Alma Mater Studiorum - Università di Bologna

DOTTORATO DI RICERCA IN

IL FUTURO DELLA TERRA, CAMBIAMENTI CLIMATICI E SFIDE SOCIALI

Ciclo 35

Settore Concorsuale: 04/A4 - GEOFISICA

Settore Scientifico Disciplinare: GEO/12 - OCEANOGRAFIA E FISICA DELL'ATMOSFERA

OCEANIC NEAR-INERTIAL INTERNAL WAVES GENERATION, PROPAGATION AND INTERACTION WITH MESOSCALE DYNAMICS

Presentata da: Elisa Cozzani

Coordinatore Dottorato

Silvana Di Sabatino

Supervisore

Paolo Oddo

Co-supervisori

Nadia Pinardi

William R. Young

Inès Borrione

Esame finale anno 2023

Acknowledgments

I would like to express my sincere gratitude to my supervisor Prof. Paolo Oddo for mentoring me through the winding road that led to this work and for always being available.
I would like to thank Prof. Nadia Pinardi for accepting me in the collaborative programme between the University of Bologna and the NATO-STO Centre for Maritime Research and Experimentation (La Spezia) and for the helpful discussions about my work.
Many thanks to Dr. Inès Borrione for her valuable suggestions, constructive criticism, and support during the tough periods of the PhD, which were further complicated by the Covid-19 pandemic.
I am extremely grateful to Prof. William Young for giving me the opportunity to spend three months at UCSD Scripps Institution of Oceanography (San Diego, California), for guiding me through the Near-inertial internal waves, for his kindness and availability.
I would like to acknowledge the NATO-STO CMRE for financial support and all the staff I met, especially the Data & Environmental Knowledge and Operational Effectiveness Department for helping me process and analyse the data, the IT Department for solving technical problems efficiently, and the Engineering Department for sharing their knowledge and time spent together aboard the research vessels.
A shout-out to my colleagues with whom I started this graduate program and to those I met at the University of California San Diego.
I would like to mention my friends and I am especially grateful to Lucia and Giulia for their encouragement and for our friendship.
Special thanks to my family for their support and for standing by me even when I was 10000 km away, and for filling my heart with joy when my niece Martina was welcomed into the world.

Abstract

Oceans play a key role in the climate system, being the largest heat sinks on Earth. Part of the energy balance of ocean circulation is driven by the Near-inertial internal waves (NIWs), which contain half of the energy of the ocean internal wave spectrum (Ferrari and Wunsch 2009). Global studies show that the Near-inertial internal waves transport energy on different scales affecting also climate (Jochum *et al*., 2013). The NIWs generation, their propagation, their properties, and how the latter change when interacting with mesoscale structures is the focus of this work, providing, to the author's knowledge, the first characterization of NIWs in the Mediterranean Sea. The observations used in this study were collected during a multi-platform, multi-disciplinary and multi-scale campaign led by the NATO Centre for Maritime Research and Experimentation during autumn 2017 to investigate the variability and predictability of the properties of the Ligurian Sea (northwestern Mediterranean Sea) at different scales. The large-scale characterization of the studied area and its variability are analysed by combining satellite and glider data. The analysis shows that the main currents of the Ligurian Sea at the time of the campaign were characterised by high variability with strong mesoscale activity. High variability was also observed at the sub-mesoscale.

Water current measurements collected with a deep-sea and a coastal mooring provide evidence of strong NIWs. At the mooring anchored at 1000 m depth, NIWs are observed between 30 and 250 m depth , while at the near-coastal mooring, fixed at 100 m depth, the strongest NIWs signal is confined between 55 and 63 m depth. Analysis of the collected data shows that the near-surface NIWs are generated locally by wind gusts, while the deeper waves originate in other regions and arrive at the moorings.

Most of the observed NIWs energy propagates downward with a mean vertical group velocity of $(2.2\pm0.3)\cdot10^{-4}$ m s^{-1}. Only one NIW propagates upward along isopycnals. The analysis also shows that the NIW energy propagates faster in both vertical and horizontal directions near the surface than at greater depths. On average, the NIW at the deep mooring have an amplitude of 0.13 m s^{-1} and mean horizontal and vertical wavelengths of 43±25 km and 125±35 m, while we observe shorter wavelengths at the near-coastal mooring, 36±2 km and 33±2 m, respectively. Most of the observed NIWs are blue shifted and reach a value 9% higher than the local inertial frequency. Only two observed NIWs are characterised by a redshift (up to 3% lower than the local inertial frequency).

In order to support and complement the *in situ* observations, a two-way parent-child nested NEMO (v4.0.4) numerical model is implemented. The coarser (1300m resolution) parent domain covers the area with coordinates (8°E-11.75°E, 42.2°N-44.45°N), while the child domain reaches a horizontal resolution of 400 m over the domain extending (9°E-10.3°E, 43.6°N-44.4°N). Both the parent and child domain share a common vertical grid discretized with 141 unevenly spaced levels from the surface to a depth of 2750 m.

The model agrees with observations as NIWs are the dominant high-frequency processes (period < 36h) and shows that the most energetic NIWs are generated in the northwestern part of the domain. Moreover, the model reproduces the intense mesoscale activity that characterises the region and further shows that such mesoscale activity strongly interacts with NIWs modifying their properties. In agreement with previous studies in other regions of the world (Kunze 1985, Poulain 1992, Rainville and Pinkel 2004, Young and Jelloul 1997, Asselin and Young 2020), results show that anticyclones (cyclones) shift the frequency of NIWs to lower (higher) frequencies with respect to the local inertial frequency. Anticyclones act as a waveguide, and facilitate the downward propagation of NIW energy, while cyclones dampen NIW energy. A special case shows the absence of NIWs energy within an anticyclone characterised by a strong normalised vorticity. This is due to the low kinetic energy transfer of the wind, which does not generate NIWs locally. NIWs generated north of the anticyclone in the surface layers are diverted around the anticyclone, while some of the energy is likely dissipated when encountering strongly slanted isopycnals.

Table of Contents

1. Introduction

1.1 Motivation

In the Earth system, oceans absorb, store, and transport an enormous amount of energy. Improving our present understanding of ocean dynamics, at all scales, can help us better predict the weather and better understand the effects of climate change on the Earth, considering that oceans alone absorb 90% of the excess heat caused by climate change (IPCC 2019, Bindoff *et al*., 2019).

The variety of multidisciplinary ocean-datasets available to date, compiled from *in situ*, satellite and modelling simulations (i.e., Copernicus Marine Service, Le Traon *et al*., 2019; World Ocean Atlas, Boyer *et al*., 2018) allowed an in-depth study of the large-scale processes that characterise the ocean (Macdonald and Wunsch, 1996; Ganachaud and Wunsch, 2000; Le Traon, 2013; Pinardi *et al*., 2015). Conversely, this level of knowledge has not yet been achieved for small-scale dynamics because the collection of high-resolution *in situ* observations is difficult and costly, mooring measurements are sparse, gliders are slow and collect data on a zigzag trajectory, ships collect data in a limited area, satellites measure only the ocean surface, and models require high computational costs to achieve high resolution. Nevertheless, the small-scale processes exchange a huge amount of energy with the large-scale processes, via the inverse energy cascade (Salmon 1998; Kobashi and Kawamura, 2002; Scott and Wang, 2005), and are therefore capable of affecting the overall energy balance of the ocean circulation.

This study focuses particularly on the small-scale, high-frequency processes because they contain most of the energy in the ocean power spectra (Callies and Ferrari 2013; Wortham and Wunsch, 2014). Moreover, at high frequencies, the ocean kinetic energy spectra is dominated by internal waves with frequencies close to the local inertial frequency (Ferrari and Wunsch 2009).

A better understanding of small-scale, high-frequency processes in the ocean, that are highly energetic and affect large-scale processes, may be important from a global perspective.

1.2 Ligurian Sea background

The present study focuses on the Ligurian sea located in the Northwestern Mediterranean Sea (Figure 1.1-1). The Mediterranean Sea is also called a "miniature ocean" as all the processes found in the world's oceans are found here (Bethoux *et al*., 1999; Tsimplis *et al.*, 2006). Its overturning circulation resembles that of the world ocean, here deep and intermediate water masses form (Robinson *et al*., 2001), which contribute to the Mediterranean outflow through the Strait of Gibraltar and can thus influence the stability of the global thermohaline circulation (Fedele *et al*., 2022). The Mediterranean circulation, like the major ocean regions of the world, is

driven by wind stress and upwelling currents (Pinardi *et al*., 2015) and is dominated by a mesoscale circulation component (Robinson *et al*., 1987; Ayoub *et al*., 1998).

The Mediterranean Sea represents a laboratory area for oceanographic studies because of its relatively small extent and large number of *in situ* observations (e.g., Mediterranean Ocean Observing System for the Environment; Mediterranean Operational Network for the Global Ocean Observing System). Studies in this region contribute significantly to our current understanding of ocean dynamics (Robinson *et al*., 1992; Robinson and Golnaraghi 1993).

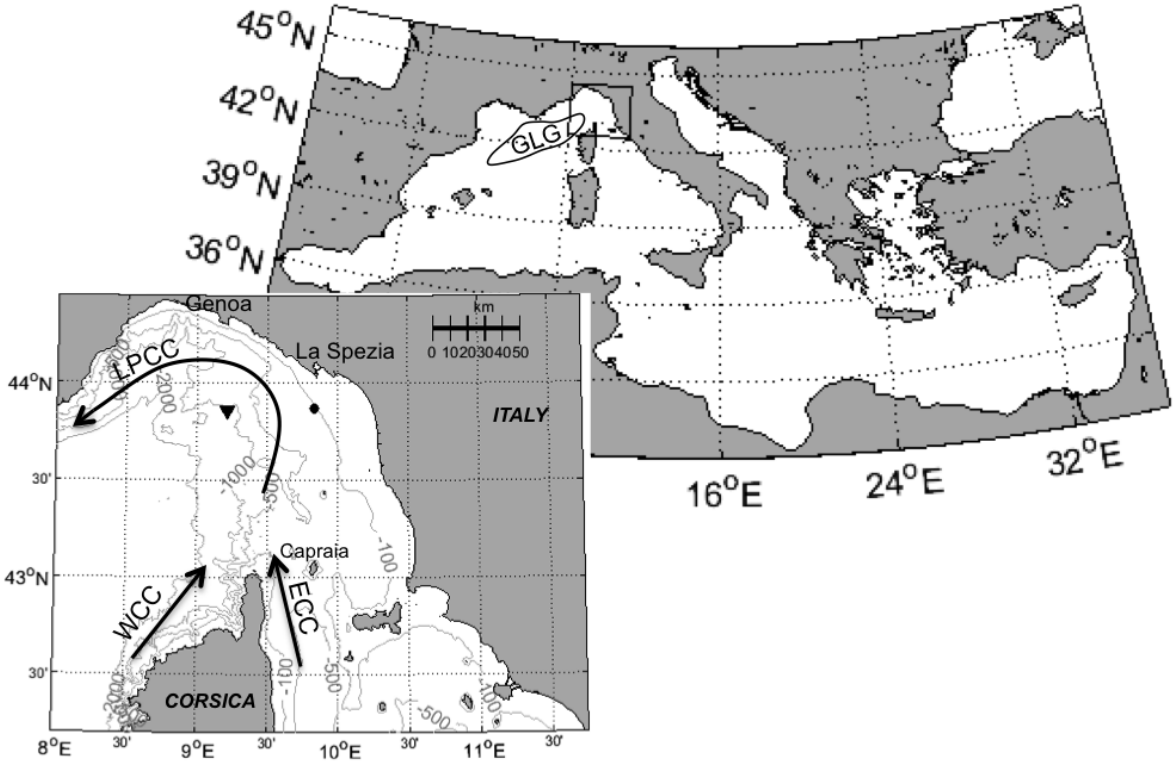

Figure 1.1-1: Upper panel: Mediterranean Sea and Gulf of Lion Gyre (GLG) derived from the mean flow field of the 1987-2007 reanalysis (Pinardi et al., 2015). The black square shows the zoomed area of the Ligurian Sea shown in the bottom left panel. Bottom left panel: schematic mean currents Liguro-Provencal Catalan Current (LPCC), Western Corsica Current (WCC), Eastern Corsica Current (ECC) are indicated by black arrows. The thin grey lines represent the contours of the bathymetry at 100, 500, 1000 and 2000 m depth.

The Ligurian Sea plays a crucial role in the Mediterranean circulation. It is the region where the confluence of two currents flowing along the Corsica sides, namely Western Corsica Currents (WCC) and Eastern Corsica Currents (ECC) (Astraldi and Gasparini, 1992), forms the Liguro-Provencal Catalan Current (LPCC). The LPCC is a 30-50 km wide boundary current that flows north from Corsica and then southwest along the Italian, French, and Spanish coasts (Millot, 1991). During winter, LPCC is stronger and mesoscale activity is more intense than

during summer (Birol *et al*., 2010). In particular, the time windows of mesoscale activity from late fall to winter are 3-6 days, while in summer they are 10-20 days (Taupier-Letage and Millot, 1986; Albérola *et al.*, 1995; Sammari *et al.*, 1995; Echevin *et al.*, 2005). The meandering nature of the LPCC has long been studied (Crépon *et al*., 1982; Marullo *et al.*, 1985; Flexas *et al*., 2002, 2005), and recently some studies have been published focusing on eddy activity north of Corsica, where WCC and ECC form the LPCC (Borrione *et al*., 2016; Casella *et al.*, 2014).

The western Liguro-Provencal basin is characterised by a large permanent cyclonic eddy referred to as the Gulf of Lion Gyre (GLG) (Madec *et al*., 1991; Pinardi *et al*., 2006; Pinardi *et al*., 2015). In addition, an anticyclone has been observed around the island of Capraia during oceanographic campaigns in the northwestern Mediterranean Sea (Poulain *et al*., 2012).

Understanding the variability of the LPCC and consequently the strength and position of the GLG is still an open debate, but we know that it is influenced by the structure of the wind stress curl over the basin (Herbaut *et al.*, 1996) and by frictional dissipation mechanisms along the continental shelf (Pinardi and Navarra, 1993).

The LPCC plays a key role in the Mediterranean circulation and transports the most important water masses in the region (Conan and Millot 1995). The Modified Atlantic Water (MAW), enters the Mediterranean Sea through the Strait of Gibraltar and changes its properties as it travels throughout the basin. The MAW are located between the surface and 200 m depth and their properties are seasonally variable and influenced by heat and water exchange with the atmosphere. This water mass is influenced by local climatic conditions (Schroender *et al*., 2006). Another important water mass that is easily identified in the Ligurian Basin at intermediate depths is the Modified Levantine Intermediate Water (MLIW), which originally forms in the Levantine Basin (Lascaratos *et al.*, 1993). The typical temperature and salinity of the MLIW core in the western Mediterranean range from 13 to 14.2°C and 38.4 to 38.8, respectively, and the depth ranges from 200 to 600 m (Millot *et al*., 2013; Borrione *et al.*, 2019). Although the characteristics of the LIW change less than those of MAW, they are affected by changes throughout the year, with salinity reaching a maximum in the fall (Bosse *et al*., 2015). Bosse and co-authors (2015) analysed data collected regularly from 2007 to 2013 with gliders in the northwestern Mediterranean Sea and found that warm and saline submesoscale anticyclones at intermediate depths contribute to MLIW propagation in the basin. They also show that the WCC transports the MLIW more saline (~38.66) than the LPCC (~38.60) and that from April to the following winter, the salinity and temperature of the MLIW increase.

The most recent study published in 2020 (Margirier *et al.*, 2020), based on high spatial and temporal resolution data from 2007 and 2017, reports warming (+0.06°C per year) and salinization (+0.012 per year) of MLIWs in the Ligurian Sea. MLIWs at depths of 200 to 500 m have minimum temperature and salinity values of 13.2°C and 38.54 in 2007 and reach 14.1°C and 38.7 in 2017.

The MLIW from the Tyrrhenian Sea and the MAW contribute to the formation of the Western Mediterranean Deep Water (WMDW) in the Gulf of Lions. The WMDW spreads across the northern and central parts of the western Mediterranean Sea and reaches the bottom of the Ligurian Sea (Schroder *et al*., 2006).

The different water masses present in the basin, their variability and surface fluxes all contribute in generating a significant variability in the vertical stratification. Seasonal variability of stratification in the Ligurian Sea is studied in Fratianni *et al*. (2016). Averaged seasonal squared Brunt-Vaisala frequency profiles are calculated using the 2001-2010 reanalysis provided by Copernicus Marine Service (former MyOcean Marine Service, https://marine.copernicus.eu), which assimilates satellite data, *in situ* salinity and temperature data from the Volunteer Observation Ship (VOS) (Manzella *et al*., 2007) and Argo profiling float programmes (Poulain *et al*., 2007). Their study shows an extended seasonal stratification cycle (Figure 1.1-2), and we describe here only the mean Brunt-Vaisala frequency profile in summer and fall, the seasons studied in this work. The seasonal averages are estimated using a relatively coarse resolution model. During summer the average Brunt-Vaisala frequency profile in the Ligurian Sea shows a maximum of $8 \cdot 10^{-4}$ s^{-2} at about 15 m depth and decreases until it reaches values less than 10^{-4} s^{-2} below 60 m depth. In autumn, the average Brunt-Vaisala frequency is less than 10^{-4} s^{-2} until a depth of 20 m, then increases and reaches a maximum of $2 \cdot 10^{-4}$ s^{-2} at 40 m depth, then decreases to values less than 10^{-4} s^{-2} below 70 m depth.

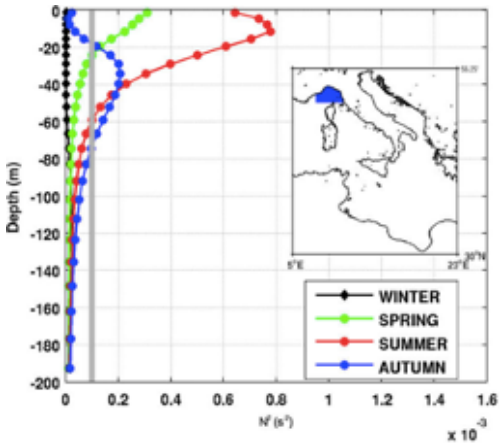

Figure 1.1-2 : Brunt-Vaisala frequency profile color-coded with season typical of the Ligurian Sea. The vertical gray line indicates the value of 10^{-4} s^{-2}. Excerpt from Fratianni et al., 2016.

A monthly climatology of the Mediterranean Mixed Layer Depth (MLD) obtained from the analysis of individual *in situ* profiles (D'Ortenzio *et al.*, 2005) shows that the MLD in the Ligurian Sea is about 15 m deep in September and October, while it reaches 50 m in November.

Additional background information on the Ligurian Sea is provided by the Rossby number and the Rossby radius of deformation. A measure of the relative importance of the nonlinear advective term on the mesoscale eddy field is the ratio between the term of the Coriolis force and the nonlinear term in the momentum equations (further details in 2.2.1: Dimensionless analysis and a-dimensional numbers). The beta Rossby number is defined as the ratio between the planetary and relative vorticity advection (Pedlosky, 1987):

$$\beta = \frac{\beta_0 L^2}{U} \qquad (1.2\text{-}1)$$

where β_0 is the latitudinal gradient of the Coriolis parameter, L is the horizontal eddy scale, and U is the velocity scale. In the Mediterranean Sea, the magnitude of the beta Rossby number is 0.01 being U=0.1 $m\,s^{-1}$, L=10km, $\beta_0 = 10^{-11} m^{-1} s^{-1}$ (Robinson *et al*., 2001). Regarding the seasonality of the Rossby radius of deformation, the study conducted by Grilli and Pinardi (Grilli and Pinardi 1998) shows that the first baroclinic Rossby radius is about 8 km in winter, 9 km in spring, and about 11 km in summer and autumn. Borrione and co-authors (2019), based on oceanographic data collected in the Ligurian Sea in spring 2016, provided an estimate of the Rossby number of about 0.03 and a Rossby radius of deformation of about 18 km (Borrione *et al*., 2019). This implies that nonlinear dynamics could be relevant, driving large inverse energy cascades (Rhines, 1979) and implying also a "long lifetime" of vortices.

To complete the background picture of the Ligurian Sea, the main tidal components are the diurnal (K1) and semidiurnal (M2) with periods of 23.93 and 12.42 hours, respectively, but the tides in this region are weak (Alberola *et al*., 1995).

1.3 Near-Inertial Internal Waves

A preliminary analysis of *in situ* observations collected during the LOng-term Glider Missions for Environmental Characterization (LOGMEC17) campaign led by the NATO Centre for Maritime Research and Experimentation in the Ligurian Sea in fall 2017 shows that Near-Inertial Internal Waves (NIWs) are the dominant high-frequency process. These waves are the core of the present study, they have a frequency close to the local inertial frequency and are called "internal" because they occur in the interior of the ocean. Internal waves play a key role in the ocean because they cause strong vertical shear and thus turbulence and mixing (Ostrovsky and Stepanyants, 1989; Moum *et al*., 2013; Nash and Moum, 2005). There are several types of internal waves in the ocean, but the most energetic are internal tides and NIWs (MacKinnon, 2017). NIWs are capable of increasing the oceanic mixed layer depth by up to 30% and affecting climate (Jochum *et al*., 2013).
NIWs exist everywhere except at the equator and they rotate clockwise (counterclockwise) in the northern (southern) hemisphere and are intermittent (Fu, 1981). The main generation mechanism

is the wind (Alford *et al*., 2016), in particular impulsive wind stress generates near-inertial oscillations in the surface mixed layer and the convergences and divergences of these oscillations pump the base of the mixed layer transfering energy to downward propagating NIWs (D'Asaro 1985; Alford *et al*. 2016). From their area of origin, NIWs can propagate for hundreds of kilometres until they break up (Ray & Mitchum 1996, Alford 2003, Zhao & Alford 2009). During NIWs propagation, they interact with other processes that alter their properties, making NIWs characterization challenging (Alford *et al*., 2016).
The NIWs phase propagates mainly upward (Sanford 1975), with some exceptions (Alford *et al*., 2016). An upward phase velocity implies a downward group velocity, hence downward energy propagation (Leaman and Sanford 1975, D'Asaro and Perkins 1984).

The horizontal scale of NIW ranges from a few tens to hundreds of kilometres, while the vertical wavelength is three orders of magnitude smaller (Kundu 1976, Kawaguchi *et al*., 2020, Lelong *et al*., 2020). Several studies show that NIWs strongly interact with mesoscale features causing a frequency shift of NIW with respect to the local inertial frequency (Kunze 1985, Poulain 1992, Rainville and Pinkel 2004, Young and Jelloul 1997, Asselin and Young 2020). Mesoscale structures in the Ligurian Sea have an horizontal scale of 18-20 km (Casella *et al*., 2014; Schroeder *et al*., 2014; Borrione *et al*., 2016).

Despite the importance of NIWs, there are few theoretical, observational, and modelling studies of these waves in the Mediterranean Sea. The Ligurian Sea is a suitable area for the study of NIW because tides are weak and the inertial frequency ($\sim 10^{-4}$ s^{-1} corresponding to about 17.3 hours) can be easily distinguished from the main tidal frequency (diurnal and semidiurnal).

The key to characterise the NIWs lies in estimating the variables of the dispersion relation. The dispersion relation of NIWs (equation (1.3-18)) is derived starting from the linearized hydrostatic Boussinesq equations of motion on the *f*-plane (from equation 1.3-1 to equation 1.3-5).

Zonal

$$\frac{\partial u}{\partial t} - fv = -\frac{1}{\rho_0}\frac{\partial p}{\partial x} \tag{1.3-1}$$

Meridional

$$\frac{\partial v}{\partial t} + fu = -\frac{1}{\rho_0}\frac{\partial p}{\partial y} \tag{1.3-2}$$

Vertical under hydrostatic approximation

$$\frac{\partial p}{\partial z} = -\ g\rho' \tag{1.3-3}$$

Continuity equation

$$\frac{\partial u}{\partial x} + \frac{\partial v}{\partial y} + \frac{\partial w}{\partial z} = 0 \tag{1.3-4}$$

$$\frac{\partial \rho'}{\partial t} - \frac{\rho_0 N^2 w}{g} = 0 \tag{1.3-5}$$

Equation (1.3-5) uses the definition of the Brunt-Vaisala frequency N (1.3-7) and results from the assumptions of incompressibility of the fluid and small perturbations:

$$\frac{D\rho}{Dt} = \frac{\partial \rho'}{\partial t} + w\frac{d\rho_0}{dz} = 0 \tag{1.3-6}$$

$$N^2 = -\frac{g}{\rho_0}\frac{d\rho_0}{dz} \tag{1.3-7}$$

Computing the tendency of equation (1.3-3):

$$\frac{\partial \rho'}{\partial t} = -\frac{1}{g}\frac{\partial^2 p}{\partial t\, \partial z} \tag{1.3-8}$$

Substituting equation (1.3-8) into equation (1.3-5), we get:

$$\frac{\rho_0 N^2 w}{g} = -\frac{1}{g}\frac{\partial^2 p}{\partial t\, \partial z} \tag{1.3-9}$$

By summing the second derivatives with respect to x and to y of equation (1.3-9):

$$-\rho_0 N^2\left(\frac{\partial^2 w}{\partial x^2} + \frac{\partial^2 w}{\partial y^2}\right) = \frac{\partial}{\partial t}\frac{\partial}{\partial z}\left(\frac{\partial^2 p}{\partial x^2} + \frac{\partial^2 p}{\partial y^2}\right) \tag{1.3-10}$$

Eliminate the variable v from equation (1.3-1) by adding the tendency of equation (1.3-1) to f times equation (1.3-2):

$$\frac{\partial^2 u}{\partial t^2} + f^2 u = \frac{1}{\rho_0}\frac{\partial^2 p}{\partial x\, \partial t} - f\frac{1}{\rho_0}\frac{\partial p}{\partial y} \tag{1.3-11}$$

Eliminate the variable u from equation (1.3-2) by adding the tendency of equation (1.3-2) to f times equation (1.3-1):

$$\frac{\partial^2 v}{\partial t^2} + f^2 v = -\frac{1}{\rho_0}\frac{\partial^2 p}{\partial y\, \partial t} + f\frac{1}{\rho_0}\frac{\partial p}{\partial x} \tag{1.3-12}$$

Summing the x derivative of (1.3-12) to the y derivative of (1.3-11):

$$\left(\frac{\partial^2}{\partial t^2} + f^2\right)\left(\frac{\partial u}{\partial x} + \frac{\partial v}{\partial y}\right) = \frac{1}{\rho_0}\frac{\partial}{\partial t}\left(\frac{\partial^2 p}{\partial x^2} + \frac{\partial^2 p}{\partial y^2}\right) \tag{1.3-13}$$

Using the continuity equation (1.3-5), the derivative of equation (1.3-13) with respect to z is:

$$-\left(\frac{\partial^2}{\partial t^2} + f^2\right)\left(\frac{\partial^2 w}{\partial z^2}\right) = \frac{1}{\rho_0}\frac{\partial}{\partial z}\frac{\partial}{\partial t}\left(\frac{\partial^2 p}{\partial x^2} + \frac{\partial^2 p}{\partial y^2}\right) \tag{1.3-14}$$

Substituting the right term of equation (1.3-10) into equation (1.3-14):

$$\left(\frac{\partial^2}{\partial t^2} + f^2\right)\left(\frac{\partial^2 w}{\partial z^2}\right) = -N^2\left(\frac{\partial^2 w}{\partial x^2} + \frac{\partial^2 w}{\partial y^2}\right) \tag{1.3-15}$$

Assuming the wave form of solution:

$$w = w_0 e^{i(kx+ly+mz-\omega t)}$$

Equation (1.3-15) can be written:

$$\begin{aligned} &-w_0 \frac{\partial^2}{\partial t^2}\left(m^2 e^{i(kx+ly+mz-\omega t)}\right) - f^2 w_0 m^2 e^{i(kx+ly+mz-\omega t)} + \\ &-w_0 N^2\left(k^2 + l^2\right)e^{i(kx+ly+mz-\omega t)} = 0 \end{aligned} \tag{1.3-16}$$

Developing the time derivatives, eliminating the term $w_0 e^{i(kx+ly+mz-\omega t)}$ and using the definition of the horizontal wavenumber $K_H^2 = k^2 + l^2$, the last equation can be written as follows:

$$\omega^2 m^2 - f^2 m^2 - N^2 K_H^2 = 0 \tag{1.3-17}$$

We obtain the NIWs dispersion relation:

$$\omega^2 = f^2 + \frac{N^2 K_H^2}{m^2} \tag{1.3-18}$$

Once all parameters of the dispersion relation are known, the horizontal and vertical phase velocity (C_h, C_z) as well as the group velocity (C_{gh}, C_{gz}) can be estimated using the equations (1.3-19) to (1.3-22).

$$C_h = \frac{\omega}{K_H} \tag{1.3-19}$$

$$C_z = \frac{\omega}{m} \tag{1.3-20}$$

$$C_{gh} = N\frac{\sqrt{\omega^2 - f^2}}{\omega m} \tag{1.3-21}$$

$$C_{gz} = -\frac{N^2 K_H^2}{m^2\sqrt{f^2 m^2 + N^2 K_H^2}} \tag{1.3-22}$$

1.4 Objectives and structures of the thesis

The general aim of the present study is to improve the understanding of small-scale, high-frequency processes. Preliminary analyses of the LOGMEC17 dataset show that Near-Inertial Internal Waves are the dominant high-frequency processes in the studied area, so the main objectives can be summarised as follows:

1. characterise the studied area at different scales during the LOGMEC17 experiment;
2. study the generation of the NIWs and their propagation;
3. estimate the properties of the NIW such as frequency, wavelength, group velocity and phase velocity;
4. study the interaction between NIWs and mesoscale structures.

To achieve these goals, we can identify three steps. First, analysing *in situ* observations; second, implementing a numerical model to support the observations; and third, combining the model with observations to evaluate the numerical model and conduct an in-depth study of the observed process.
This work is organised as follows. Chapter 2 first introduces the LOGMEC17 experiment, then explains some theoretical background on the methods used to achieve the goals of this thesis, and describes the numerical model implemented. Chapter 3 characterises the oceanographic environment of the experimental area at different scales. Generation, propagation, and characterization of the observed NIWs are presented in Chapter 4. Chapter 5 examines the interaction of NIWs with mesoscale structures by combining observations with the dedicated numerical model. Chapters 4 and 5 will be submitted as scientific papers. Chapter 6 summarises the conclusions of this study.

2. Data and Methods

In this chapter, the data set used to study the small-scale high-frequency dynamics in the Ligurian sea is introduced, as well as the theoretical background of the methods used to analyse the data set. The numerical model implemented to achieve the objective of this work is also presented.

2.1 The LOGMEC17 Sea Trial Experiment

The LOng-term Glider Missions for Environmental Characterization 2017 (LOGMEC17) is a multi-platform, multi-scale, multi-disciplinary combined acoustic and oceanographic campaign led by the NATO-STO Centre for Maritime Research and Experimentation (CMRE). The sea trial aimed at investigating the variability and predictability of the Ligurian Sea properties at different scales took place in the Ligurian Sea from 13 September to 14 November 2017 (Figure 2.1-1). The experimental design was optimised to sample synoptically multiple oceanographic scales. The spatial and temporal scales covered by the different platforms are summarised in Table 2.1-1.

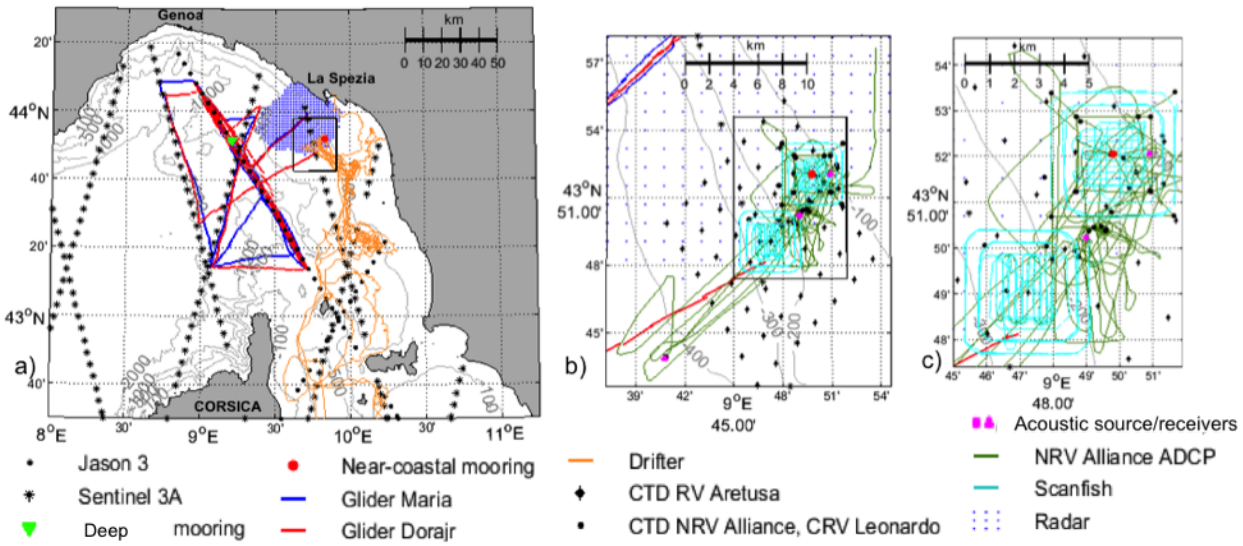

Figure 2.1-1: Overview of datasets collected during LOGMEC17 at the large (a), mesoscale (b), and submesoscale (c). The black square in panels (a) and (b) shows the zoomed area in panels (b) and (c) respectively. The thin grey lines represent the bathymetry. The legend is at the bottom of the figure.

Platforms		Parameters	Sampling scale & deployment time	Spatial scale	Depth (m)	Date
Autonomous	Gliders	T,S,P,Chl, Oxygen, turbidity	Minutes Monthly	Multi	[0, 1000]	21/Sep-10/Nov
	ScanFish	T,S,P,Chl, Oxygen	Minutes Daily	Sub-mesoscale	[0, 150]	26-29/Sep; 1-2/Oct; 24/Oct; 26/Oct
	Drifters	Water current	Monthly	Large	Surface	26/Sep; 02/Oct
Shipboard	CTD	T,S,P, Oxygen	Minutes Daily	Mesoscale Sub-mesoscale	[0, 400]	27-29/Sep
	ADCP	Water current	Minutes Daily	Sub-mesoscale	[0, 800]	26-29/Sep; 1-2/Oct; 24/Oct; 26/Oct
Fixed	Radar	Water current	Hours Monthly	Mesoscale	[0, 0.5]	13/Sep-14/Nov
	Acoustic buoys	Sound Level	Minutes Weekly	Sub-mesoscale	[0, 420]	26/Sep-03/Oct
	Moorings	T,S,P, water current	Minutes Months	Multi	[0, 1000]	13/Sep-14/Nov

Table 2.1-1: Platforms, data collected, temporal and spatial scales, depth reached and deployment date during the LOGMEC17 campaign. The letters T, S, and P represent temperature, salinity, and pressure measurements, respectively.

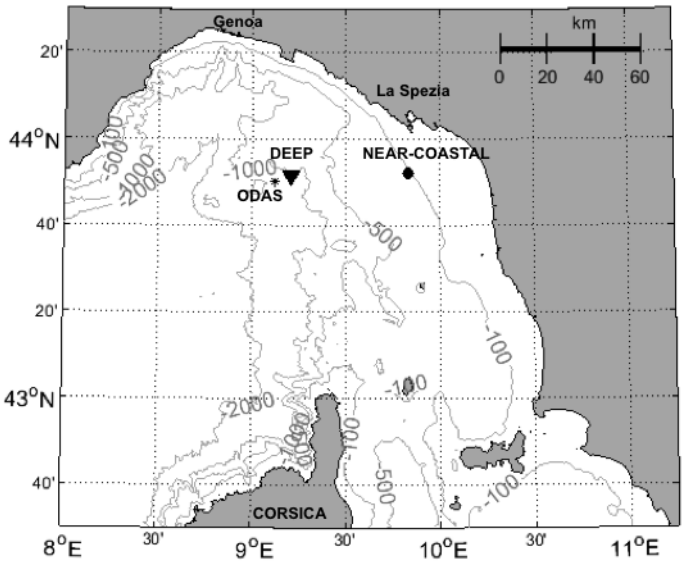

Figure 2.1-2: Deep, near-coastal, and ODAS moorings are indicated by a black triangle, dot, and asterisk, respectively. The thin grey lines represent bathymetry.

Two deep oceanographic gliders (named Maria and Dora-jr), sampling from surface to 1000 m depth, were deployed for a two month mission to collect large-scale samples (Figure 2.1-1a) and their trajectories were designed to complement available satellite data. The gliders are autonomous underwater vehicles that move up and down along the water column by changing their buoyancy and using wings to generate forward motion. As they move, the gliders follow a sawtooth-like path, providing a high-resolution data set along the vertical (Figure 2.1-3). The very low power consumption deriving from the buoyancy-based propulsion allows data to be collected over a long period of time. Usually they reach data from the user-defined depth to the subsurface, but occasionally (as at 05:00 in Figure 2.1-3) they remain at the surface to transmit data.

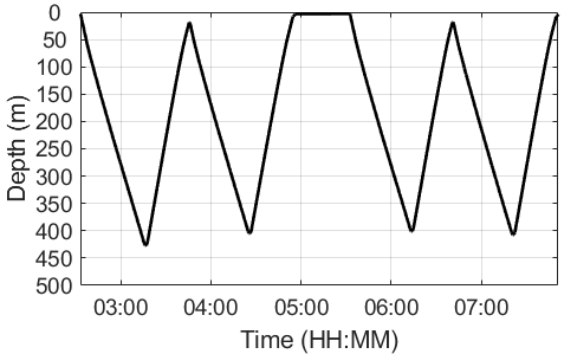

Figure 2.1-3: Glider path

The gliders were equipped with multidisciplinary sensors, but for the present study only the data collected with the Conductivity Temperature Depth (CTD) sensors were used. The glider Maria was launched on September 21 and recovered on November 10. The first deployment of Dora-jr took place from 21 to 25 September and the second from 28 September to 10 November. During their mission, the two gliders followed the satellite tracks of Jason-3 and Sentinel-3A. The co-located and near-contemporaneous acquisition of measurements from gliders and satellites is challenging but useful, as it improves, for example, the understanding of altimetry signals (Borrione *et al*., 2019). The LOGMEC17 experiment supported several studies, including estimated correlation between remote and *in situ* observations to optimise assimilation in ocean models (Storto *et al*., 2019).

During the two-month glider mission, two oceanographic moorings were anchored to provide fixed-point and high-frequency observations (Figure 2.1-2). One was deployed near the 1000m bathymetric line (to also support correlation studies of data collected by the satellite glider), and the second was deployed in shallower water, at about 100m depth.

The location of the deep mooring is 43.8563°N, 9.2088°E (Figure 2.1-2) and it collected data for two months (13/Sep - 14/Nov/2017). As shown in the mooring design (Figure 2.1-3a), many ocean sensors were mounted at different depths to measure temperature, salinity, and pressure data every 10 seconds. At 250 m depth, an upward looking Acoustic Doppler Current Profiler

(ADCP) measures the velocity and direction of ocean currents by using the principle of the Doppler effect of sound waves backscattered from particles in the water. According to the ADCP Practical Primer (ADCP Practical Primer, 2011), the range of surface contamination is between 6% and 15% of the water column depth. Therefore, analysis of ADCP data from deep mooring is limited to measurements made below 20 m.

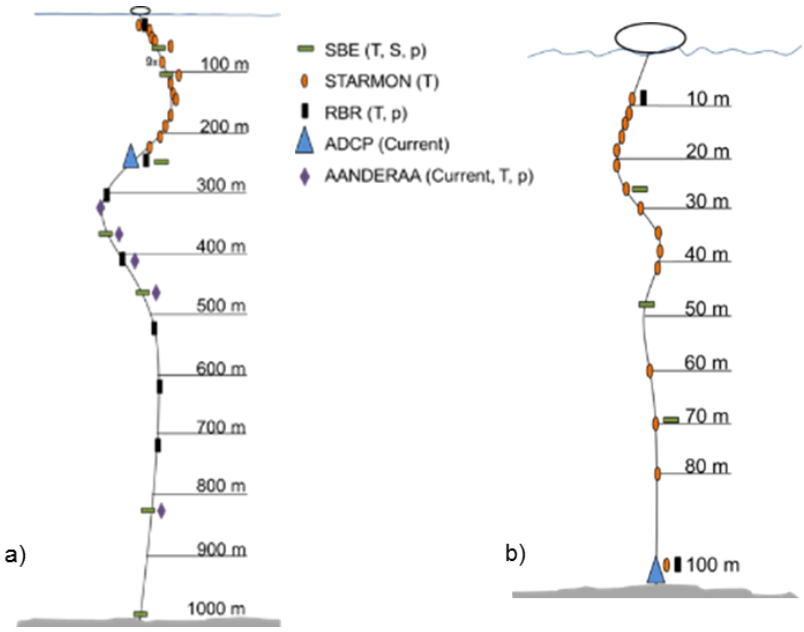

Figure 2.1-4: Deep (a) and near-coastal (b) mooring design.

The near-coastal mooring was moored at 43.8675 °N, 9.8300°E, close to the 100-metres bathymetric line (Figure 2.1-2). The buoy was equipped with an upward looking ADCP mounted at 100 m, measuring water currents till the subsurface and the following working sensors: 15 Starmon (temperature sensors), 3 SBE (CTD), 2 RBR (temperature and pressure sensors). The mooring design is shown in Figure 2.1-4b. The near-coastal mooring collected data for one month (27/Sep – 25/Oct/2017). Considering the ADCP Practical Primer, the currents observed by near-coastal ADCP may be considered reliable below 15 metres. Therefore the analysis of near-coastal ADCP data will be carried out on the measurements below the 15 metres depth only.

All dataset collected by ADCP underwent an iterative quality control. For each sampling depth, values outside the range defined by the mean ± 3 times standard deviation were flagged as spikes and removed.

To characterise the intermediate and the small scales, three vessels collected data for one week: the Research Vessel (RV) Aretusa of the Italian Navy, the NATO Research Vessel (NRV) Alliance and the Coastal Research Vessel (CRV) Leonardo. Intermediate scale was sampled by RV Aretusa conducting several regular spaced CTD casts from 27 to 29 September (Figure 2.1-1b and Figure 2.1-5).

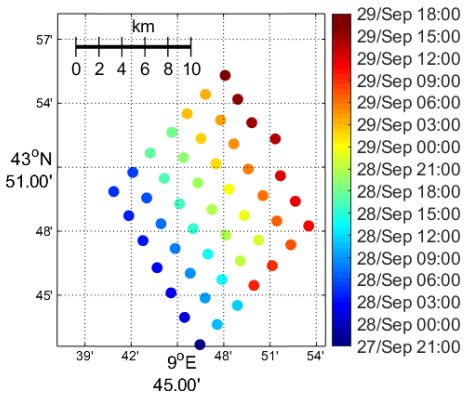

Figure 2.1-5: CTD locations collected by RV Aretusa (same as in Figure 2.1-1b) colour coded with time.

The sampling area is a square with a 15 km long side and the distance between CTD stations is 2.5 km. From now onwards this sampling will be named LS2500 that stands for Large Scale with horizontal resolution of 2500m. The vessel started from the southernmost corner of the sampling square and then reached the North corner following a back-and-forth path. The sampling was completed in 33 hours.

In the same area clusters of drifters, a fleet of oceanographic-acoustic shallow water gliders and acoustic moorings have been deployed by RV Alliance and CRV Leonardo. In particular clusters of CODE (Coastal Ocean Dynamics Experiment) drifters were deployed to acquire surface current measurements. The first deployment was carried out on 26 September and the second one on 1 October. A total of 19 drifters were deployed (drifters trajectories are drawn in Figure 2.1-1a).

The small-scale dataset (Figure 2.1-1c) was collected by CRV Leonardo using a towed undulating vehicle system, named Scan-Fish, equipped with CTDs and optical sensors. Its rapid vertical motion allows to gather profile at very high vertical and horizontal resolution and a cable reports data back to the vessel in real-time. During the small-scale sampling the ScanFish collected data from surface up to 100-150m depth. Different sampling strategies (Figure 2.1-6) allowed to capture mesoscale and sub-mesoscale features.

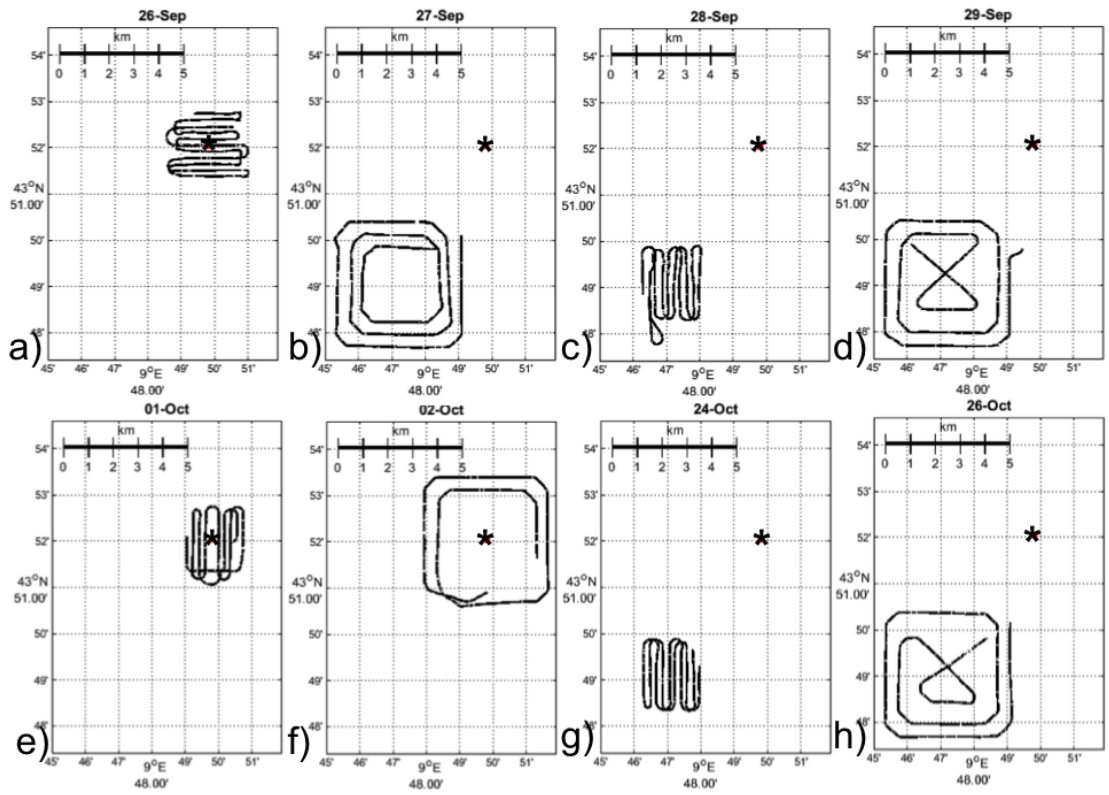

Figure 2.1-6: CRV Leonardo paths (black line) during ScanFish sampling September 26-29 (a,b,c,d respectively) and October 1, 2, 24, and 26 (e,f,g,h). The black asterisk indicates near-coastal mooring location.

The surveys covered two squares 5 km wide (Figure 2.1-1c and contextualised over time and space in Figure 2.1-6). One centred on the larger sampling CTD area (RV Aretusa) and the other one centred on the location of the near-coastal mooring. From 27 to 29 September the ScanFish collected data simultaneously with the RV Aretusa CTD survey at the centre of the CTD sampling area (Figure 2.1-6b,c,d) and the minimum and maximum distance of the ScanFish from the near-coastal mooring is 4 and 10 km respectively. The 1st and 2nd October the sampling area was centred on the near-coastal mooring location (Figure 2.1-6e,f). The other two ScanFish surveys during 24 and 26 October (Figure 2.1-6g,h) are similar to the 28 and 29 September paths, respectively (Figure 2.1-6c,d).

Different sampling strategies are adopted to sample the areas. The area perimeter is sampled following a concentric square track starting from the widest square and going towards the centre reaching a resolution of 500m horizontally (Figure 2.1-6b,f), named SM500. The centre of the area is sampled following an "S" path back and forth (Figure 2.1-6a,c,e,g) and reaching an horizontal resolution of about 250 m (SM250). The choice of covering the square area back and forth takes into account the difficulties of manoeuvring the ship with the towed instrument and it is useful in order to study the spatial and temporal variability of the sub-mesoscale dynamics. In

addition, when limited time was available, hybrid strategies, named SM500-2, were applied (Figure 2.1-6d,h).

During the ScanFish sampling the CRV Leonardo shipboard mounted ADCP collected continuously current data. Furthermore the CRV Leonardo collected CTD casts before and/or after Scan-Fish surveys and before mooring deployment and after its recovery (black dots in Figure 2.1-1b,c).

The third ship, NRV Alliance, was mainly involved in the acoustic part of the LOGMEC17 experiment conducted from 26 September 16:30 to 29 September 15:00 but the vessel also collected oceanographic data. The surveyed area was close to the near-coastal mooring. During the experiment several ship borne CTD casts have been collected. The downward ADCP mounted on the NRV Alliance measured sea currents during the whole survey period. The ADCP measurements collected by the vessels were processed with the Common Ocean Data Access System (CODAS) software.

Additional information such as surface currents is provided by radar CNR-ISMAR, and meteorological data is collected by the Oceanographic Data Acquisition System (ODAS) buoy at 43.83°N, 9.12°E (Figure 2.1-2). ODAS is a meteo-oceanographic buoy of the National Research Council of Italy and is located 7.7 km and 57.7 km from deep and near-coastal moorings, respectively.

2.2 Data Analysis Methods

This section describes the main methods used to analyse the data collected during the LOGMEC17 experiment.

Mixed layer depth

Various approaches can be used to calculate the Mixed Layer Depth (Kara *et al.*, 2000; Lorbacher *et al*., 2006). The widely used methods can be broadly divided into four categories: fixed temperature difference, fixed density difference, fixed temperature gradient, and fixed density gradient. Salinity data collected from the near-coastal mooring are sparse, so MLD can only be calculated using the temperature-based criteria. Ruiz and co-authors (Ruiz *et al.*, 2012) propose to estimate MLD as the depth at which the temperature difference from the water temperature at 10 m depth is 0.2 °C (T10 - T_h = 0.2 °C, where T_h is the temperature at depth *h* and T10 is the temperature at 10 m depth). The data from the near-coastal mooring data closest to the surface are at a depth of about 10 m, so we can use this depth as a reference depth (Kara *et al*., 2000 and Qu *et al*., 2007). The fixed temperature difference method mentioned above was applied to glider profiles with very high vertical resolution by Ruiz (2012). Unfortunately, mooring measurements have low vertical resolution compared to gliders, so after several tests a second criterion was added to the one described above: the temperature gradient should be larger than 0.02.

2.2.1 Dimensionless analysis and a-dimensional numbers

Dimensionless analysis and a-dimensional numbers are useful to identify the dominant processes and simplify the governing equations of motion. Several a-dimensional numbers are used in oceanography, here we focus on the derivation of the few used in the present study. To derive these numbers, we first introduce the primitive equations under the incompressible, hydrostatic, and Boussinesq approximations, which consist of three momentum equations (2.2.1-1), (2.2.1-2), and (2.2.1-3), a continuity equation (2.2.1-4), and an equation of state (2.2.1-5).

Zonal:

$$\frac{\partial u}{\partial t} + u\cdot\nabla u - 2\Omega sin\,\theta\ v = -\frac{1}{\rho_0}\frac{\partial p}{\partial x} + \nu\nabla^2 u + \frac{1}{\rho}\nabla_h\cdot\left(A_H\nabla u\right) + \frac{1}{\rho}\frac{\partial}{\partial z}\left(A_V\frac{\partial u}{\partial z}\right) \qquad (2.2.1\text{-}1)$$

Meridional:

$$\frac{\partial v}{\partial t} + u\cdot\nabla v + 2\Omega sin\,\theta\ u = -\frac{1}{\rho_0}\frac{\partial p}{\partial y} + \nu\nabla^2 u + \frac{1}{\rho}\nabla_h\cdot\left(A_H\nabla v\right) + \frac{1}{\rho}\frac{\partial}{\partial z}\left(A_V\frac{\partial v}{\partial z}\right) \qquad (2.2.1\text{-}2)$$

Vertical:

$$\frac{\partial p}{\partial z} = -\ \rho g \tag{2.2.1-3}$$

Continuity equation:

$$\nabla \cdot \vec{u} = 0 \tag{2.2.1-4}$$

Equation of state:

$$\rho = \rho(T, p, S) \tag{2.2.1-5}$$

where u and ν are the horizontal and vertical velocity of the fluid, Ω is the Earth's angular velocity vector, θ is the latitude, p is the pressure, ρ is the density, g is the gravitational acceleration vector, A_H, and A_V are the horizontal and vertical turbulent viscosity coefficients, respectively.

In order to derive a-dimensional numbers, we introduce the characteristic scales:

- The horizontal length scale in (x,y) is represented by L
- The vertical length scale is H
- The horizontal velocity scale (u,v) is represented by U
- The vertical velocity scale is W
- The time scale is T

In the ocean, the order of magnitude of the vertical scale H is 10^2 m, which is much smaller than the horizontal scale L of order 10^4 m (H<<L), therefore the ratio between horizontal and vertical scales is very small $\delta = \frac{H}{L} \ll 1$. This is the fundamental characteristic of shallow water theory. Moreover, the order of magnitude of U is 10^{-1} m s^{-1} and we also expect that W <<U, therefore large-scale geophysical flows are assumed shallow and nearly two-dimensional. Assuming that the temporal scale is on the order of 1 day and $\Omega = 7.3 \cdot 10^{-5}\ s^{-1}$, so we obtain $T \geq \frac{1}{\Omega}$ and $\frac{U}{L} \leq \Omega$.

Starting with the zonal component of the averaged Reynolds equation under the incompressible, hydrostatic, and Boussinesq approximations (2.2.1-1), its terms (the local tendency, advection term, Coriolis term, horizontal pressure term, horizontal and vertical turbulent and molecular viscosity) have the following dimensions:

$$\frac{U}{T}, \frac{U^2}{L}, \frac{WU}{H}, \Omega U, \frac{P}{\rho_0 L}, \frac{A_H U}{L^2}, \frac{A_V U}{H^2}$$

To evaluate the importance of the Coriolis term ΩU in relation to all other terms, we divide all terms by ΩU and obtain the following dimensionless ratios:

$$\frac{1}{\Omega T},\ \frac{U}{\Omega L},\ \frac{U}{\Omega L},\ \frac{W}{\Omega H},\ 1,\ \frac{P}{\rho_0 L\Omega U},\ \frac{A_H}{L^2\Omega},\ \frac{A_V}{H^2\Omega}$$

The first a-dimensional number is the temporal Rossby number defined as $R_{oT} = \frac{1}{\Omega T}$, which quantifies the local temporal rate of change of velocity with the Coriolis force.

At mid latitudes, θ=45°, $2\Omega sin\,\theta = 2 \cdot 7.3 \cdot 10^{-5} \cdot 0.71 \simeq 10^{-4}$, so the temporal Rossby number is of order 0.1.

The a-dimensional number $\frac{U}{\Omega L}$ is the so-called Rossby number R_o .

$$R_o = \frac{U}{\Omega L} \qquad (2.2.1\text{-}6)$$

It compares horizontal advection to the Coriolis force. If R_o is large, the Earth rotation effect can be neglected, while a small Rossby number means that the system under study is strongly influenced by the Coriolis force.
Considering the order of magnitude of the characteristics scales introduced before, the order of the Rossby number is $R_o = \frac{U}{\Omega L} = \frac{1\cdot 10^{-1}}{1\cdot 10^{-4}\cdot 1\cdot 10^{4}} \simeq 0.1$

The smaller the Rossby number, the stronger the rotation effect. Similar to the Rossby number, the Froude number measures the importance of stratification. The Froude number can be derived by considering a stratified fluid characterised by a Brunt-Vaisala frequency N, flowing horizontally at a speed U, and encountering an obstacle of width L and height H (Cushman-Roisin, 1994). The stratification forces the flow to pass around the obstacle rather than over it. The time spent by a fluid particle to cover the horizontal distance L at the speed U is $T = \frac{L}{U}$. The corresponding vertical displacements are $\Delta z = WT = \frac{WL}{U}$ and cause density perturbations on the order of $\Delta\rho = \left|\frac{d\rho}{dz}\right|\Delta z = \frac{\rho_0 N^2 WL}{U}$. Density fluctuations lead to pressure perturbations that scale through hydrostatic balance as follows:

$$P = gH\Delta\rho = \frac{\rho_0 N^2 WLH}{U}$$

The pressure gradient force implies a change in fluid velocity $\left(u\frac{\partial u}{\partial x} + v\frac{\partial u}{\partial y} \sim \frac{1}{\rho_0}\frac{\partial p}{\partial x}\right)$ so:

$$U^2 = \frac{P}{\rho_0} = \frac{N^2 WLH}{U}$$

The ratio between the vertical convergence $\frac{W}{H}$ and the horizontal divergence $\frac{U}{L}$ can be calculated from the above expression as $\frac{W}{H}\frac{L}{U} = \frac{U^2}{N^2H^2}$. If U<NH, this implies that $\frac{W}{H} < \frac{U}{L}$, so the fluid is deflected horizontally, and the stronger the stratification is, the smaller is U compared to NH, and the weaker is the vertical velocity W. The ratio $\frac{U}{NH}$ is the Froude number that measures the importance of stratification.

$$F_r = \frac{U}{NH} \qquad (2.2.1\text{-}7)$$

The smaller Fr is, the more important is the stratification, analogous to the Rossby number, because the smaller Ro is, the more important are the rotational effects.

In case effects of rotation and stratification are simultaneously present and considering the geostrophic balance in the horizontal momentum equation we obtain the horizontal velocity scale $\Omega U = \frac{\Delta P}{\rho_0 L}$, hence $U = \frac{N^2 H\, \Delta z}{\Omega L}$

The ratio between vertical and horizontal convergence becomes: $\frac{W}{H}\frac{L}{U} = \frac{\Delta z}{H} = \frac{\Omega L U}{N^2H^2} = \frac{F_r^{\,2}}{R_o}$.

Since vertical divergence cannot exist without horizontal convergence ($\frac{W}{H} \leq \frac{U}{L}$), the following inequality results: $\frac{U}{NH} < \frac{NH}{\Omega L}$.

This brings to the definition of the Burger number:

$$Bu = \left(\frac{NH}{\Omega L}\right)^2 = \left(\frac{R_o}{F_r}\right)^2 \qquad (2.2.1\text{-}8)$$

This a-dimensional number measures the relative importance of rotational and stratification effects. When the Burger number is close to one, the flow is affected by both rotation and stratification.

2.2.2 Spatial analysis of data fields

One of the oldest problems in oceanography is the visualisation of dynamic processes using irregularly spaced data. Before the advent of computerised mapping techniques, horizontal mapping and contouring were done by hand. The simplest method for obtaining a gridded dataset is block averaging, which calculates the average of the available data over a rectangular grid. The increasing amount of digital data has led to the development of a newer estimation technique, objective analysis.

The objective analysis technique uses the least squares optimal interpolation method to map spatially non-uniform data to a regular set of grid values. It is based on the Gauss-Markov theorem, first introduced by Gandin (1965) in meteorology and by Bretherton (1976) in

oceanography. Interpolation is defined as "optimal" if the statistics (covariance function) of the data field are stationary and homogeneous. This means that the statistics do not change over the sample period of each map (stationary) and that the characteristics are the same over the entire data field (homogeneous). To simplify the analysis, the covariance function is isotropic, meaning that it has the same structure in all directions.

The main equations and parameters used for objective mapping are described below; the reader is referred to Bretherton *et al*. (1976) for further details.

Objective analysis estimates the value of a scalar variable θ_x over a regular grid starting from the irregularly distributed N observations φ_r at known locations x_r with r=1,2,…,N. At each point x the objective estimate θ_x is given by:

$$\theta_x = \overline{\theta_x} + \sum_r C(x, x_r) \sum_s \left[C\left(x_s, x_r\right) + IE\right]^{-1} (\varphi_s - \overline{\theta_x}) \qquad (2.2.2\text{-}1)$$

where $C(x, x_r)$ and $C\left(x_s, x_r\right)$ are data-grid and data-data covariance matrix (matrix of covariance between all pair of observations), I is the identity matrix, $IE = < \epsilon_r, \epsilon_s >$ is the normalised variance of the observation errors, E is the expected initial error of the observations (in %*100), and $\overline{\theta_x}$ is the first guess estimated as weighted average of the observations. It is assumed that the observation errors ϵ are not spatially correlated. The estimated mean $\overline{\theta_x}$ is not the arithmetic average of the observations, it is calculated so that the sum of the weights is exactly zero:

$$\sum_{r,s} \left[C\left(x_s, x_r\right) + IE\right]^{-1} \left(\varphi_s - \overline{\theta_x}\right) = 0 \qquad (2.2.2\text{-}2)$$

Two data points far apart have a greater influence on $\overline{\theta_x}$ than two data points close together.

The correlation functions $C\left(x_s, x_r\right)$ and $C\left(x, x_r\right)$ are the core of the objective analysis and are defined as follows:

$$C\left(x_i - x_j\right) = \left(1 - \frac{r^2}{A^2}\right) e^{-\frac{r^2}{2B^2}} \qquad (2.2.2\text{-}3)$$

where r is the distance between the data values (x_i and x_j) bounded by the radius of influence R_{inf} within which the observations are selected, A is the zero crossing correlation scale also called the decorrelation length, and B is the decay length scale.

2.2.3 Time-series analysis: frequency domain

To select specific processes in our study, harmonic analysis was applied to time series data. Fourier transform (FT) was used to decompose the time series into frequency components.

In its discrete forms, the Fourier transform (DFT) is:

$$Y(k) = \sum_{j=1}^{n} X(j) W_n^{(j-1)(k-1)} \qquad (2.2.3\text{-}1)$$

where X is the signal time-series, j is the discrete time, n is the transform length, k is the Fourier frequency component and W is defined as $W_n = e^{\frac{-2\pi i}{n}}$.

The corresponding power spectra is computed as $P_k = |Y(k)|^2$.

The time series of the velocity vector fields are often analysed using rotating circularly polarised components (Gonella *et al*., 1972, Mooers *et al*., 1973, Denbo and Allen 1984, Chen *et al*., 1996). First, the complex horizontal velocity vector is defined by combining the zonal (u) and meridional (v) component of the currents as w(t)=u(t)+iv(t) .

Positive values of ω indicate counterclockwise (CCW) motion, whereas negative angular frequency, (ω≤0), indicate a clockwise (CW) motion . The relative magnitude of the two components determines the vector rotation (CW or CCW) with time.

The complex horizontal velocity vector is then expressed as the sum of the two complex rotary components $w(t) = \sum_k [W_k^+ e^{i\omega_k t} + W_k^- e^{-i\omega_k t}]$ where ω_k is the angular frequency of the kth Fourier component and t is the time. It can be written in terms of Fourier transform components.

$$w(t) = \sum_k \{[A_{1k} cos\,(\omega_k t) + B_{1k} sin\,(\omega_k t)] + i[A_{2k} cos\,(\omega_k t) + B_{2k} sin\,(\omega_k t)]\} \qquad (2.2.3\text{-}2)$$

where A_1 and B_1 are the amplitudes of the cosine and sine terms for the zonal component (u) and A_2 and B_2 are the amplitudes for the meridional component (v).

The amplitudes of the CCW and CW rotation components (A^+ and A^-, respectively) and their phase (ε^+ and ε^-, respectively) for each kth frequency component are:

$$A^+ = \frac{1}{2}\left\{\left[B_2 + A_1\right]^2 + \left[A_2 - B_1\right]^2\right\}^{1/2} \qquad (2.2.3\text{-}3)$$

$$A^{-} = \frac{1}{2}\left\{\left[B_2 - A_1\right]^2 + \left[A_2 + B_1\right]^2\right\}^{1/2} \quad (2.2.3\text{-}4)$$

$$\varepsilon^{+} = tan^{-1}\left[A_2 - B_1\right] / \left[A_1 + B_2\right] \quad (2.2.3\text{-}5)$$

$$\varepsilon^{-} = tan^{-1}\left[B_1 + A_2\right] / \left[A_1 - B_2\right] \quad (2.2.3\text{-}6)$$

where k subscript is omitted.

The one-sided spectra for the two oppositely rotating components for frequencies $f_k = \frac{\omega_k}{2\pi}$ are:

$$S^{+} = \frac{(A^{+})^2 \Delta t}{q} \quad (2.2.3\text{-}7)$$

$$S^{-} = \frac{(A^{-})^2 \Delta t}{q} \quad (2.2.3\text{-}8)$$

where q is the total number of the Fourier components and Δt is the temporal resolution.

To improve the statistical reliability of the spectra, a smoothing method is applied. It reduces the scattering loss of the observed spectral peaks and the low-frequency components of the time series (Thomson and Emery, p. 466). A common technique, called block averaging, involves dividing the original time series into a series of equally long, shorter segments in which the data can be weighted by a specific window. Spectra are calculated for each segment, and the final autospectrum is obtained by averaging the values associated with each frequency. Note that the minimum resolvable period 2Δt (reciprocal of the Nyquist frequency) remains the same because the sampling period Δt is unchanged, but the temporal resolution between adjacent spectral estimates is reduced due to the shorter recording lengths of each segment. Adjacent segments can be overlaid to achieve more uniform weighting of individual data points.

Because preliminary analysis of the LOGMEC17 data set reveals strong processes with a period close to the theoretical inertial period (17.3 h), the length of the segments was set to four times the inertial period (~ 3 days) to ensure that the spectra for these high-frequency processes were reliable. Tests were performed with different overlapping windows, with the best overlap being 50% of the window. The sampling period Δt of the current measurement is 15 minutes for both moorings. The near-coastal mooring collected data for 28 days and the deep mooring for 60 days. The mean and trend were removed before applying the discrete Fourier transform (DFT) to the current time series. For efficient processing of DFT, the transformation length n is equal to a power of 2. Since the transformation length n is greater than the number of data within a segment, zero padding is applied. Interpolation between the frequency components of a transform not padded with zeros is performed to smooth the shape of the spectrum. While this technique does not improve temporal resolution, it does help distinguish spectral peaks.

In the northern hemisphere, inertial motions rotate clockwise (Thomson and Emery, p. 454), so only the clockwise components of the spectra (CW, $\omega < 0$) are considered in this study.

To better characterise NIWs, their phase propagation through the rotary inner-coherence between two current time series observed at different depths is investigated.

We can distinguish the CCW and CW rotary components and their amplitudes and phase are denoted by A^+, ε^+ (CCW) and A^- , ε^- (CW), respectively. The inner rotary coherence squared between time-series 1 and 2 is defined as follows:

$$\gamma_{12}^2 = \frac{\langle A_1^+ A_2^+ cos(\varepsilon_1^+ - \varepsilon_2^+)\rangle^2 + \langle A_1^+ A_2^+ sin(\varepsilon_1^+ - \varepsilon_2^+)\rangle^2}{\langle A_1^+\rangle^2 \langle A_2^+\rangle^2} \quad \text{for } \omega \geq 0 \tag{2.2.3-9}$$

$$\gamma_{12}^2 = \frac{\langle A_1^- A_2^- cos(\varepsilon_1^- - \varepsilon_2^-)\rangle^2 + \langle A_1^- A_2^- sin(\varepsilon_1^- - \varepsilon_2^-)\rangle^2}{\langle A_1^-\rangle^2 \langle A_2^-\rangle^2} \quad \text{for } \omega \leq 0 \tag{2.2.3-10}$$

where $\langle\,\rangle$ denotes the ensemble average over some specified averaging time.

Small coherence values, close to zero, indicate a low correlation between the two like-rotating series, while high coherence implies a strong relationship between the two.

The inner rotary phase lag $\phi_{12}(\omega)$ of the vectors 1 with respect to that of vector 2 is:

$$\phi_{12}(\omega) = \frac{\langle A_1^+ A_2^+ sin(\varepsilon_1^+ - \varepsilon_2^+)\rangle}{\langle A_1^+ A_2^+ cos(\varepsilon_1^+ - \varepsilon_2^+)\rangle} \text{ for } \omega \geq 0 \tag{2.2.3-11}$$

$$\phi_{12}(\omega) = \frac{\langle -A_1^- A_2^- sin(\varepsilon_1^- - \varepsilon_2^-)\rangle}{\langle A_1^- A_2^- cos(\varepsilon_1^- - \varepsilon_2^-)\rangle} \text{ for } \omega \leq 0 \tag{2.2.3-12}$$

Since NIWs rotate clockwise ($\omega \leq 0$) and the theoretical inertial period is 17.3 hours, the analysis is performed only for 17.3 hours. The confidence level for the inner coherence squared is calculated as follows (Emery & Thomson p. 510):

$$\gamma_{1-\alpha}^2 = 1 - \alpha^{\frac{2}{DoF-2}} \tag{2.2.3-13}$$

where α is 0.05 for calculating the confidence level of 95% and DoF indicates the Degrees of Freedom. The latter is defined as two times the number of independent adjacent segments into which the time series is divided for the calculation of coherence, but in the case of segments that overlap, the DoF is four times the number of segments.

Wavelet analysis

The Fourier transform provides an averaged estimate of amplitude and phase for each frequency component, while the wavelet transform produces an "instantaneous" estimate of amplitude and phase that allows examination of time evolution.

The continuous wavelet transform of a signal x(t) is:

$$W_{\psi}(t,s) = \int_{-\infty}^{\infty} \frac{1}{s^n} \psi^* \left(\frac{\tau - t}{s}\right) x(\tau)\, d\tau \qquad (2.2.3\text{-}14)$$

where the asterisk denotes the complex conjugate, *s* is the wavelet scale that dilates or compresses a given wavelet, ψ is the wavelet function. If the scale normalisation is equal to one the equation (2.2.3-9) is a set of bandpass operations, while if n=0.5 it is seen as a set of projections, indexed by the scale parameter *s* (Lilly & Olhede, 2012).

Several wavelet functions exist but in the present study we use the generalised Morse wavelets defined in the frequency domain as follows:

$$\psi_{\beta,\gamma}(\omega) = \int_{-\infty}^{\infty} \psi_{\beta,\gamma}(t) e^{-i\omega t} dt = U(\omega)\, a_{\beta,\gamma}\, \omega^{\beta} e^{-\omega\gamma} \qquad (2.2.3\text{-}15)$$

where ω is the frequency, $U(\omega)$ is the unit step function, $a_{\beta,\gamma}$ is a normalisation constant, β and γ are parameters for controlling the wavelet shapes, which are defined as default values 3 and 20, respectively.

The continuous wavelet transform is usually approximated by Fourier space, since this is a much faster method. Before applying the discrete Fourier transform (DFT) to the time series, the mean and trend are removed. Using the convolution theorem, the wavelet transform is the inverse Fourier transform.

The generalised Morse function ψ is complex, which means that the wavelet transform is also complex. Analogous to rotary spectra, the wavelet transform of the current time series can be determined in terms of clockwise and counterclockwise components (Liu and Miller, 1996).

By defining the wavelet transform of the Cartesian components $\widetilde{u}$ and $\widetilde{v}$ as the sum of their real and imaginary part $\widetilde{u}(\omega,t) = \widetilde{u}_r(\omega,t) + i\widetilde{u}_i(\omega,t)$, the counterclockwise ($\left|U_+(\omega,t)\right|^2$) and clockwise ($\left|U_-(\omega,t)\right|^2$) wavelet power spectra are calculated as follows:

$$\left|U_+(\omega,t)\right|^2 = \left[\widetilde{u}_r(\omega,t) - \widetilde{v}_i(\omega,t)\right]^2 + \left[\widetilde{u}_i(\omega,t) + \widetilde{v}_r(\omega,t)\right]^2 \qquad (2.2.3\text{-}16)$$

$$\left|U\_(\omega,t)\right|^2 = \left[\widetilde{u}_r(\omega,t) + \widetilde{v}_i(\omega,t)\right]^2 + \left[\widetilde{u}_i(\omega,t) - \widetilde{v}_r(\omega,t)\right]^2 \quad (2.2.3\text{-}17)$$

Since the NIWs rotate clockwise, and the inertial period is about 17.3 hours, the inertial power is defined as $\left|U\_(\omega,t)\right|^2$ with $\omega = \frac{1}{17.3}$cph.

Band pass filter

To quantify the contribution of different processes to the variability of a selected variable, a bandpass filter is often applied to the representation in the frequency domain *Y*. If F_s is the sampling frequency and $dF = \frac{F_s}{n}$ (ratio between sampling frequency and transform length n), the frequency vector of the Discrete Fourier Transform starts at $-Fs/2$ and ends at $Fs/2\text{-}dF$ with steps of *dF*. The band pass filter is defined as the vector frequency between a lower and an upper frequency limit (user defined). This filter multiplies the frequency domain representation *Y*, preserving only the values within the lower and upper frequency limits (Y_F).

After applying the band pass filter, the inverse Fourier transform X_F is performed on the filtered time-series:

$$X_F(j) = \frac{1}{n}\sum_{k=1}^{n} Y_F(k) W_n^{-(j-1)(k-1)}$$

where letter *F* indicates the filtered signal.

2.3 Numerical model

The numerical ocean model implemented in this study is based on the Nucleus for European Modelling of the Ocean (NEMO) version 4.0.4 (Madec *et al*., 2019). NEMO is a flexible tool for studying the dynamics and thermodynamics of the ocean and its interaction with components of the Earth's climate system.
A two-way nesting system is also available to allow adaptive grid refinement to increase horizontal resolution in specific regions of interest using Adaptive Grid Refinement in Fortran (AGRIF) software (Debreu *et al*., 2008). The coarser grid feeds the open boundaries of the finer grid, while the latter provides volume averages of the prognostic variables to the coarser grid, which is why it is referred to as "two-way nesting". The latter technique is used in this study to achieve adequate horizontal resolution in the experimental area.

The model NEMO solves the three-dimensional primitive equations and a nonlinear equation of state used to relate temperature and salinity (active tracers) to the momentum equation. The following approximations are used to simplify the equations. The spherical Earth hypothesis, where gravity is assumed to be parallel to the Earth's radius; the ocean shell hypothesis, since the ocean depth is much smaller than the Earth's radius; the turbulent closure hypothesis, since turbulent fluxes are parameterized; the Boussinesq approximation, where density changes are neglected except for their contribution to the buoyancy force; the incompressibility hypothesis ($\nabla \cdot U = 0$); hydrostatic hypothesis, which reduces the vertical momentum equation to $\frac{\partial p}{\partial z} = -\ \rho g$, which is why the convective processes must be parameterized.

The model implemented in the present study, the Ligurian Sea Model (LISM hereafter), has a coarser domain, called parent domain, with a horizontal resolution of about 1.3 km, and a two-way nested domain, so-called child domain, which reaches 400 m in the experimental area. Both domains share a vertical grid of 141 unevenly spaced levels discretized with z* partial steps (Barnier *et al*., 2006). The z* coordinate system (Adcroft and Campin, 2004) follows the variation in sea surface elevation, so the variation in layer thickness due to sea surface undulations is distributed throughout the water column. A full description of the z*-coordinate system is given in a report (Levier *et al.*, 2007).

In order to optimise the computation time, the slow and fast processes are solved using a time splitting technique, i.e. the barotropic and baroclinic dynamic equations are solved separately with different time steps. In the parent model, the time step for the baroclinic component is 150 s, while in the child it is 50 s and the barotropic part is calculated in 40 and 20 subloops, respectively.

In ocean models, the effects of small-scale motions resulting from the advective terms of the Navier-Stokes equations must be represented in terms of large-scale patterns to close the

equations. This is what is known as subgrid scale physics and provides the stability to the model by dissipating the energy that cascades to the grid level. Since gravity causes a strong difference between the horizontal and the vertical direction, the subgrid scale physics is divided into lateral and vertical parts. Vertical turbulence occurs at scales much smaller than the vertical model resolution, which is why it is never explicitly solved, but parameterized. The parameterizations used in this study are described below.
The advection scheme for active tracers is the 4th order Flux Correct Transport scheme (Zalesak, 1979) and horizontal diffusion is solved by a bi-laplacian operator along iso-neutral surfaces. A 3rd order upstream scheme (Shchepetkin and McWilliams, 2005) is used to solve the advective terms of the momentum equation, while for the viscous term a bi-laplacian operator is activated along the iso-level surfaces.

To ensure numerical stability and minimise numerical dissipation, the horizontal diffusivity and viscosity values are uniform in the interior of the model domain ($5 \cdot 10^5$ m^4s^{-1} and 10^6 m^4s^{-1}, respectively) and double starting from ten grid points near the coast and at the lateral open boundaries. The atmospheric pressure term is added to the governing equations to be consistent with the Copernicus Marine Environmental Monitoring Service (CMEMS) (Le Traon *et al*., 2019) Mediterranean Sea operational model (its products are used as lateral open boundary conditions as described in detail in Chapter 5). The lateral open boundary conditions (LOBCs) are one-way nested with a procedure that uses a Flather formula (Flather *et al*., 1976) for barotropic velocities, a flow relaxation scheme for baroclinic velocities, and a radiation scheme for active traces (Oddo and Pinardi, 2008).

The vertical turbulence coefficients are calculated using the Generic Length Scale turbulence closure scheme (Umlauf and Burchard 2003, 2005), where the generic length scale is calculated using a k-kl turbulence closure (Mellor and Yamada 1982).

In LISM, eight major components (Q1, O1, P1, K1, N2, M2, S2, and K2) of tidal elevations and velocities from TPXO (Padman and Erofeeva, 2004) are superimposed on the lateral open boundary conditions, and the tidal potential is added to the surface pressure gradient calculations.

The surface heat flux is adjusted with the satellite level 4 Sea Surface Temperature provided by CMEMS using a Newtonian relaxation algorithm. A retroaction term is added to the surface heat flux using a flux formulation. The light extinction coefficient (Lengaigne *et al*., 2007) is calculated using the chlorophyll satellite products provided monthly by CMEMS. Surface boundary condition fields are calculated using the COARE 3.5 algorithm (Edson *et al*., 2013), starting from the atmospheric fields of air temperature, humidity, winds, and cloud cover provided by the European Centre for Medium-Range Weather Forecasts (ECMWF). No-slip boundary condition is imposed on the lateral momentum, which means that the tangential velocity vanishes at the coastline. The bottom friction caused by bathymetry is parameterized by a logarithmic layer (log-layer bottom friction) where the drag coefficient depends on the distance to the bottom.

3. Environmental characterization

The previous chapter presented the data set and the methods used to achieve the goal of the thesis, both from the data analysis and modelling point of view. In the present chapter we focus on the environmental characterization during the LOGMEC17 sea trial, starting with the dimensionless analysis that allows us to identify the characteristic scales in the studied area. The large-scale circulation and its variability are studied by combining satellite and glider data, while the mesoscale and submesoscale are characterised using ScanFish data.

3.1 Characteristic scales

A-dimensional numbers such as the Rossby (2.2.1-6), Froude (2.2.1-7), and Burger (2.2.1-8) numbers are calculated to characterise the area under study.

As described in Section 2.2.1, these numbers help identify the dominant processes and simplify the governing equations of motion. The Rossby number measures the importance of the rotational effect: the smaller the Rossby number, the stronger the rotational effect. Analogous to the Rossby number, the smaller the Froude number, the stronger the stratification.

The Burger number measures the relative importance of rotation and stratification effects. If the Burger number is close to one, the flow is influenced by both rotation and stratification.

To calculate the dimensionless numbers, the magnitude of the local inertial frequency ϕ, the current magnitude U, the horizontal (H) and vertical (L) scales, and the Brunt-Vaisala frequency (N) are first estimated.

The theoretical inertial frequency depends on the latitude ϕ: $f=2\,\Omega\,sin(\phi)$. Coriolis parameter at Ligurian basin latitudes is 10^{-4} s^{-1} and the magnitude of ocean currents is 0.1 m s^{-1} (Robinson *et al*., 2001; Millot and Taupier-Letage, 2005), as confirmed by *in situ* observations during LOGMEC17. Rossby, Froude, and Burger numbers are calculated at the two moorings, as shown in Table 3.1-1. The horizontal and vertical length scales at the deep mooring are 100 km and 1000 m, respectively, the same orders of magnitude as the length scales characteristic of the Ligurian Basin. The vertical length scale of 1000 m was chosen because it corresponds to bathymetry at the deep mooring, while the horizontal scale is 100 km because we assume that we are covering the large-scale structures at the deep mooring. Instead, at the near-coastal mooring, the dimensionless numbers are calculated with horizontal and vertical length scales of 10 km and 100 m, respectively, because 10 km is the order of magnitude of the Rossby radius of deformation in the western Mediterranean Sea (Grilli and Pinardi, 1998; Beuvier *et al.*, 2012; Escluder *et al*., 2016) and 100 m is the water depth at the near-coastal mooring.

To calculate the Froude number, the Brunt-Vaisala frequency time series (Figure 3.1-1) is derived from the temperature and salinity values measured by the two moorings along the water column.

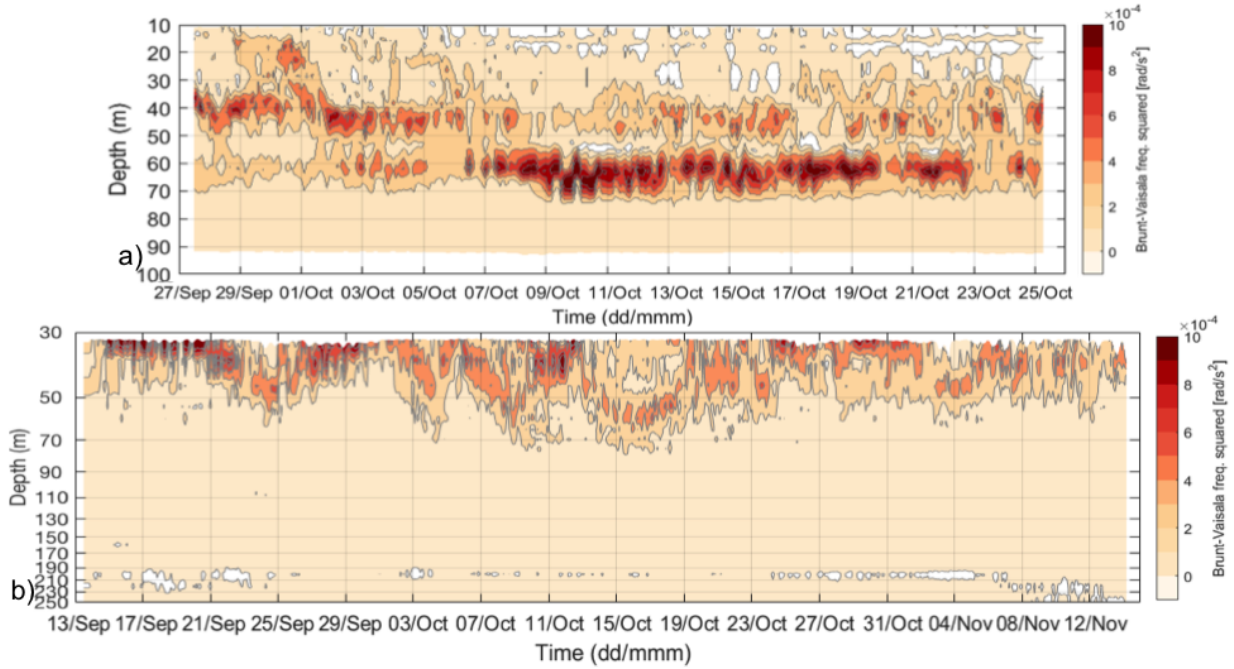

Figure 3.1-1: Brunt-Vaisala frequency squared from 27 September to 25 October at near-coastal (a) and from 13 September to 13 November at the deep mooring (b). In panel b the logarithmic scale is used for the y-axis. Values are averaged every 2 hours. Contour lines from -10^{-4} to 10· 10^{-4} every 2· 10^{-4} are shown.

Mooring	**U (m s^{-1})**	**H (m)**	**L (km)**	**Brunt-Vaisala frequency** ($rad\ s^{-2}$)	**R_o**	**F_r**	**Bu**
Deep	0.1	1000	100	$0.9 \cdot 10^{-4}$	0.01	0.0105	0.91
				$1.8 \cdot 10^{-3}$	0.01	0.0024	18
Near-coastal		100	10	$1.8 \cdot 10^{-4}$	0.1	0.0745	1.8
				$1.6 \cdot 10^{-3}$	0.1	0.025	16

Table 3.1-1: U is the horizontal velocity and H,L are the vertical and horizontal scales used to calculate the dimensionless numbers. Rossby (Ro), Froude (Fr) and Burger (Bu) numbers at the two moorings. The first and third rows represent the values calculated using the averaged Brunt-Vaisala frequency values for the deep and near-coastal mooring, respectively, and the second and fourth rows using the maximum Brunt-Vaisala frequency.

At the deep mooring (Figure 3.1-1b), strong stratification is found in the upper layers, whereas at the near-coastal mooring (Figure 3.1-1a), it is in the intermediate layers. For the deep mooring, Brunt-Vaisala frequency values are shown down to a depth of 250 m where the ADCP was moored. Values below 250 m are not shown because they are low and nearly constant and are not used in the present study.

At the near-coastal mooring the mean value of the Brunt-Vaisala frequency from 27 September

to 25 October between 15 and 90 m is $1.8 \cdot 10^{-4}$ rad s^{-2}. The highest values, about 10^{-3} rad s^{-2}, occur from 06 to 20 October between 60 and 70 m depth. Different Brunt-Vaisala frequency profiles are found at the deep mooring (Figure 3.1-1b). At the deep mooring, the average of the Brunt-Vaisala frequency from 14 September to 14 November between 30 and 250 m is 10^{-4} rad s^{-2}. From the first available layer, about 30 m, to 80 m depth, the value ranges from 10^{-3} to 10^{-4} rad s^{-2}, while lower values are found below 80 m depth. At the deep mooring from 14 to 22 September, the highest values, 10^{-3} rad s^{-2}, occur at about 35 m depth, then the values decrease and the maximum value increases to 50 m depth on 24 September. The highest values continue to vary between 30 (shallowest depth of available data) and 60 m depth during the sampling period. The Brunt-Vaisala frequency from 15 to 18 October is $2 \cdot 10^{-4}$ rad s^{-2} at about 30 m depth, decreases at 45 m depth, then increases to values of $5 \cdot 10^{-4}$ rad s^{-2} between 50 and 60 m depth, and decreases again below 60 m depth. Overall, these values are comparable to the averaged Brunt-Vaisala frequency profile in the Ligurian Sea calculated using data from 2001 to 2010 (Fratianni *et al*., 2016) in autumn. The latter study shows that the mean profile in autumn assumes maximum values around $2 \cdot 10^{-4}$ rad s^{-2} at 30 m depth and decreases toward the bottom.
As shown in Table 3.1-1, the Rossby, Froude, and Burger numbers are calculated using two different Brunt-Vaisala frequency values for each mooring. The first and third rows of Table 3.1-1 are calculated using the Brunt-Vaisala frequency averaged over the water column at the deep and near-coastal mooring, respectively. At the deep mooring, the averaged Brunt-Vaisala frequency is $0.9 \cdot 10^{-4}$ rad s^{-2} and at the near-coastal mooring, the average value is $1.8 \cdot 10^{-4}$ rad s^{-2}. To examine how stratification affects the dimensionless numbers, the maximum Brunt-Vaisala frequency that occurred during LOGMEC17 is used to calculate the numbers given in the second and fourth rows of Table 3.1-1 at the deep and near-coastal mooring, respectively. The highest Brunt-Vaisala value at the deep mooring, $1.8 \cdot 10^{-3}$ rad s^{-2}, was measured at 32 m depth at 02:00 on 17 September. At the near-coastal mooring, the maximum Brunt-Vaisala frequency, $1.6 \cdot 10^{-3}$ rad s^{-2}, occurred on 10 October 02:00 at 63 m depth.

The magnitude of the Rossby number at the deep mooring (0.01) is consistent with that obtained with the LOGMEC16 dataset in the Ligurian Sea (Ro=0.03) (Borrione *et al*., 2019). The Froude and Rossby numbers using the averaged Brunt-Vaisala frequency value at the deep mooring (first row in Table 3.1-1) are both 0.01, so the Burger number is close to 1. This means that the stratification and rotational effects are equally important.

The choice of the Brunt-Vaisala frequency value strongly affects the Froude and consequently the Burger numbers. In particular, when the maximum Brunt-Vaisala frequency values are used (second and fourth rows in Table 3.1-1), the Burger number is an order of magnitude higher (18 and 16 for the deep and near-coastal mooring, respectively) than when the averaged values are used (0.91 and 1.8, respectively), indicating a significant influence of the stratification effect over the rotation effect. The Rossby and Froude numbers at the near-coastal mooring are almost an order of magnitude higher than at the deep mooring (third and fourth rows in Table 3.1-1). Based on these a-dimensional numbers, we likely have different regimes at the two mooring

locations, but overall the Rossby, Froude, and Burger numbers suggest a quasi-geostrophic regime (Maksimova, 2018).

Another method of calculating the Rossby number is based on vorticity. One estimate of the Rossby number is the ratio between relative vorticity ζ and planetary vorticity f.

$$R_o = \frac{\zeta}{f}$$

Based on the geostrophic velocity derived from satellite measurements provided by the Copernicus Marine Environmental Monitoring Service (CMEMS), the relative vorticity is calculated as the curl of the horizontal velocity vector u.

$$\zeta = \nabla \times u$$

To estimate the Rossby number during the LOGMEC17 campaign, a map of averaged values over the two-month period is examined (Figure 3.1-2).

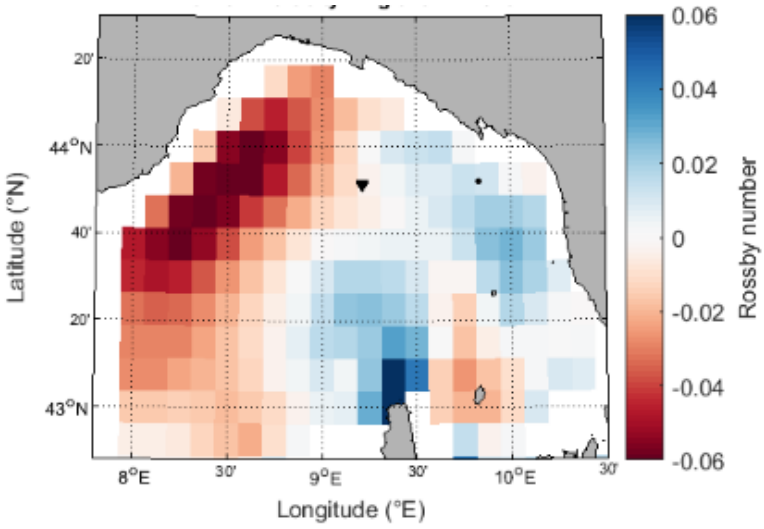

Figure 3.1-2: Rossby number averaged from 14 September to 14 November. Black dot and black triangle indicate near-coastal and deep moorings, respectively.

Negative numbers are due to negative vorticity values. The maximum Rossby number averaged over the two months in the Ligurian Sea is 0.06. The time series of Rossby numbers are analysed at the locations of the two fixed moorings (Figure 3.1-3). The time series show a difference in vorticity at the sites of the two moorings, except from 9 to 11 October. The maximum Rossby number during the LOGMEC17 campaign at the two fixed moorings is 0.03, which is on the same order of magnitude as the Rossby number calculated using the traditional equation at the deep mooring (first and second rows in Table 3.1-1). This analysis confirms previous results, as the Rossby number at both moorings is much smaller than 1, indicating strong rotational effects.

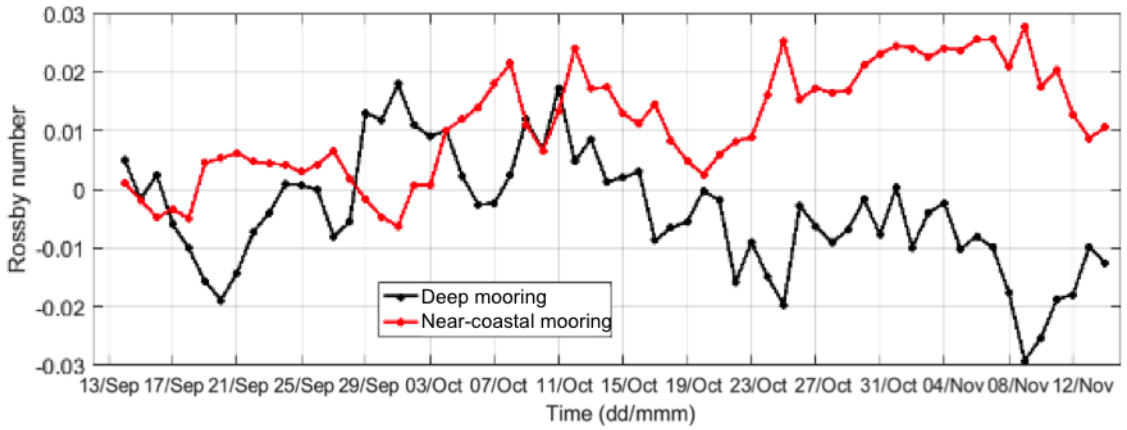

Figure 3.1-3: Rossby number estimated from geostrophic velocity time series near the deep (black line) and near-coastal (red line) mooring.

3.2 Large scale circulation and water masses

The large-scale of the LOGMEC17 area is characterised by combining the gridded satellite-based sea level data provided by Copernicus Marine Environmental Monitoring Service (CMEMS) (Pujol et al., 2016) and data collected by gliders.

The satellite measures the Sea Surface Height (SSH) above the reference ellipsoid and its temporal mean is called Mean Sea Surface (MSS). The Sea Level Anomaly (SLA) is the anomaly of the signal with respect to its mean (SLA=SSH-MSS). The Mean Dynamics Topography (MDT) is the MSS above the geoid over a selected period.

The Absolute Dynamic Topography (ADT) is the instantaneous height above the Geoid which corresponds to the idealised ocean surface at rest (with no currents, under the gravity field only). The ocean surface moved from the geoid due to wind, different heat and precipitation distribution and other sources of energy. The ADT is the sum of the SLA and MDT (ADT=SLA+MDT). The spatial resolution of the gridded product (L4) used in the present study is 1/8° (10 km and 14 km in the zonal and meridional directions, respectively) and the temporal resolution is daily. Therefore, we can use this product to study the dynamics on a horizontal scale larger than 10 km.

Major water masses and large-scale circulation during LOGMEC17 are studied by combining satellite data averaged over 10 days and data collected by gliders. Time-averaged gridded Absolute Dynamic Topography (ADT) and geostrophic velocities during LOGMEC17 (from 14 September to 13 November) in the experimental area are analysed (Figure 3.2-1).

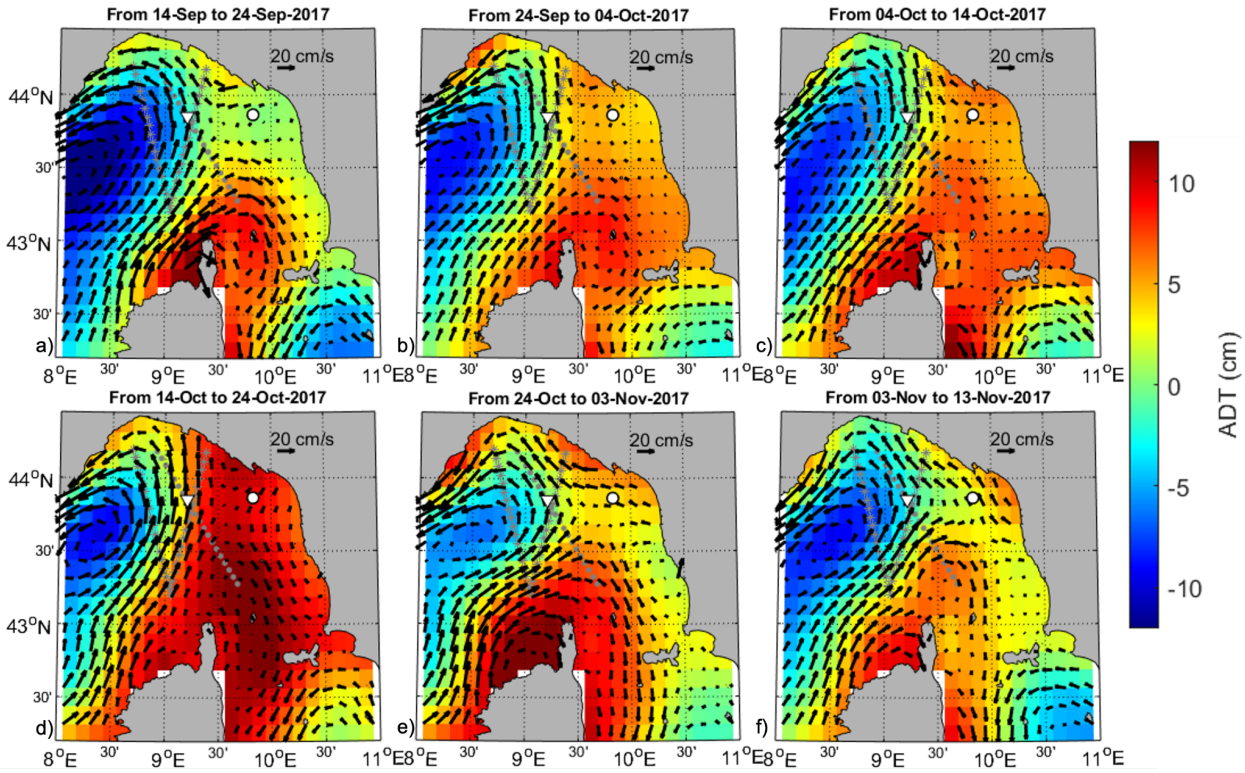

Figure 3.2-1: ADT and geostrophic velocity (black arrows) averaged over 10 days from 14 September (upper left) to 13 November (bottom right). Dots and asterisks indicate the Jason3 and Sentinel-3A satellite tracks along which the gliders collected data. Tracks number 44 are shown in magenta and Sentinel-3A track number 85 is shown in grey. Deep and near-coastal mooring are indicated by white triangle and dot, respectively.

The WCC, LPCC, and GLG characterising the Ligurian Sea (see 1.2: Ligurian Sea Background) are clearly identified throughout the LOGMEC17 experiment and their variability is described below. The ECC has a peculiar behaviour with respect to literature, it does not always flow northward. South of 42.6°N, the current East of Corsica flows southward throughout the LOGMEC17 campaign.

The deep mooring is mostly located at the LPCC boundary, while the near-coastal mooring is not directly affected by the LPCC. During the entire LOGMEC17 experiment, the WCC splits north of the island of Corsica to form the LPCC, which turns counterclockwise and partially clockwise along the east side of Corsica to the south. At the deep mooring, the mean ADT is low and is strongly influenced by the LPCC with a mean geostrophic velocity of 25 cm s^{-1}, while at the near-coastal mooring the mean ADT is about 5 cm and the mean geostrophic velocity is close to zero. A strong cyclone, characterised by a mean ADT of -12 cm, is located in the northwestern area and a weaker one in the southeastern part of the studied area.

The centre of the cyclonic gyre (GLG) moves northeasterly during the LOGMEC17 campaign. The first 10 days, from 14 to 24 September, are characterised by a strong WCC (40 cm/s) splitting north of the Corsica island (43.5°N, 9.5°E) and forming the LPCC, which rotates counterclockwise around the negative ADT (up to -12 cm/s), the GLG cyclone, while part of the WCC rotates clockwise and forms an anticyclone northeast of Corsica. At the near-coastal mooring, the ADT and geostrophic current are near zero but it could also be due to the low resolution of satellite data. From 24 September to 14 October (Figure 3.2-3b,c), the large-scale circulation is similar to the first 10 days, but the geostrophic currents are weaker, the WCC intensity is half (20 cm/s), and the point where the WCC splits into an LPCC and an anticyclonic circulation shifts northward. Beginning on 14 October (Figure 3.2-3d), ADT increases sharply at longitudes and latitudes above 9.2°E and 42.5°N, respectively, and the highest ADT value, 12 cm, indicates a strong anticyclone around the island of Capraia. At the deep mooring, the geostrophic flow is northward, while at the near-coastal mooring is southward. From 24 October (Figure 3.2-3e,f), the cyclone moves northeastward and the geostrophic flow at the deep mooring remains the same as in the previous 10 days, while at the near-coastal mooring it becomes northwesterly and the LPCC forms meanders (in agreement with the literature).

The observed changes in the GLG, LPCC, and WCC affect the LOGMEC17 area in terms of the input of water masses reaching this area.

The water masses in the LOGMEC17 area and their variability are studied by analysing data collected from the deep mooring and the gliders that followed the satellite tracks. The deep mooring is located at the intersection of the Jason-3 and Sentinel-3a tracks.

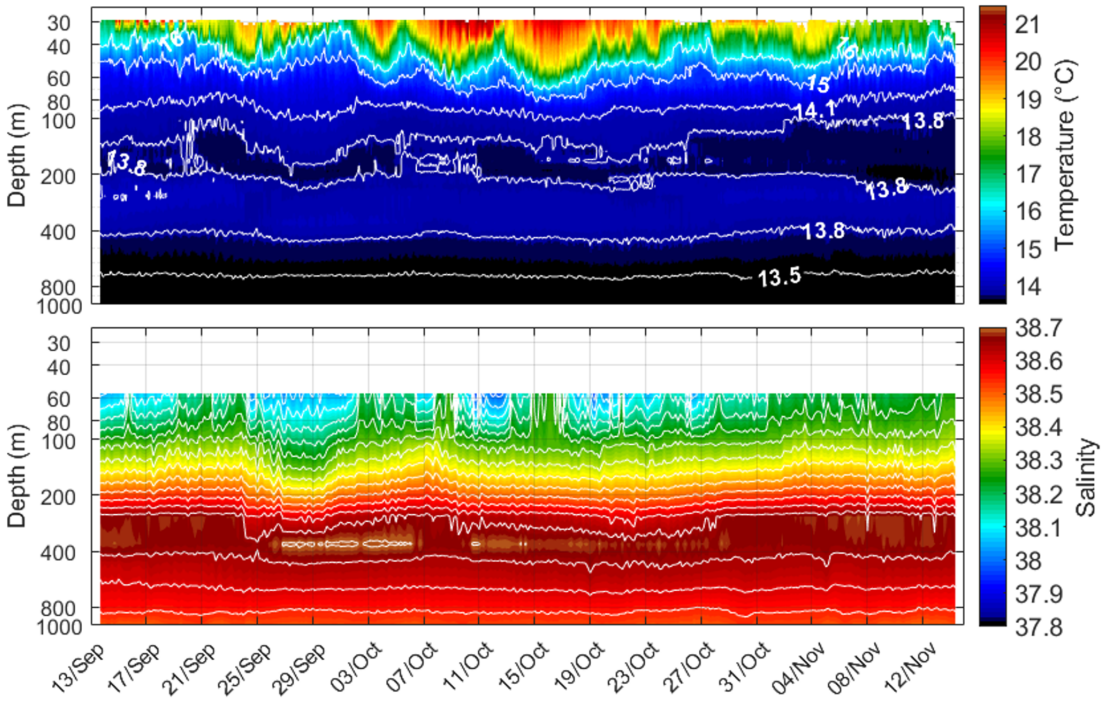

Figure 3.2-2: Time series of temperature (top) and salinity (bottom) reconstructed from deep mooring measurements. Isotherms are indicated by white lines and labelled, while isohalines are plotted every 0.05. Note that salinity sensors (SBE) are sparse (see Table 2); all salinity-derived values are rough approximations based on linear approximation. To better illustrate the isosurface, the y-axis is shown in logarithmic scale (depth).

At the deep mooring (Figure 3.2-2), the temperature reaches 21°C in the surface layers. Unfortunately, salinity data are not available above 60 m depth, but we can identify the Modified Atlantic Water (MAW) from 60 to 80 m depth, characterised by a low salinity of 37.8-38 and a temperature ranging from 14 to 15.5°C. Below 80 m depth, the temperature decreases (13.8-14°C) while the salinity increases (38.2-38.4); this water mass could be of Tyrrhenian origin, while from 200 to 400 m depth the warmer and saltier water mass (38.6-38.7 and 13.8-14°C) indicates the presence of Modified Levantine Intermediate Water (MLIW). The bottom layer below 400 m depth is characterised by a temperature between 13.3 and 13.8°C and a salinity of 36.5 - 36.65, which is typical of Western Mediterranean Deep Water (WMDW).

At the beginning of data collection, the Modified Levantine Intermediate Water (LIW) core is characterised by a temperature of 14 °C and a salinity of 38.65-38.7 between 200 and 400 m depth and increases in depth between 300 and 400 m depth from 26 September to 04 October. The values for temperature and salinity are consistent with MLIW characteristics reported in the literature (Millot *et al.*, 2013; Bosse *et al.*, 2015; Borrione *et al.*, 2019). In October, the MLIW core temperature drops 0.2°C by the end of the month and then rises again to 14°C at about 250 m depth. These fluctuations are related to the changes in circulation observed by the satellite (Figure 3.2-1), as the mooring located at the intersection of the satellite tracks is affected by

GLG, WCC, and LPCC. Indeed, the GLG moves westward during the second half of October. Moreover, the characteristics of the MLIW core from 14 to 24 October and from 27 October to 04 November are consistent with a similar circulation observed by the satellite near the deep mooring (Figure 3.2-1a,e).

In support of the data collected by the deep mooring, gliders help characterise also the surface layers not covered by mooring. The analysis of the glider data also allows the study of the circulation of the main water masses in the Ligurian basin and their variability during the LOGMEC17 campaign. The gliders used during the LOGMEC17 sea trial were programmed to follow the tracks of the altimetry satellites (Jason-3 and Sentinel-3A). The LOGMEC17 sampling strategy allows multiple glider data to be collected along tracks that are co-located and near-contemporaneous with the satellite transit (Table 3.2-1).

Satellite name	Track n.	Time of transit
Jason-3	44	26/Sep/17
Sentinel-3A	44	02/Oct/17
Sentinel-3A	85	03/Oct/17
Jason-3	44	06/Oct/17
Jason-3	44	15/Oct/17
Sentinel-3A	44	29/Oct/17
Sentinel-3A	85	30/Oct/17
Jason-3	44	04/Nov/17

Table 3.2-1: Date and time of selected satellite tracks during LOGMEC17.

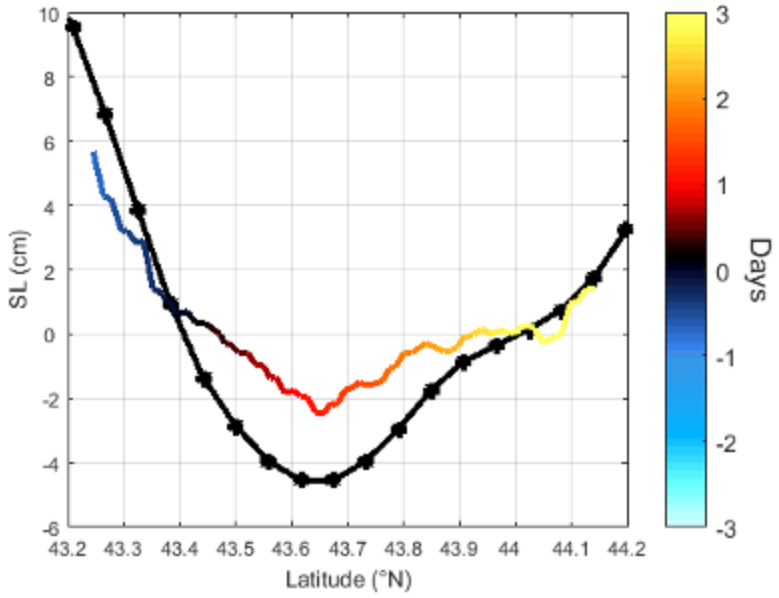

Figure 3.2-3: Altimeter-filtered ADT (black line) and glider-derived DH along satellite track number 85 of Sentinel-3A on 30 October. The DH line is colour coded to reflect the difference between the time of satellite transit and the time of glider measurements.

A first consistency check between glider and satellite is performed by comparing the altimeter filtered ADT and Dynamic Height (DH) calculated from the glider profiles along the satellite tracks. Overall, satellite-derived ADT and glider-derived DH show similar patterns (an example in Figure 3.2-3). The DH is determined by integrating water density derived from glider temperature and salinity measurements from the surface to a reference level. Sensitivity tests show that good agreement is found between ADT and DH when 200 m is used as the reference depth, in agreement with previous studies (Tintore' et al., 1988; Ruiz et al., 2009; Borrione et al., 2016), suggesting that most of the dynamics responsible for sea level variability were captured within 200 m (Figure 3.2-4 to Figure 3.2-6).

The MAW, MLIW, and WMDW are clearly identified by the gliders, similar to the deep mooring observations, and the T-S diagrams (not shown) at the time of the sea trial are consistent with the T-S diagram typical of the Ligurian Sea in autumn (Cruzado *et al*., 2012; Aracri *et al*., 2016). Temperature and salinity profiles collected by the gliders are grouped for each satellite track. The variability of the identified water masses during LOGMEC17 is examined below.

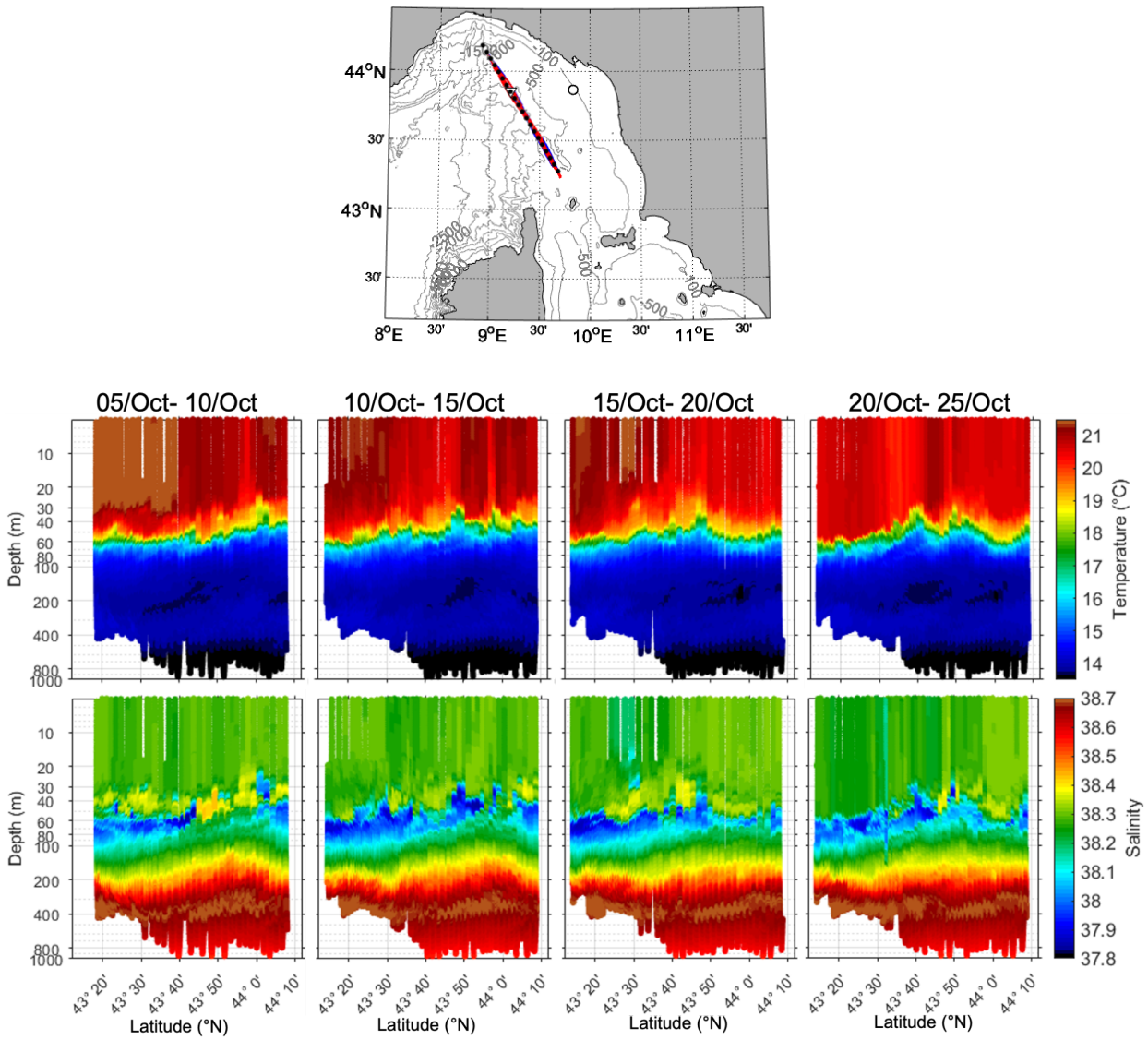

Figure 3.2-4: Top panel: Jason-3 satellite track number 44 (black dots) and glider trajectory (blue and red lines); temperature (middle panels) and salinity (bottom panels) profiles acquired by glider Maria along the satellite track. The date of data collection is indicated at the top of each transect.

Along the Jason-3 track (Figure 3.2-4), the gliders observed a sea surface salinity of about 38.3 and a temperature between 20 and 21.5°C. At depths of 50 to 80 m, the MAW are characterised by lower salinity values (37.8-38.1). The saltier and warmer MLIW (salinity 38.6-38.7; temperature 13.8-14°C) are found at depths of 300 to 500 m, and below 500 m depth the WMDW are characterised by a temperature between 13.3 and 13.8°C and a salinity between 38.5 and 38.65. Overall, the southern part (<43° 40'N) of the glider transect along the Jason-3 satellite track (Figure 3.2-6) is characterised by warmer water masses compared to the north throughout

the LOGMEC17 experiment. The latitude where we can see this change in water temperature is where part of the WCC rotates clockwise (warmer water mass) and part forms the LPCC (colder), as shown by the geostrophic velocity maps (Figure 3.2-1). Moreover, the MAW tends to be trapped in a thinner layer around 50 m depth as it moves northward.

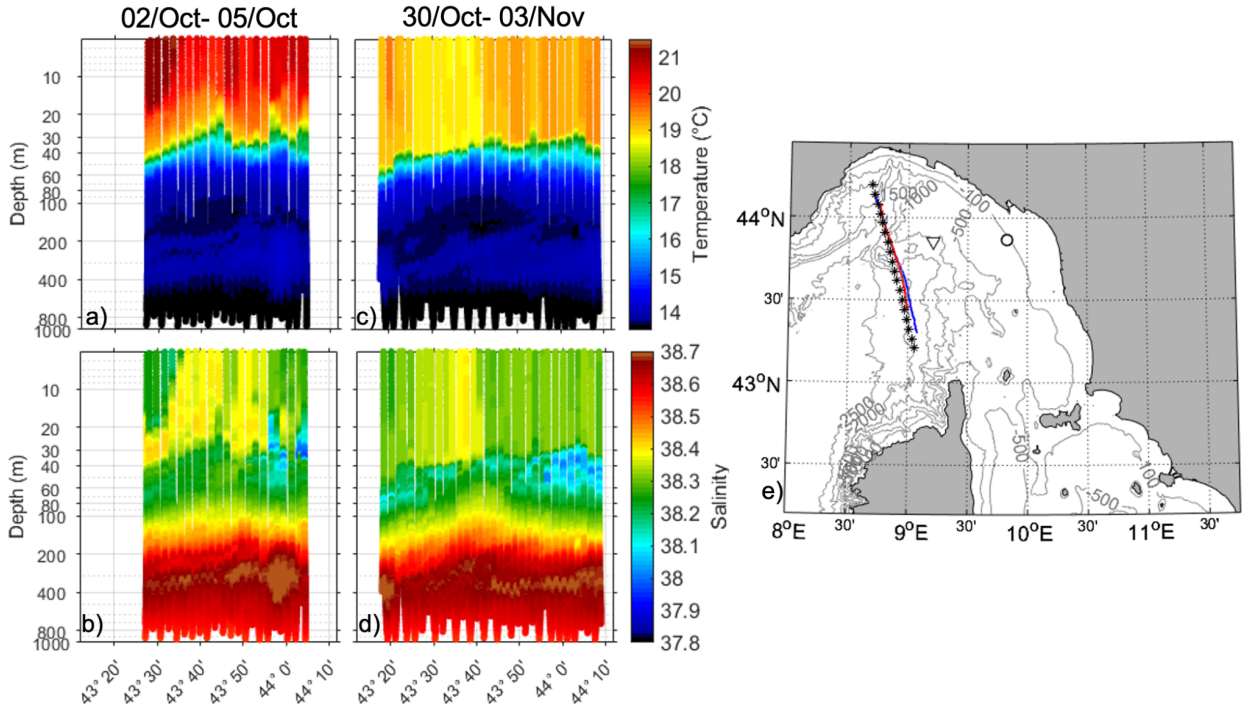

Figure 3.2-5: Temperature (a,c) and salinity (b,d) profiles collected by gliders along Sentinel-3A satellite track number 44. The date of data collection is indicated at the top of each transect. (e) Map of the Ligurian Sea showing bathymetry (thin grey lines), glider trajectories (blue and red lines), and Sentinel-3 satellite track number 44 (black asterisks).

Glider profiles collected along track 44 of Sentinel-3A (Figure 3.2-5a,b) show that MAW is observed from 02 to 05 October only around 44°N, the same latitude where a warmer and saltier MLIW core is clearly visible between 200 and 400 m depth, possibly transported by the LPCC running perpendicular to the northern part of the transect (Figure 3.2-1b). This suggests that in the inner part of the cyclonic gyre, the MAW is not present and the MLIW is trapped in a thinner layer. In addition, the water mass within the cyclonic eddy from the surface to a depth of 30 m is saltier than in the surrounding area.

The same satellite track was followed by glider Maria almost a month later, from 30 October to 03 November (Figure 3.2-5c,d). During this period, the LPCC flows parallel to the track (Figure 3.2-1e), and the MAW is present, although slightly saltier (~38.1). Sea surface salinity is similar to the previous month, while sea surface temperature decreases significantly and is 18.5-19°C.

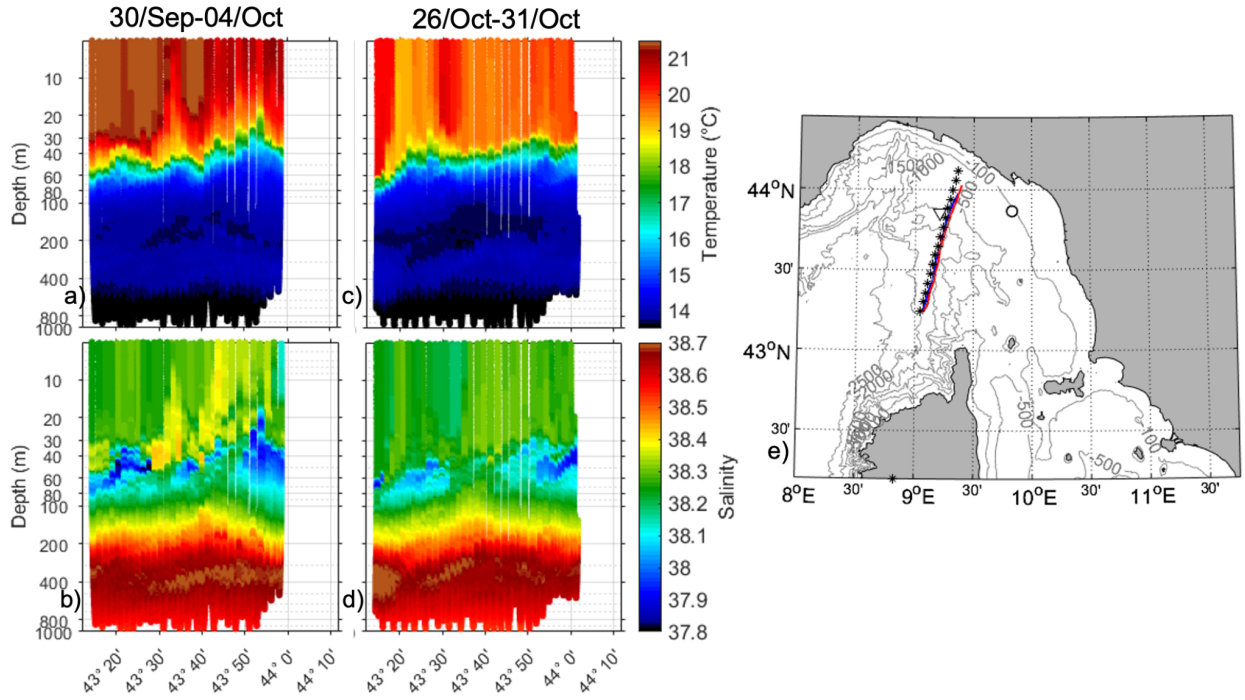

Figure 3.2-6: Temperature (a,c) and salinity (b,d) profiles acquired by glider Maria along Sentinel-3A satellite track number 85. The date of data collection is indicated at the top of each transect. (e) Map of the Ligurian Sea showing bathymetry (thin grey lines), glider trajectories (red line), and Sentinel-3 satellite track number 85 (black asterisks).

The last track is number 85 of Sentinel-3A, which was followed by the glider Maria from September 30 to October 4 (Figure 3.2-6). It confirms that the southern area is characterised by warmer water masses and that in the central part, at the cyclone boundary (Figure 3.2-1b), the MAW is not clearly visible, while in the northern part, near the coast, the MAW extends from 30 to 80 m depth. Similar water masses were observed from Dora-jr from 26 to 31 October, with a MLIW core occurring in the southern part of the transect, probably transported perpendicular to the transect by the strong WCC (Figure 3.2-1e). During this period, sea surface temperatures range from 19.5 to 20°C.

3.3 Mesoscale and sub-mesoscale characterization

Mesoscale and submesoscale samples were collected from two research vessels and several groups of drifters deployed close to the near-coastal mooring (Table 3.3.1-1). Regular CTD casts at 2.5 km spacing conducted by RV Aretusa covered a 15 km square area, referred to as the LS2500 sampling (see Section 2.1 for details). ScanFish data were collected close to the near-coastal mooring along a variety of pathways (Figure 2.1-6) within the CTD sampling area. The sampling strategy assumed two days as the synoptic time scale.

To investigate the variability of temperature and salinity in the experimental area, objective analysis was applied to the CTD and ScanFish data. Depending on the sampling strategy, different parameters are used to perform the objective analysis (Table 3.3-2). The analysis is performed for the entire water column and for the different sampling dates, but in the following we focus on the period from 27 to 29 September, since this is the only period when several platforms (CTD, ScanFish, mooring, and drifter) collected data simultaneously, and only the temperature and salinity field at 40 m depth is presented, since the preliminary analysis showed that this depth is characterised by the highest variability. The analysis is not affected by MLD variability because the MLD at the near-coastal mooring, located within the sampling area, is at about 20 m depth during the selected period (Figure 3.4-5).

Platforms	**Sampling date**
CTD RV Aretusa	27-29/Sep
ScanFish	26-29/Sep; 1-2/Oct; 24/Oct; 26/Oct
Near-coastal mooring	27/Sep–25/Oct
Drifters	26/Sep; 02/Oct

Table 3.3-1: Sampling period for CTD casts, ScanFish, near-coastal mooring, and drifter deployments.

	A (km)	B (km)	E (%)	LIMIT	NPTINF	R_{inf} (km)
SM500	2	1	40	10	10	5
LS2500	6	4	40	20	30	20

Table 3.3-2: Objective analysis parameters for each sampling. A indicates the zero crossing, correlation scale, B the decay length scale, E the expected initial error of the observations, LIMIT the number of influential points to be considered for each interpolation (NPTINF is its maximum value), R_{inf} the influential radius within which the observations are selected.

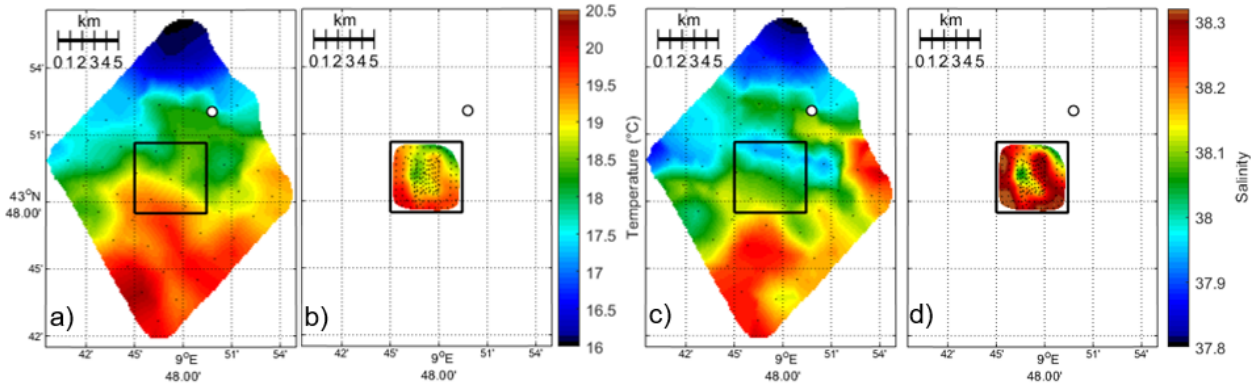

Figure 3.3-1: Temperature (a,b) and salinity (c,d) at 40 m depth measured with CTDs (a,c) from 27/Sep 21:30 to 29/Sep 14:30 and with ScanFish (b,d) from 28/Sep 09:00 to 29/Sep 16:00. The black square shows the ScanFish operating area and the white dot the near-coastal mooring. The black dots indicate the location of the data used for the objective analysis.

Both the temperature and salinity fields derived from CTD casts at 40 m depth (Figure 3.3-1a,c) show a gradient along the north-south direction of 4°C and 0.55, respectively. The northern area is characterised by colder and fresher water with a temperature of 16°C and salinity of 37.8, while in the south the temperature reaches 20.4°C and salinity 38.25.

The data collected by ScanFish (Figure 3.3-1 b,d), centred on the CTD sampling area, show features with smaller dimensions (order of 1 km). Indeed, in the central area, a structure with a temperature of 18.5°C and a salinity of 38.05 is surrounded by warmer and saltier water. The salinity field from ScanFish clearly shows a difference in salinity with respect to CTD sampling that needs further investigation.

To better study the scales of observed structures during LOGMEC17, an objective analysis was performed for all ScanFish sampling periods, but only the most important results are reported here.

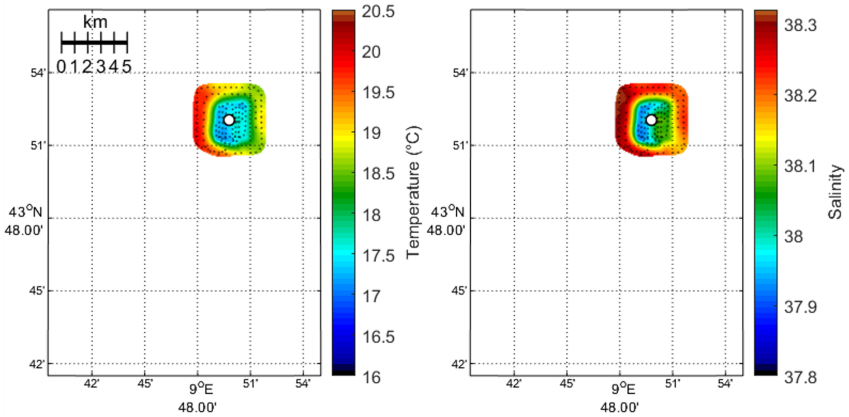

Figure 3.3-2: Temperature (left) and salinity (right) at 40 m depth collected by ScanFish on 01 and 02 October. The white dot indicates the near-coastal mooring and the black dots the location of the data used for the objective analysis.

The objective analysis of the temperature and salinity field collected on 01 and 02 October (Figure 3.3-2) confirms that submesoscale structures are clearly visible. Similar structures are also found at different depths and during different sampling periods, indicating high variability extending to the sub-mesoscale in this region.

From now on, we will focus on the data collected on 28 and 29 September because the ScanFish (Figure 3.3-1d) measured a saltier (~0.2) water mass than that measured by the CTD (Figure 3.3-1c), and we will investigate this by comparing data collected simultaneously from different platforms. To distinguish between temporal and spatial variability and possible different calibration of the various sensors used, a comparison of observations collected simultaneously from ScanFish, CTDs, and near-coastal mooring was performed. We focus on 28 September as the three platforms collected data simultaneously and they were close to each other (Figure 3.3-3a).

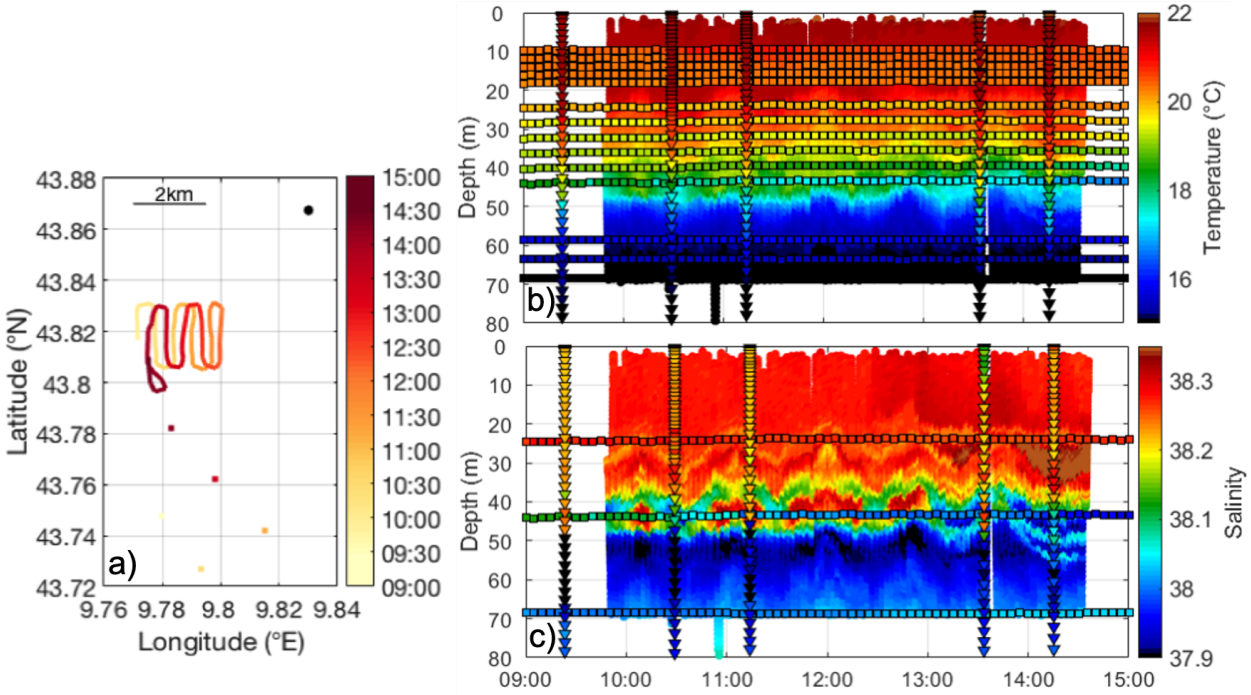

Figure 3.3-3: ScanFish path with colour coding by time, CTD casts (coloured dots) and near-coastal mooring (black dot) (a); temperature (b) and salinity (c) time series of ScanFish, CTDs (triangles), and mooring (square).

Overall, the lowest temperature values (Figure 3.3-3b) were measured at the near-coastal mooring north of the ScanFish sampling area, confirming the presence of cold water masses in the northern area, which were also detected by the objective analysis of the CTD casts (Figure 3.3-1). The water mass at the near-coastal mooring at about 45 m depth is fresher than that observed by ScanFish and the CTD casts, while the water mass at about 25 m depth is saltier than that sampled by the CTDs. ScanFish observed a saltwater tongue between 35 and 50 m

depth. Temperature and salinity values measured by ScanFish fluctuate almost once per hour. The differences in salinity and temperature values measured by the different platforms are clearly visible, so we investigate them further, distinguishing between temporal and spatial variability. Since ScanFish and the mooring are only 5 km apart, to distinguish between temporal and spatial variability, the temperature time series measured by these two platforms is analysed where the highest variability occurs (40 m depth) (Figure 3.3-4).

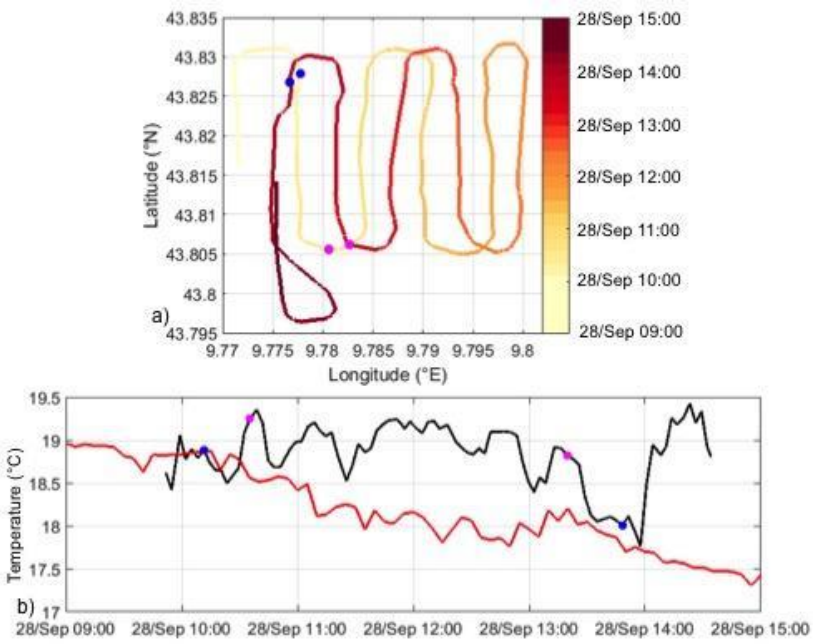

Figure 3.3-4: (a) ScanFish path colour-coded with time; (b) temperature time series measured by ScanFish (black line) and by near-coastal mooring (red line) at 40 m depth . Blue and magenta dots indicate temperature observed by ScanFish at locations marked with the same colour in panel (a).

In the northwestern part of the ScanFish area (blue dots), the temperature decrease of 1°C in 3.5 hours is measured by both ScanFish and the mooring 7 km away, so it is clearly a temporal variation of the temperature field. Although the trend of temperature decrease was observed from both platforms, the amplitudes of the high-frequency oscillations are higher in the ScanFish data than at the mooring, suggesting that this is due only to the spatial variability recorded by ScanFish. The spatial variability explains the fluctuations shown in Figure 3.3-3b,c. The distance between the northern and southern boundaries of the Scanfish sampling area is 5 km. Despite the short distance, the southern area (magenta dots) is characterised by a warmer water mass than the northern area (blue dots). This could indicate microscale variability or the presence of a front in the centre of the ScanFish sampling area.

The presence of a front is also suggested by the temperature gradient along the north-south direction observed by the CTD (Figure 3.3-1). To better investigate this feature, the direction of

the frontal shift is examined below, beginning with analysis of the near-coastal mooring ADCP and the shipboard ADCP turned on during the ScanFish survey on September 28.

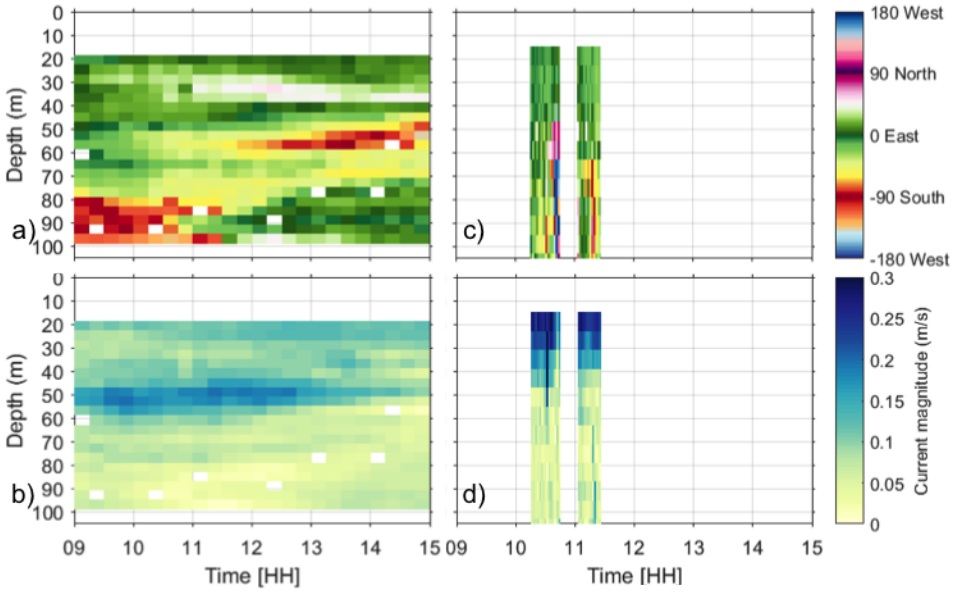

Figure 3.3-5: Direction and magnitude of the current measured by the near-coastal mooring ADCP (a and b, respectively) and by the ADCP on NRV Leonardo (c and d, respectively) on 28 September from 9:00 to 15:00.

At near-coastal mooring, the current direction (Figure 3.3-5a) is E- NE, which is consistent with the ADCP onboard the vessel in the ScanFish survey area (Figure 3.3-5c), down to a depth of 40 m, while below 40 m it becomes SE. The velocity in the surface layers is about 0.15 m/s at the mooring (Figure 3.3-5b) and is stronger, reaching 0.3 m/s, in the ScanFish area (Figure 3.3-5d). A maximum value of 0.2 m/s occurs at the mooring between 40 and 60 m depth, while the current velocity in the ScanFish area below 40 m depth is less than 0.1 m/s.

On 28 September, another available current measurement was provided by drifters deployed two days earlier (Figure 3.3-6). The drifters indicate that the surface current is southeastward (Figure 3.3-6a), and the drifter near the ScanFish survey area measures a current velocity of 0.3 m/s (Figure 3.3-6b), which is consistent with the current measured by the onboard ADCP (Figure 3.3-5d). Moreover, the satellite data (not shown) indicate a southward geostrophic current in the studied area.
The combination of all the data available on 28 September shows that the front is moving in a southeasterly direction.

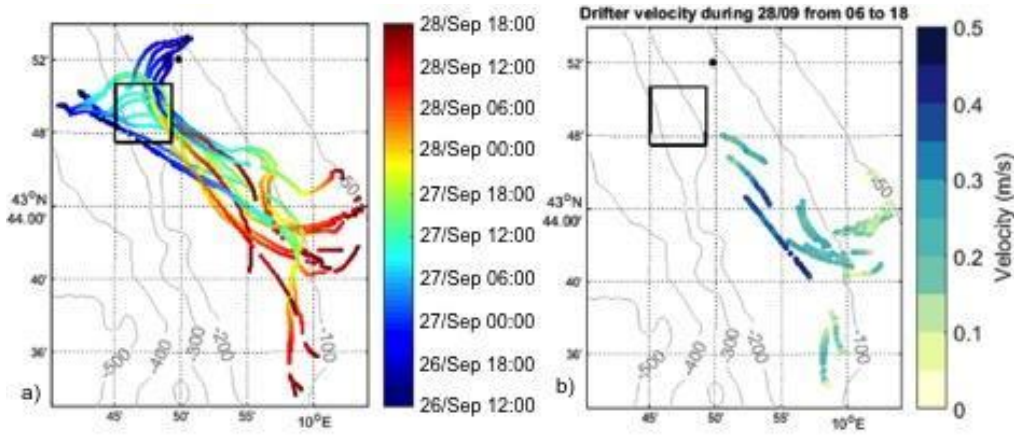

Figure 3.3-6: Drifter trajectories colour-coded with time (a) and drifter locations colour-coded with velocity during 28 September (b). The black square denotes the ScanFish sampling area and the black dot denotes the near-coastal mooring location.

3.4 Observed variability

The large-scale variability of the LOGMEC17 area is characterised using gridded satellite-based sea level data and derived geostrophic current provided by CMEMS (Pujol et al., 2016).

The ADT and geostrophic velocities averaged during the two months of the LOGMEC17 experiment (14 September - 14 November) (Figure 3.4-1a) show the presence of the WCC splitting north of Corsica island to form the LPCC and turning partially clockwise north of Capraia island, while the ECC cannot be clearly identified. The deep mooring is strongly influenced by the LPCC and a strong cyclone (mean ADT of -12cm) is located in the northwestern area.

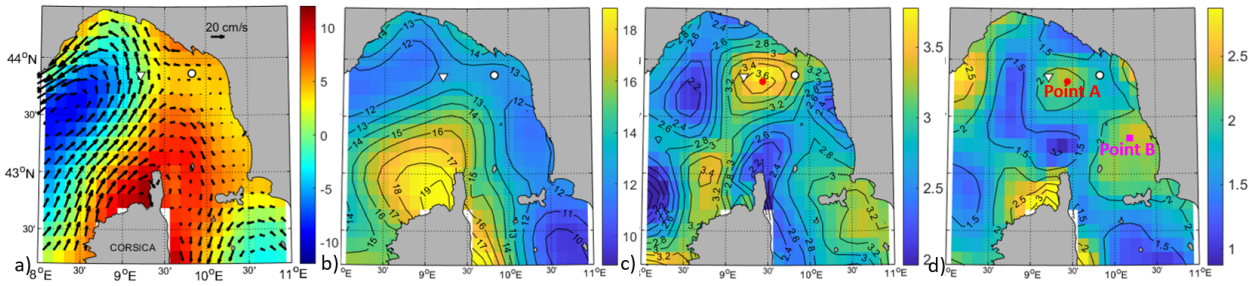

Figure 3.4-1: (a) Averaged ADT and (b) averaged SLA in cm from 14 September to 14 November, 2017, (c) corresponding SLA standard deviation in cm, and (d) SLA standard deviation map computed removing the daily basin mean.

The averaged Sea Level Anomaly (SLA) ranges from 9 cm to 18 cm near the island of Corsica. The corresponding standard deviation map SLA (Figure 3.4-1c) shows an area near the two moorings with high SLA variability (3.5 cm) compared to the surrounding area with much lower variability, indicating that the LPCC changes position between the two moorings. The strongest variability is found at point A. To distinguish the basin and intra-basin variability, the daily basin averages SLA have been removed before computing the standard deviation (Figure 3.4-1d). This method highlights another area with a high value of standard deviation (2.4 cm) located off Livorno (point B, 43.4°N 10.2°E).

Point A is located near the deep mooring, is about 45 km from the coast, is under the influence of the LPCC, and the bathymetry is about 1000 m. Point B is about 15 km from the coast and is near the 100 m bathymetric line.

The variability of the SLA time series in the two highlighted regions, point A and B, and over the entire Ligurian Basin during the LOGMEC17 campaign are shown in Figure 3.4-2a, while Figure 3.4-2b shows the SLA anomalies of the two points with respect to the Ligurian Basin.

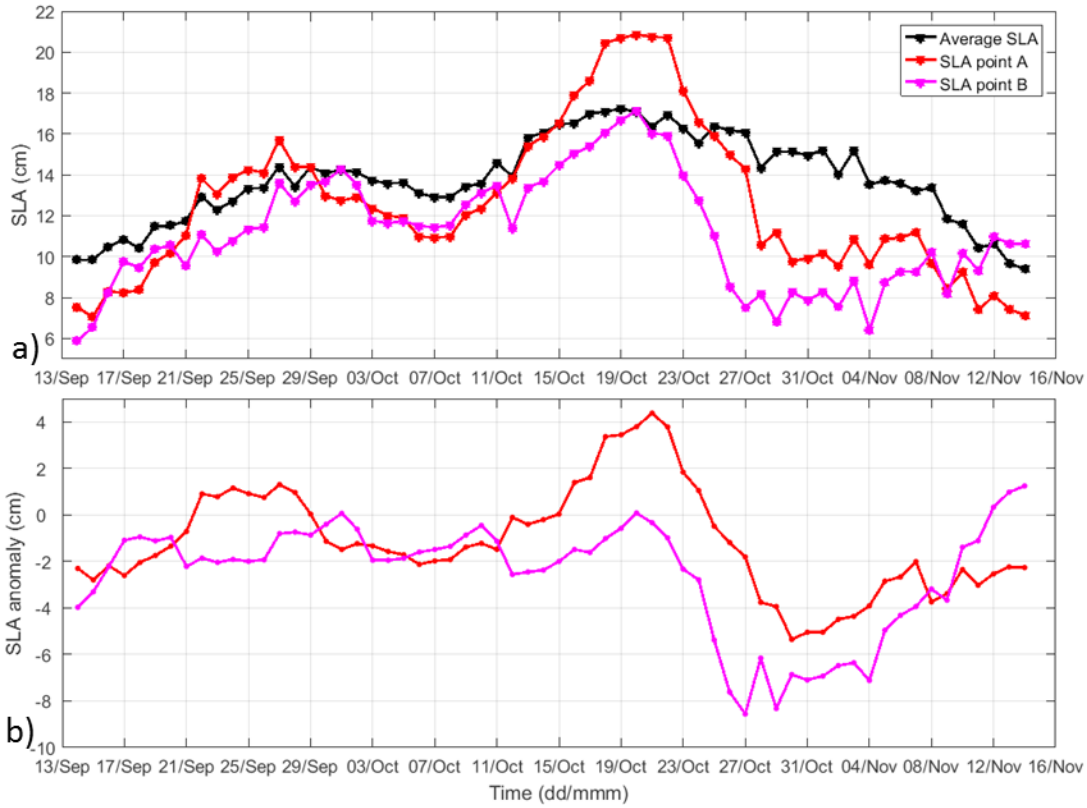

Figure 3.4-2: (a) Time series of SLA over points A and B (red and magenta lines, respectively) and average SLA (black line) of the whole Ligurian basin. b) Time series of the difference between points A (red) and B (magenta) SLA and average SLA over the whole area (anomalies).

The SLA time series (Figure 3.4-2a) for the Ligurian Basin has two relative maxima, one around 29 September (14 cm) and the other around 19 October (17 cm). The SLA at point A largely follows the Ligurian Basin oscillation in the first part of the time series, but amplified, reaching 21 cm on 20 October, while at point B there are smaller variations. Within a week, after 20 October, SLA decreases by almost 10 cm at both points.

To extrapolate the dominant frequencies of the anomalies, the discrete Fourier transform is applied to the SLA (Figure 3.4-3), and the principal power peaks are listed in Table 3.4-1.

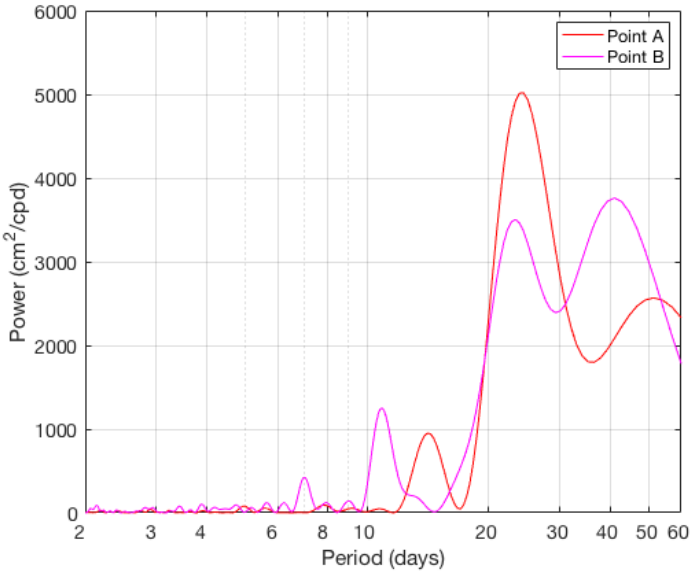

Figure 3.4-3: Power spectra of the time series of SLA anomalies for points A (red line) and B (magenta line). A logarithmic scale on the X axis is used. The position of points A and B are marked in Figure 3.4-1.

	Point A	Point B
Period (days)	Power (cm^2/cpd) $\cdot 10^3$	Power (cm^2/cpd) $\cdot 10^3$
51.2	2.57	2.83
41.0	2.08	3.76
23.8	5.01	3.47
14.2	0.95	0.04
10.9	0.04	1.25
7.0	0.002	0.42

Table 3.4-1: Periods and power peaks for Point A and B.

For periods longer than 20 days, the power in points A and B is high. As expected from the time series in point B, the high power is associated with the period of 10.9 days, which probably explains the small fluctuations highlighted in Figure 3.4-2b. In point A, the power decreases sharply for periods less than 14 days. Conversely, Point B exhibits high energy, i.e., high variability, at 7 and 10.9 days. According to the spectral analysis, the predominant frequencies at point A are 51.2, 23.8 and 14.2 days, while at point B they are 41, 23, 10.9 and 7 days (see Table 3.4-1 for the corresponding power values).

Considering the length of the time series of 60 days, the significance of the discrete Fourier transform results is low for periods close to the length of the time series. To be confident on the dominant slow processes, spectral analysis was performed for one-year SLA at points A and B.

In particular, wavelet analysis (Figure 3.4-4) confirms that the dynamics are very energetic with 20- and 30-day periods during the LOGMEC17 period.

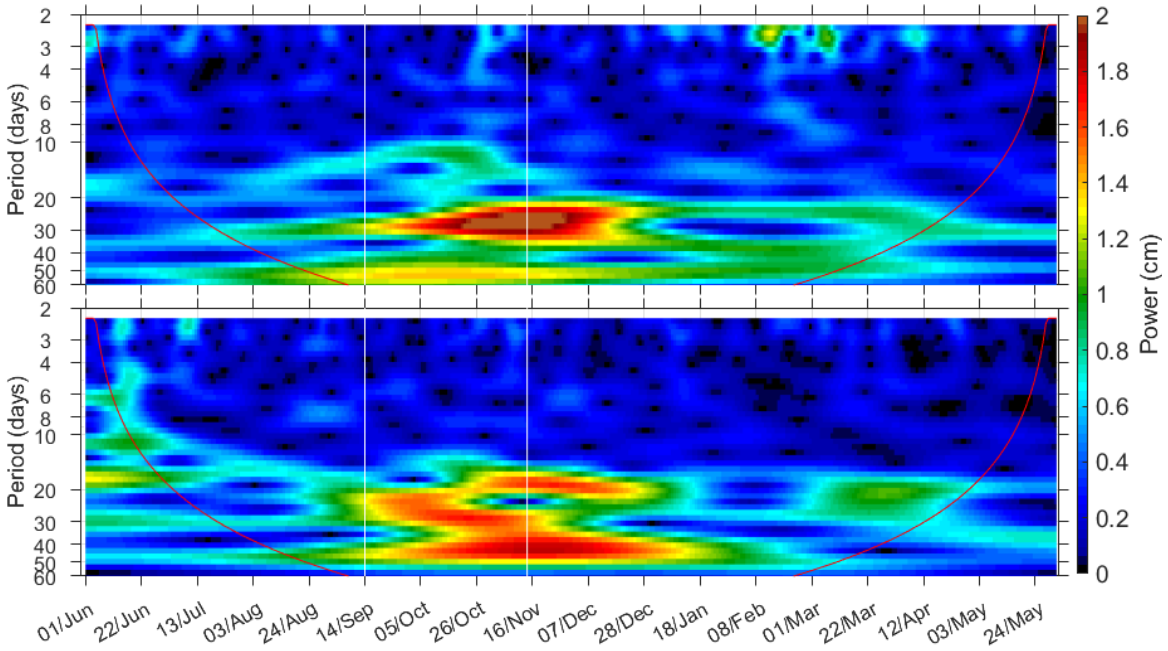

Figure 3.4-4: Wavelet of the SLA at point B (top) and A (bottom) for 1 year. The two vertical white lines denote the period of the LOGMEC17 experiment. The red line denotes the cone of influence.

In particular, the wavelet (Figure 3.4-4) shows that the processes with periods longer than 10 days during the LOGMEC17 experiment are much more energetic compared to the other months of the year.

To complement the satellite data used to analyse low-frequency variability during the LOGMEC17 experiment, we will now focus on the high-frequency data collected in the experimental area, which will allow us to resolve higher frequencies. In particular, we will investigate the Mixed Layer Depth (MLD), its variability, and the temperature variability at the two fixed moorings during LOGMEC17. A suitable data set for calculating the MLD and investigating its variability during LOGMEC17 was collected only from the near-coastal mooring, because in the deep mooring the near-surface temperature sensor was located at 30 m depth, i.e., below the MLD.

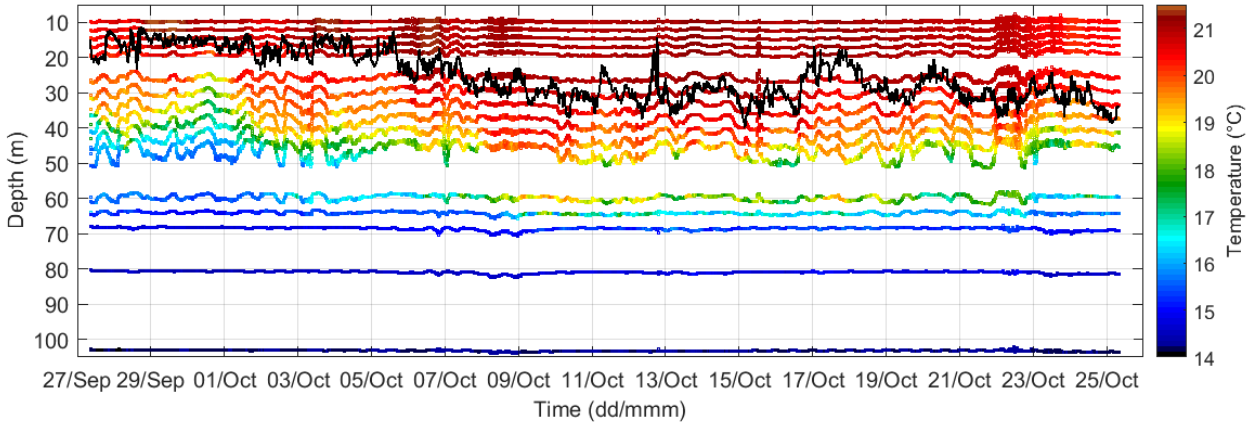

Figure 3.4-5: The black line indicates the estimated MLD. The colour-coded scale shows the temperature values measured by operating sensors.

The estimated MLD time series (Figure 3.4-5), derived from the near-coastal mooring and averaged over the month of data collection, is 25 m and ranges from 12 to 40 m depth, consistent with the literature (see 1.2 Ligurian Sea Background). At the beginning of the time series, from 27 September to 05 October, the mixed layer depth is shallow, between 15 and 20 m, then it becomes deeper, reaching 40 m on 15 October.

Similar to the analysis of satellite data, spectral analysis is applied to the MLD. Most of the MLD variability is explained by processes that occur with a period of about 20 days (Figure 3.4-6) and have a power of about $8{\cdot}10^{5}\frac{m^{2}}{cpd}$. This is consistent with the analysis of the satellite data, since for a period of about 20 days the power is high at the two selected points. Other relevant peaks ($\sim 10^{5}\frac{m^{2}}{cpd}$) are observed at 6, between 2.8 and 3.5 days and at 1.5 days. A smaller contribution with a power of about $0.5{\cdot}10^{5}\frac{m^{2}}{cpd}$, is associated with a period of 4.7 days.

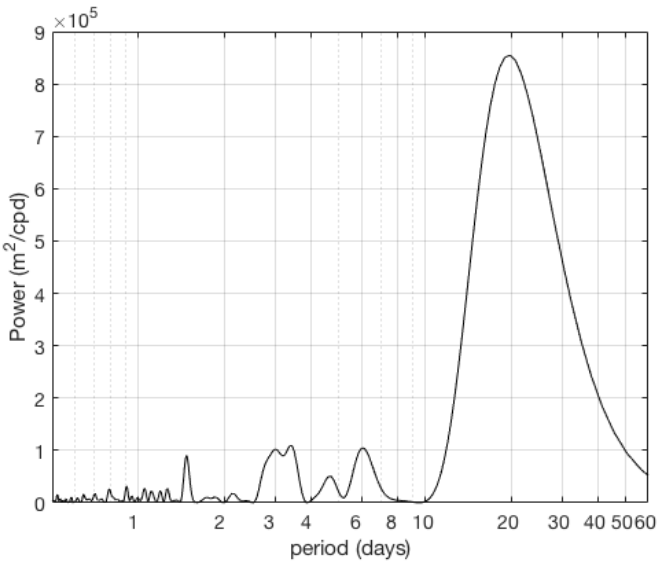

Figure 3.4-6: Power spectra of Mixed Layer Depth at the near-coastal mooring. A logarithmic scale is used for the x-axis.

Higher frequencies are investigated by applying the wavelet transform to the temperature time series at selected depths. In particular, the wavelet transform is applied at depths of 40 and 60 m because preliminary analysis showed strong variability at these depths and most of the temperature variation is found at these depths, as confirmed by the mean vertical profiles and standard deviation at the two moorings (Figure 3.4-7). Figure 3.4-7 also shows that the deep mooring measures colder water masses than the near-coastal mooring.

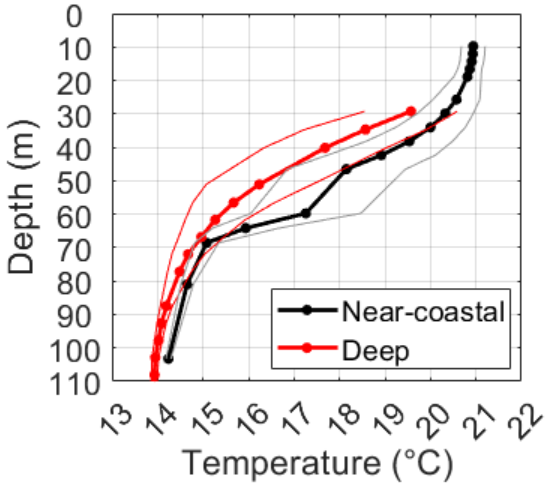

Figure 3.4-7: Mean (thick lines) and standard deviation (thin lines) of temperature measured by near-coastal (black) and deep mooring (red) from 27 September to 25 October. The dots represent the depth of the temperature sensors.

Here, we define slow and fast processes assuming a threshold of 2 days, since the sea trial was designed assuming a synoptic time scale of 2 days and the CTD sampling is indeed completed in almost 2 days (see Section 2.1).

Applying the wavelet to the temperature time series at the two moorings allows us to identify the periods of fast dynamics that contribute most to the temperature variability during LOGMEC17.

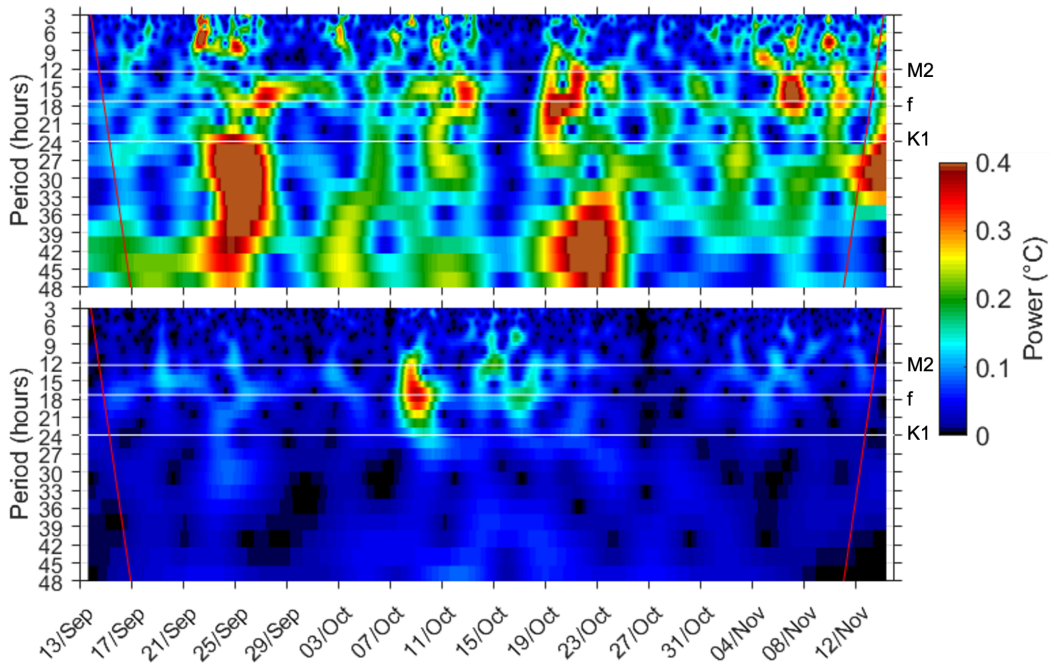

Figure 3.4-8: Wavelet of temperature measured by the deep mooring at 40 m (top) and 60 m depth (bottom) for high-frequency processes (period from 0 to 48 hours). The horizontal white lines indicate the inertial period (f) and the diurnal (K1) and semidiurnal (M2) tidal periods. Solid red lines represent the cone of influence.

At the deep mooring (Figure 3.4-8), the temperature variability at 40 m depth is due to several fast processes, as energy is spread within the considered frequency window (3 to 48 hours), however, some peaks are evident. The strongest, centred between 24 and 42 hours, occurs from 23 to 27 September. Processes near the inertial frequency occur throughout the two months of data collection, and peaks appear around 27 September, 13 October, from 19 to 22 October, and on 07 November. At 60 m depth, power is weaker due to smaller temperature variations, but maxima between 12 and 24 hours are present; the strongest power peak occurs on 09 October close to the inertial period.

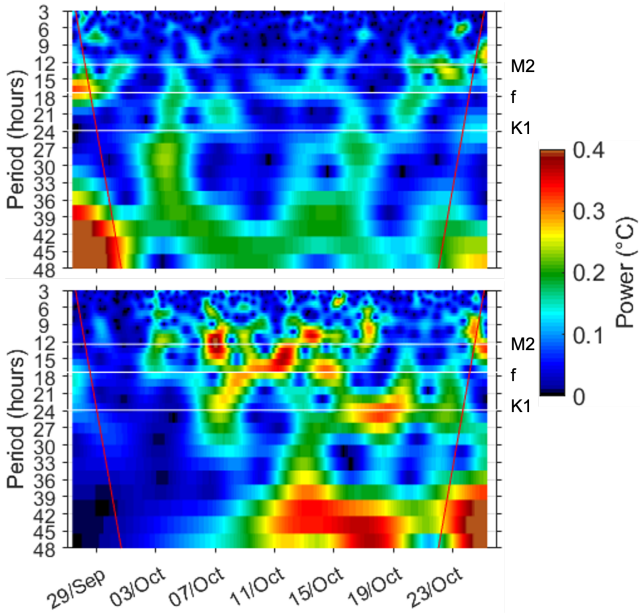

Figure 3.4-9: Same as Figure 3.4-8, but for the near-coastal mooring (from 27 September to 25 October).

At the near-coastal mooring (Figure 3.4-9), overall temperature variability is weaker than at the deep mooring (Figure 3.4-8). At 40 m depth, power is fairly evenly distributed over periods shorter than 48 hours, while peaks in power are observed at 60 m depth. From 06 to 20 October, the strongest energy is confined to periods of 12 to 24 hours. In addition, a significant amount of energy (0.35 °C) is observed between 36 and 48 hours from 11 October. Temperature variability at 60 m depth is strongly influenced by processes that occur at near- inertial periods from 07 to 15 October.

4. Observed Near-inertial internal waves in the Northwestern Mediterranean Sea

This chapter is a manuscript to be submitted to a scientific journal for publication.

Abstract

Near-Inertial internal Waves (NIWs) are found to be the dominant high-frequency process during a multi-platform campaign conducted in the Ligurian Sea (Northwestern Mediterranean Sea) from September to November 2017. A buoy moored at 1000 m depth observes strong NIWs along the sampled water column from 30 to 250 m depth (deeper available observation), while a near-coastal mooring, fixed along the 100 m bathymetric line, detects NIWs only from 55 to 63 m depth. The near-surface NIWs are generated locally by wind gusts, while the deeper NIWs are generated in remote regions and arrive at the mooring. On average, NIW energy propagates downward from the subsurface (30 m depth) into the ocean interior, following two identified bands with mean vertical group velocities of $2.6 \cdot 10^{-4}$ and $1.9 \cdot 10^{-4}$ m s^{-1}, respectively, although considerable variability in group velocities is observed throughout the water column. The energy of the NIWs near the surface propagates faster in both vertical and horizontal directions than at greater depths. Only one NIW energy envelope is characterised by an upward energy propagation (downward phase) along the isopycnals. Most of the observed NIW frequencies are blue-shifted, reaching a value 9% higher than the local inertial frequency, but two events are characterised by a red-shift (up to 3%). We argue that the NIW frequency shift is caused by the wave interaction with the local eddy field. The NIW current amplitude does not decrease with depth, and its mean value is 0.13 m s^{-1}. The estimated mean horizontal and vertical wavelengths of downward propagating NIWs at the deep mooring are 43±25 km and 125±35m, respectively, while they are shorter at the near-coastal mooring, 36±2km and 33±2m, respectively.

4.1 Introduction

Near-Inertial internal Waves (NIWs) are waves in the interior of the ocean with a frequency close to the inertial frequency. NIWs are intermittent (Fu, 1981), highly energetic and cause strong vertical shear currents (Ferrari and Wunsch 2009). For this reason, NIW contribute significantly to vertical mixing (Alford *et al*., 2003) in shallow water (Hebert and Moum 1994; Alford and Gregg 2001), and studies suggest that they are also responsible for mixing in the deep ocean (Silverthorne and Toole 2009). Global studies show that the NIWs deepen the ocean mixed layer depth by up to 30%, influence climate (Jochum *et al*., 2013), and affect a variety of processes as they transport energy at different scales. Because NIW play a key role in the energy balance of ocean circulation, understanding these waves can lead to significant improvements in numerical ocean models and their products.

NIWs are mostly generated by winds (Alford *et al*., 2016), which is confirmed by observations and modelling exercises. Impulsive wind stresses generate near-inertial oscillations in the surface mixed layer and the convergences and divergences of these oscillations deepen and raise the base of the mixed layer and transfer energy to downward propagating NIWs (Gill 1984; D'Asaro 1985; Alford *et al*. 2016). Other mechanisms may also be responsible for the generation of NIWs, such as the formation of lee waves over bottom topography by geostrophic flow (Nikurashin and Ferrari 2010) and geostrophic adjustment at fronts and eddies (Alford et al., 2013; Nagai and Hibiya 2015), but the relative importance of these mechanisms is not known.

NIWs can propagate far from their regions of generation before breaking (Ray & Mitchum 1996, Alford 2003, Zhao & Alford 2009) and they interact with other processes that alter their properties, making NIWs characterization challenging (Alford *et al*., 2016).

The NIWs phase propagates mainly upward (Sanford 1975), with some exceptions (Alford *et al*., 2016). The upward phase velocity indicates a downward group velocity, indicating downward energy propagation (Leaman and Sanford 1975, D'Asaro and Perkins 1984).

The horizontal scale of NIW ranges from a few tens to hundreds of kilometres, while the vertical wavelength is three orders of magnitude smaller (Kundu 1976, Kawaguchi *et al.*, 2020, Lelong *et al.*, 2020)

Several studies show that the NIWs interaction with mesoscale structures is responsible for the frequency shift of NIW with respect to the local inertial frequency (Kunze 1985, Poulain 1992, Rainville and Pinkel 2004, Young and Jelloul 1997, Asselin and Young 2020). Anticyclones (cyclones) cause a frequency shift to lower (higher) frequencies than the local inertial frequency, which is called a red shift (blue shift). The frequency shift could also be caused by the interaction of NIW with strong internal tides and fronts (Thomas *et al.*, 2017).

The study of NIW is difficult and expensive because it requires synoptic sampling at very high resolution. In the present work, we used the dataset collected during the LOng-term Glider

Missions for Environmental Characterization (LOGMEC17) campaign in the Ligurian Sea (northwestern Mediterranean) in autumn 2017. The Ligurian Sea plays a crucial role in the Mediterranean circulation as it is the region where the confluence of two currents flowing along the Corsica sides, namely the Western Corsican Current (WCC) and the Eastern Corsican Current (ECC) (Astraldi and Gasparini, 1992), form the Liguro-Provencal-Catalan Current (LPCC) (Figure 1). In winter, the LPCC is stronger and mesoscale activity is more intense than in summer (Birol *et al*., 2010). In particular, the time scale of mesoscale activity from late fall to winter is 3-6 days, while in summer it is 10-20 days (Taupier-Letage and Millot, 1986, Sammari *et al*., 1995; Echevin *et al.*, 2003). The meandering nature of the LPCC has long been studied (Crépon *et al*., 1982, Flexas *et al*., 2005), and recently some studies have focused on the eddy activity north of Corsica (Casella *et al*., 2014, Borrione *et al*., 2016). Regarding the known eddies in the studied area, the western Liguro-Provencal basin is characterised by a large permanent cyclonic eddy called the Gulf of Lion Gyre (GLG) (Madec *et al*., 1991; Pinardi *et al*., 2015). Moreover, an anticyclone has been observed around the island of Capraia during oceanographic campaigns (Poulain *et al*., 2012).

In most of the Mediterranean Sea, the inertial currents have amplitudes of $O(10^{-1}$ m $s^{-1})$, while the tidal currents have amplitudes of $O(10^{-3}$ m $s^{-1})$ (Alberola *et al*., 1995; Tsimplis *et al*., 1995). Especially in the Ligurian Sea, the inertial period (17.3 hours) is easily distinguished from the diurnal and semidiurnal tidal periods. In the northwestern Mediterranean Sea, NIW were observed by Millot and Crèpon (1981), Van Haren and Millot (2004), and by Picco *et al.* (2010), showing that they are the main components of the regional internal wave spectrum. In this region, Small *et al.* (2012) performed numerical simulations to demonstrate the importance of NIW in inducing mixing and cooling of the SST.

Perkins (1972) observed inertial oscillations in the Mediterranean Sea throughout the water column at a frequency nearly 3% higher than the local inertial frequency on a single mooring equipped with current metres located at 500m depth intervals between 200 and 2200 m, but the very sparse vertical sampling did not allow identification of NIWs.

In the northwestern Mediterranean Sea, NIWs were observed by Millot and Crèpon (1981), Van Haren and Millot (2003), and by Picco *et al.* (2010), highlighting that they are the main components of the regional internal wave spectrum. Numerical simulations (Small *et al.,* 2012) show the importance of NIW shear-induced mixing and cooling of the SST in this region.

There is no complete characterization of the NIWs in terms of wavelengths, phase, and group velocity in the Mediterranean Sea. In the eastern Mediterranean the wavelengths of the NIWs have been estimated to be 10 to 100 km and 100 to 150 m in horizontal and vertical directions, respectively (Cuypers *et al*., 2012). Motivated by the observations of these strong NIWs, a numerical study (Lelong *et al*., 2020) was conducted to investigate the interaction of NIWs with the semipermanent anticyclonic Cyprus Eddy, in the southeastern Levantine Sea.

The present study identifies for the first time the NIWs and their characteristics in the Ligurian Sea. It describes their structure and vertical propagation and investigates the potential causes of their frequency shift..

The paper is organised as follows. Section 2 describes the LOGMEC17 campaign and the data set used to identify and characterise the NIWs. The regional setting, the identification of NIWs, and their characteristics are analysed in Section 3. Section 4 discusses the results and draws conclusions.

4.2 Data and Methods

The LOGMEC17 experiment

The LOng-term Glider Missions for Environmental Characterization 2017 (LOGMEC17) is a multi-platform, multi-scale, multi-disciplinary combined acoustic and oceanographic campaign led by the NATO-STO Centre for Maritime Research and Experimentation (Figure 1).

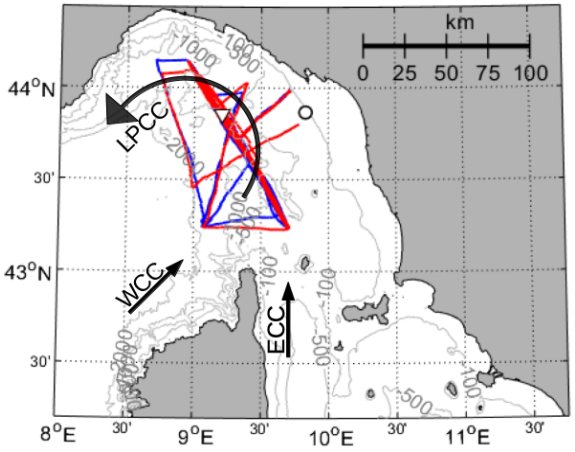

Figure 1: Map of the Ligurian Sea showing bathymetry (grey thin lines), main currents (black arrows), and locations of the deep mooring (triangle) and near-coastal mooring (dot). The trajectories of the two deep-sea gliders are indicated by the red and blue lines.

The sea trial took place from 13 September to 14 November 2017 in the Ligurian Sea and investigated the variability and predictability of the Ligurian Sea properties at different scales. To complement the available satellite data, the large scale was sampled by two oceanographic deep gliders. During the same period, two oceanographic moorings equipped with several multidisciplinary sensors provided high-frequency observations at fixed points. During a one-week period, the mesoscale and submesoscale were sampled by three research vessels.

In the vicinity of the near-coastal mooring, the mesoscale was sampled by several CTD casts conducted at regular intervals. During the CTD sampling, another research vessel collected the submesoscale data using a towed, undulating vehicle system called Scan-Fish, which was equipped with CTDs and optical sensors. The surveys focused on two square areas 5 km wide, one centred on the larger CTD sampling area and the other one centred on the near-coastal mooring location. Different sampling strategies allowed mesoscale and submesoscale features to be collected at a horizontal resolution of 250 m. This resolution reveals the spatial and temporal variability of submesoscale dynamics.

The LOGMEC17 sampling strategy allows the collection of synoptic and very high resolution data suitable for the study of NIWs. The characteristics of the platforms used for the present study are summarised in Table 1. The data collected from the two moorings form the basis for this study. The deep mooring is located at the LPCC boundary, while the near-coastal mooring is moored in the region where previous studies (Borrione et al., 2016) revealed strong mesoscale activity.

Platforms	**Parameters**	**Sampling scale / deployment time**	**Spatial scale**	**Depth (m)**
Gliders	T,S,P	Minutes / Monthly	Multi	[0, 1000]
CTD RV Aretusa	T,S,P	Minutes / Daily	Mesoscale Submesoscale	[0, 400]
Scan-Fish	T,S,P	Minutes / Daily	Submesoscale	[0, 150]
Moorings	T,S,P, water current	Minutes / Monthly	Submesoscale	[0, 1000]

Table 1: Platforms, collected data, temporal and spatial scales, and depth reached during the LOGMEC17 campaign. The letters T, S, and P represent temperature, salinity, and pressure measurements, respectively.

Mooring data

The deep mooring was anchored near the 1000-m bathymetric line at 43.86°N, 9.21°E and collected data for two months (13/Sep - 14/Nov). It was equipped with several ocean sensors (Figure 2) and an upward-looking ADCP (150kHz, vertical resolution 8m, sampling period 15 minutes) that collected current measurements from 250m to 20 m depth, taking into account surface contamination according to the ADCP Practical Primer (ADCP Practical Primer, 2011). The temperature sensor with the shallowest operating depth on the deep mooring was located at about 30 m depth (Table A-1).

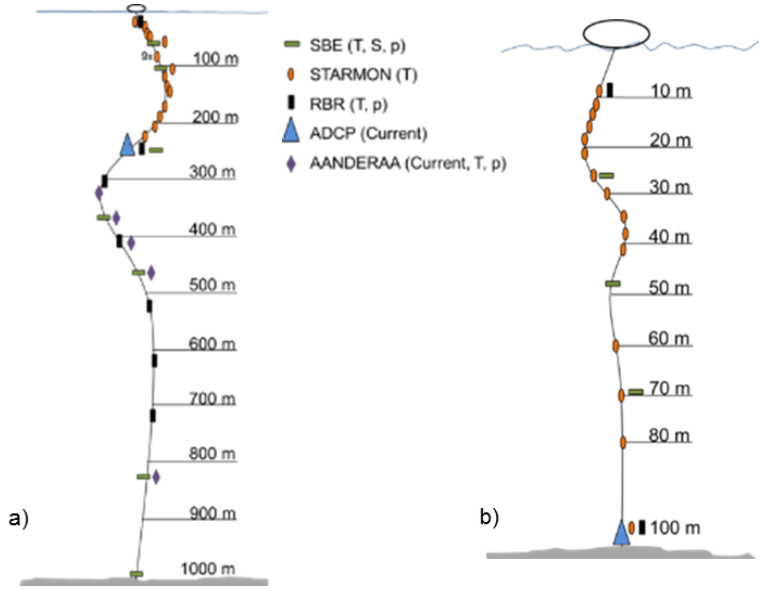

Figure 2: Deep (a) and near-coastal (b) mooring design.

The near-coastal mooring was at 100 m depth at 43.86 °N, 9.83 °E and collected data for one month (27/Sep - 25/Oct). An upward looking ADCP was located near the seafloor (Figure 2). The ADCP (300kHz, vertical resolution 4m, sampling period 15 minutes) measured water currents from 100m to 15m depth. The temperature sensor closest to the surface was located at about 10 m depth (Table A-1).

The distance between the deep and near-coastal moorings was about 50 km.

Additional dataset

In the present study, the glider data are used only to calculate the Mixed Layer Depth (MLD) at the deep mooring because the shallowest temperature sensor at the mooring was below the MLD. The MLD measurements are available when the gliders pass within a range of 2.5km from the deep mooring.

Additional information is provided by temperature and salinity data collected by CTD casts and ScanFish close to the near-coastal mooring.

In order to analyse environmental conditions during LOGMEC17, the L4 sea surface temperature (SST) analysis product is provided by JPL with support from the NASA Making Earth Science Data Records for Use in Research Environments (MEaSUREs) program.

The main generation mechanism of NIWs is wind. In this study, wind data from the operational analyses of the European Centre for Medium-Range Weather Forecasts (ECMWF) are used. The

horizontal spatial resolution of the near-real-time product is 0.125 degrees and the temporal resolution is 3 hours.

Comparison of ECMWF wind data with time series collected from a buoy in the Ligurian Sea near the deep mooring of the LOGMEC17 experiment has shown that ECMWF overestimates measured wind during calm conditions and underestimates wind intensity for near gale and gale-force conditions (Bozzano *et al*., 2004). However, the error in wind intensity does not affect the present study because we are interested in identifying the wind bursts but not in quantifying the wind input.

Data analysis methods

The data collected by the two moored ADCPs are checked by an iterative quality control procedure in which all measurements that fall outside the range defined by the mean of the measurements at that depth ± three times their standard deviation at any measurement depth are flagged as spikes and removed.

The current time series are often analysed by combining the zonal component (u) and the meridional component (v) into a complex horizontal velocity vector (Gonella, 1972, Mooers, 1973, Denbo and Allen 1984, Chen et al., 1996) as follows: $w(t)=u(t)+iv(t)$.

The rotary spectra is applied to the currents, where the velocity vector for a given frequency ω is considered as the combination of the clockwise component characterised by a negative angular frequency and the counterclockwise component with positive angular frequency. In this study, only the clockwise components of the spectra are presented because inertial motions rotate clockwise in the northern hemisphere. The spectral analysis is based on Welch's method (Welch, 1976; Hayes, 1996; Stoica, 2005). The window length is 3 days and the overlap is 50%.

To quantify the amplitude of the currents associated with NIWs, the bandpass filtered currents are obtained by applying a bandpass filter to the current time series. The bandpass filter is applied to the frequencies within f±10%f, which is defined as the near-inertial frequency band.

To investigate the energy propagation of the NIWs over time, the continuous wavelet transform is applied to the complex horizontal velocity vector at different depths using the analytical Morse wavelet (Liu and Miller, 1996; Olhede and Walden, 2002). We refer to the inertial power distribution as the power time series associated with the local inertial frequency.

The NIWs dispersion relation is derived from the linearized hydrostatic Boussinesq equations of motion on f-plane:

$$\omega^2 = f^2 + \frac{N^2 K_H^2}{m^2} \quad (1)$$

where ω is the NIWs frequency, f is the local inertial frequency 1.01 rad s^{-1} (corresponding to 17.3 hours in period), N is the Brunt-Vaisala frequency, K_H and m are the horizontal and vertical wavenumbers respectively.

Two methods are used to estimate the properties of the NIW: the first is based on the complex correlation coefficient method, the second on the cross-spectral analysis of the currents at different depths.

The complex correlation coefficient method (Kundu, 1976; Emery & Thomson 2014) quantifies the correlation and phase between two rotating velocity vectors. The complex correlation coefficient for each pair of bandpass-filtered (f±10%f) current time series is calculated as follows:

$$\rho = \frac{\overline{w_1^*(t)\, w_2(t)}}{\sqrt{\overline{w_1^*(t)\, w_1(t)}}\ \sqrt{\overline{w_2^*(t)\, w_2(t)}}} \quad (2)$$

where 1 and 2 indicate the first and second complex current time series at two different depths, the asterisks indicate the complex conjugate and the overbar denotes the time average. The time window is centred on the peak of the inertial current and the length is four times the inertial period, almost 3 days.

The complex correlation coefficient phase Φ is used to estimate the phase speed C of the NIWs as follows:

$$C = \frac{\omega}{\Phi}\Delta z \quad (3)$$

where Δz is the difference between the depths of the first and second current time series. Estimates of vertical wavenumber m, vertical and horizontal group velocities (C_{gz} and C_{gh}), and horizontal wavenumber K_H are calculated using the dispersion relation (1) (Eq. from 1.3-19 to 1.3-22). For NIWs characterised by redshift, the group velocities and horizontal wavelength are not calculated because the dispersion relation is not valid.

The second method for calculating the phase Φ of the NIWs is based on cross-spectral analysis of the full currents at different depths within the identified strong NIWs. The cross spectra are calculated for a time window equal to four times the inertial period, i.e., nearly 3 days, centred

on the peak of the inertial power. The cross phase associated with the inertial frequency gives the estimated phase Φ of the NIW, and the other parameters are calculated using the dispersion relation (1).

4.3 Results

4.3.1 Environmental conditions during LOGMEC17

Analysis of satellite data (not shown) clearly indicates the presence of LPCC, WCC, and GLG typical of the Ligurian Sea throughout the LOGMEC17 experiment, but ECC does not always flow northward, contrary to the literature. South of 42.6°N, the current east of Corsica flows southward throughout the oceanographic campaign.

Since the Ligurian Sea is characterised by strong eddy activity, we study it from September 27 to 29, when two research vessels sampled mesoscale and submesoscale close to the near-coastal mooring. To complement this dataset and examine the structures over the entire studied area, the SST anomaly is also analysed (Figure 3a,b,c).

The cold water in the northwestern part of the area (1.5°C lower than the mean in the selected period) is typical of the known cyclone (GLG). In the other regions of the domain, the SST is equal to or higher than the mean temperature, reaching 1.5°C more northwest and east of Corsica island. The SST anomaly shows the meandering nature of the LPCC in agreement with the literature and the strong mesoscale and submesoscale activity that characterises the LOGMEC17 experimental area. From September 27 to 28 (Figure 3a,b) the position of some cyclones (negative anomalies) and anticyclones (positive anomalies) changed, while some other features remained similar, such as the structures in the CTD area (black rectangle). Here, the SW region is characterised by warmer water, likely due to the presence of an anticyclone and the NE region by colder water (cyclone). This feature was similar on September 29 (Figure 3c), but on that day mesoscale activity weakened. Objective analysis of temperature measured by CTDs at 40 m depth (Figure 3d) confirms the overall warm water to the south and cold water to the north, highlighting smaller structures. Within the CTD domain, the ScanFish-derived temperature anomaly field (Figure 3e) shows a decrease in the horizontal scale of structures up to 1 km. As the sampling resolution increases, smaller and smaller structures are detected.

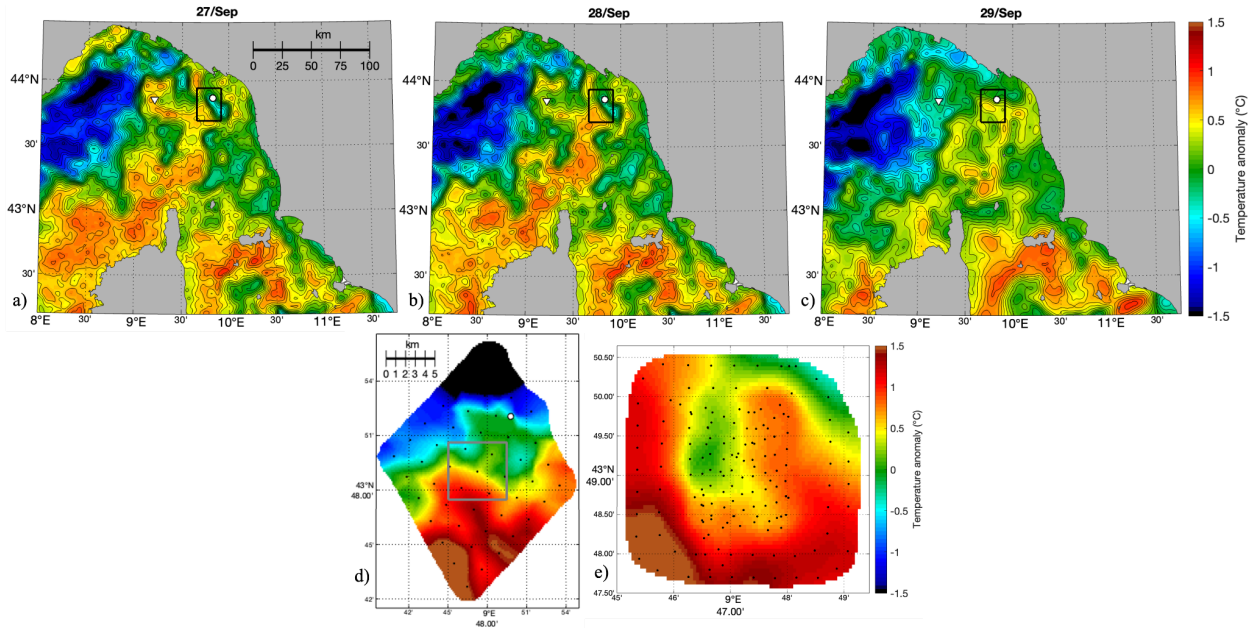

Figure 3: SST anomaly on September 27 (a), 28 (b), and 29 (c). The reference temperature is the mean SST on these days (21.3°C) and the contour interval is 0.1°C. The white triangle and dot indicate the location of the deep and near-coastal mooring, respectively. The black rectangle indicates the CTD sampling area. The lower panels show the temperature anomaly at 40 m depth derived from CTD casts (d) collected from September 27 21:30 to September 29 14:30, and from ScanFish (e) from September 28 09:00 to September 29 16:00. The fields were determined using objective analysis, and the reference temperature for the anomaly is 18.4 °C. The grey square shows the ScanFish operating area. The black dots indicate the location of the data used for the objective analysis.

Since wind is the primary mechanism for NIWs generation, the ECMWF 10m wind amplitude time series averaged over the LOGMEC17 area (Figure 4) is examined. The mean wind speed during the LOGMEC17 experiment is about 5 m s^{-1}. At the beginning of the LOGMEC17 experiment, three wind peaks around 10 m s^{-1} occurred on September 12, 14 and 17, followed by calm conditions. A second peak of the same intensity as the previous bursts occured on October 06 at 21:00, followed by weaker peaks.

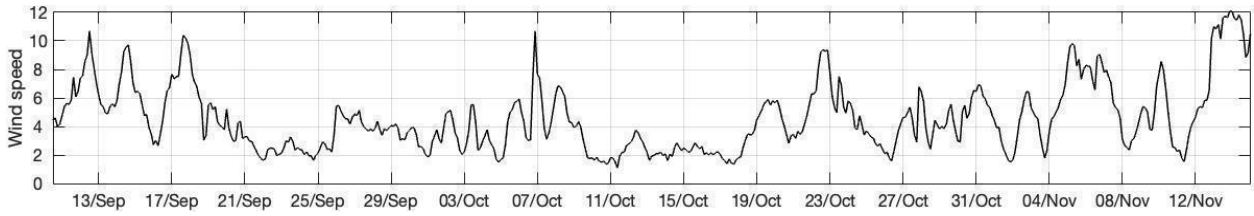

Figure 4: Wind speed time-series (m s^{-1}) averaged over the studied area represented in Figure 1.

The present study is based on the analysis of water currents measured by ADCP from two fixed moorings during the LOGMEC17 campaign. The time series of observed zonal and meridional velocities are shown in Figure 5. The horizontal currents measured at the two moorings have an average magnitude of 0.1 m s^{-1}.

The current direction at the deep and near-coastal mooring is mainly northwest and southeast, respectively. At the deep mooring, the main direction is determined by the Liguro-Provencal Catalan Current (positive meridional, negative zonal velocity components), while the inversions of the flow direction near the coast could be due to eddies (Borrione *et al*., 2016).

The current time series recorded by the two moorings (Figure 5) show periodic tilted stripes along the entire water column, with the tilt angle changing with depth and time. The stripes are more pronounced when the flow is slow and this indicates relevant vertical velocities associated with the NIWs.

At the deep mooring from September 23 to 29, the current reaches 0.3 m s^{-1} from the subsurface to 150 m depth. A second intensification occurs from October 07 to 19 from the subsurface to 60 m depth at both moorings. At the near-coastal mooring from October 23 the current increases up to 0.2 m s^{-1} along the entire water column.

Figure 5 also shows the MLD, which is important for the NIWs. Once inertial oscillations are excited by the wind, the horizontal convergences and divergences lift and deepen the stratified base of the mixed layer and generate NIWs.

Few MLD values are plotted at the deep mooring because the upper temperature sensor was below the MLD. Therefore, the MLD is calculated using data collected by the gliders as they passed within 2.5 km of the deep mooring. The gliders flew by near the deep mooring 12 times from September 29 to November 08. The high vertical resolution of the glider data allows the application of a density-based criterion. The MLD is defined as the depth at which the density changes by 0.05 kg m^{-3}, relative to the density at 10 m depth.

The MLD is at about 20 m deep until October 7, then deepens to about 40 m depth, and from October 13 it starts to fluctuate between 30 and 40 m depth.

At the near-coastal mooring the salinity values are scarce, so the Mixed Layer Depth (MLD) is calculated using the temperature-based criteria (Ruiz *et al*., 2012) with an additional temperature gradient criterion defined after several tests. The MLD is referred to as the depth at which the temperature changes by 0.2 °C and the temperature gradient changes by 0.02 with respect to the temperature at 10 m depth (Kara *et al*., 2000; Qu *et al*., 2007).

At the near-coastal mooring, the MLD is at about 20 m depth until October 7, after which it becomes deeper and fluctuates between 20 and 40 m depth, following the same trend as at the deep mooring.

The MLD values are consistent with the climatology study obtained from the analysis of individual *in situ* profiles (D'Ortenzio *et al.*, 2005). The latter shows that the MLD in the Ligurian Sea is around 15 m depth in September and October, while it reaches 50 m in November.

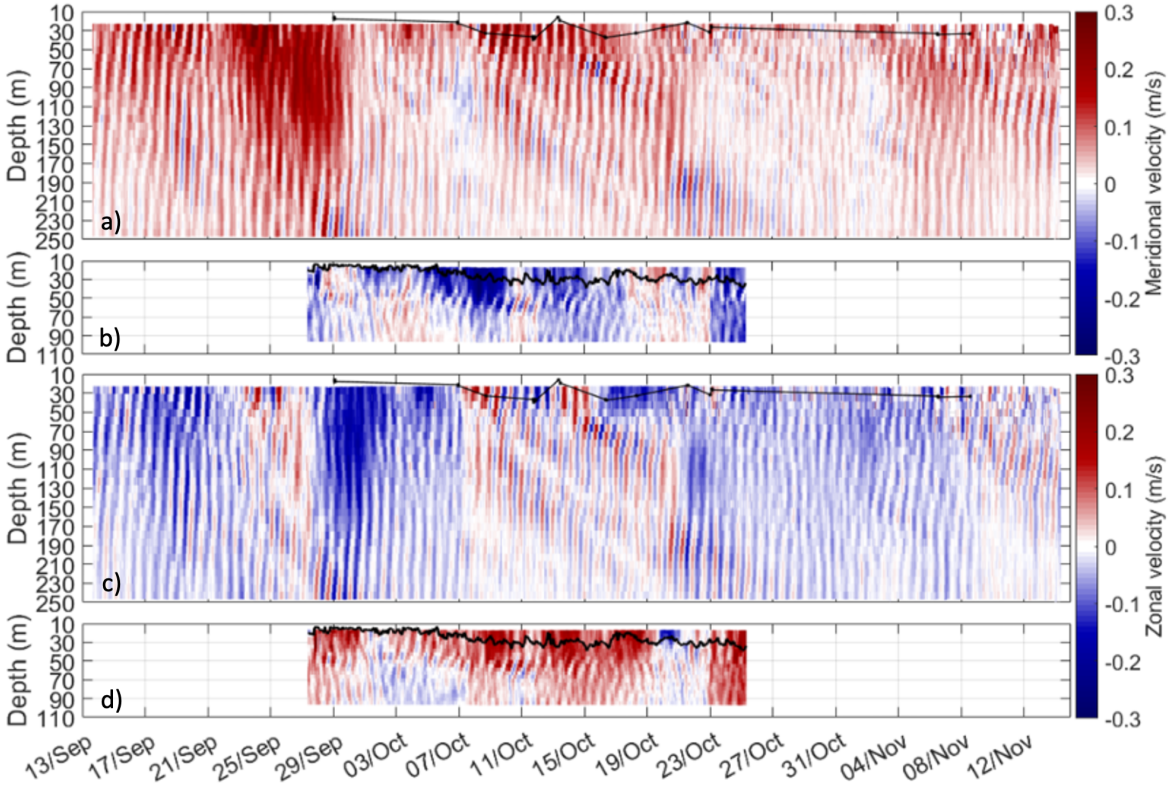

Figure 5: Meridional (a,b) and zonal (c,d) current time-series measured at the deep and near-coastal mooring (upper and bottom panels, respectively). The MLD is denoted by the black lines. At the deep mooring MLD is available when the glider is close to the mooring (black dots).

Most of the temperature and density variability is confined to the MLD at both moorings (Figure 6). Temperature variability is higher at the deep mooring and water masses are colder than at the nearshore mooring. Below 70 m depth, the temperature ranges from 14°C to 15°C, and a cold layer (about 13.5°C) is observed at the deep mooring in the intermediate layers. Below this layer, the temperature of about 14°C and salinity (not shown) of 38.7 indicate the presence of Modified Levantine Intermediate Water (MLIW), consistent with MLIW properties reported in the literature in the Ligurian Sea (Bosse *et al*., 2015, Borrione *et al*., 2019).

At the start of the LOGMEC17 experiment, the temperature around 30 m depth at the deep and near-coastal mooring is 18.5°C and 20°C, respectively, and the colder layer at the deep mooring

is limited to 120 m to 190 m depth. From September 25 to October 01, the cold layer becomes deeper and reaches a depth of 230 m on September 29, when isopycnals deepen below 70 m depth. During the same period, isopycnals at depths shallower than 70 m tend to increase toward the surface. Around October 07, the isopycnals and isotherms become deeper. On October 09, the temperature reaches 16.5°C at 60 m depth and 19°C at the deep and near-coastal mooring, respectively.

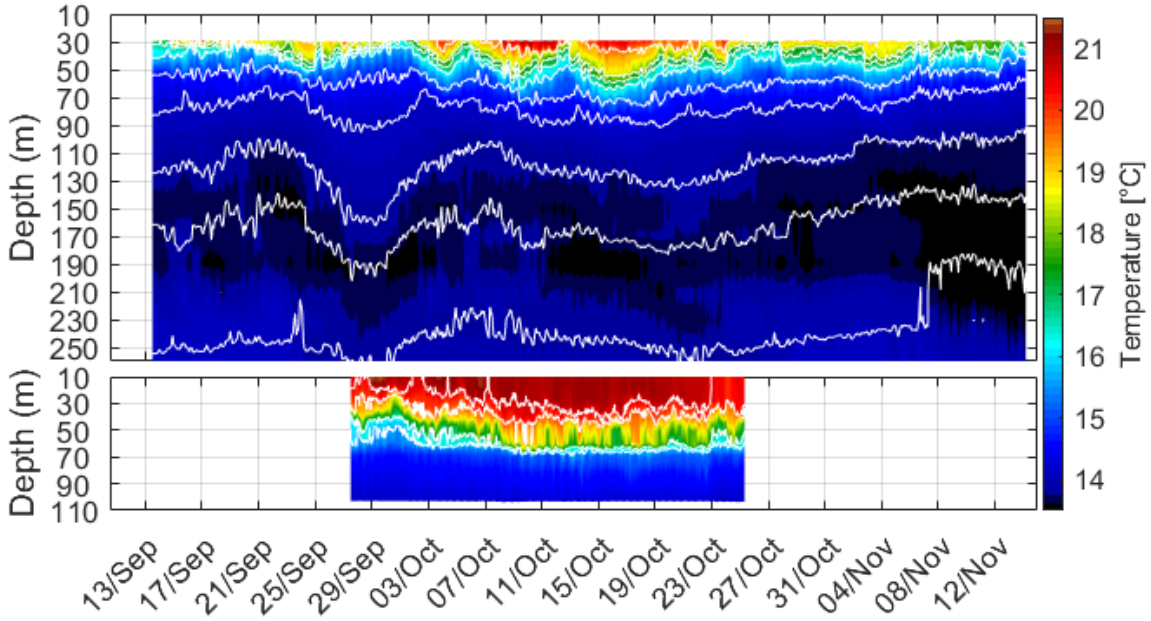

Figure 6: Temperature time-series at the deep mooring (top panel) and at the near-coastal mooring (bottom panel). The white lines indicate the isopycnals (deep mooring 1027.3,1027.7,1027.9,1028.1,1028.4,1028.6,1028.8,1028.9,1029 while for the near-coastal mooring 1027.1,1027.3,1027.9,1028.1).

The Brunt-Vaisala frequency time series (Figure 7) is derived from the temperature and salinity data collected at the two moorings. At the deep mooring, strong stratification is found in the upper layers, while at the near-coastal mooring it is confined in the intermediate layers. At the deep mooring, the maximum stratification tends to follow the variability of the 18.5°C isotherm. The value ranges from 10^{-3} to 10^{-4} rad s^{-2} from the first available layer, about 30 m, to 80 m depth, while lower values are found below 80 m depth. At the beginning of the LOGMEC17 campaign, stratification is strong at the deep mooring at 30 m depth (10^{-3} rad s^{-2}), then it decreases becoming three times weaker within the next two days, while at the near-coastal mooring two layers with strong stratification are found at 45 m and 65 m depth. From October 07, after the second wind gusts, the maximum Brunt-Vaisala frequency at the deep mooring deepens, as do the isotherms, reaching a depth of 70 m on October 09, while the stratification at

the near-coastal mooring increases sharply at a depth of 60 m, reaching a value of 10^{-3} rad s^{-2} from October 07 to 20, fluctuating three times in two days from October 09 to 11.

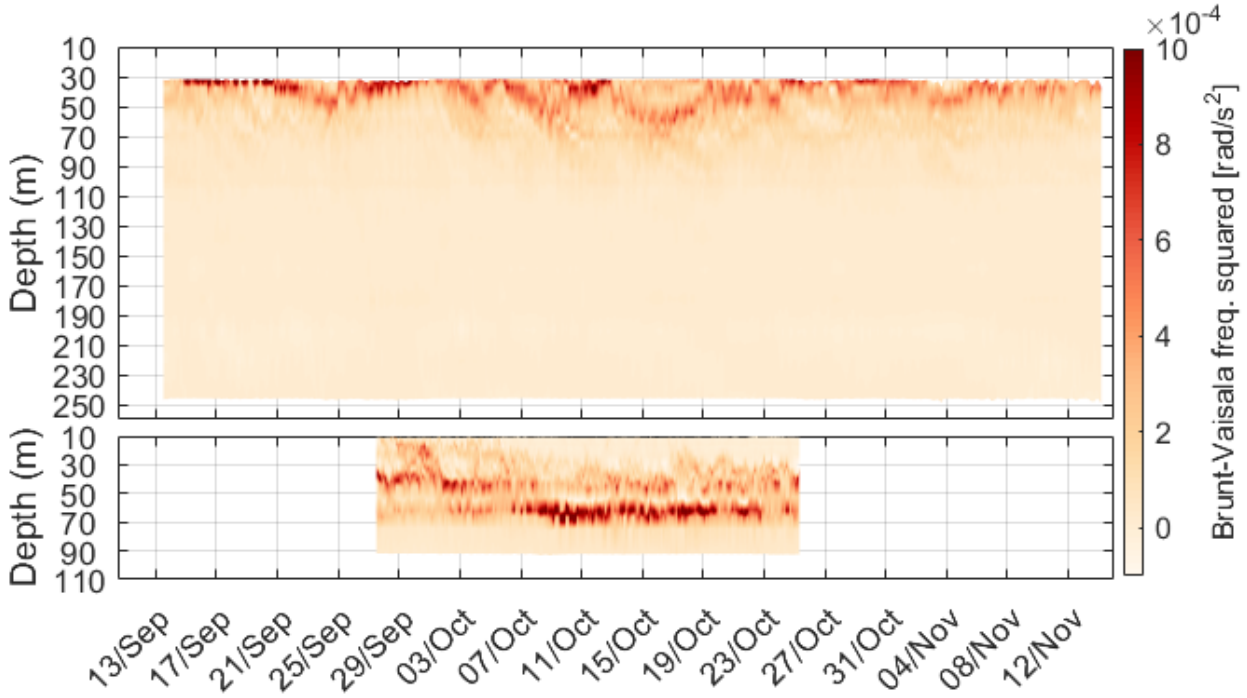

Figure 7: Brunt-Vaisala frequency time-series at the deep (top) and near-coastal mooring (bottom).

4.3.2 Identification of NIWs

The rotary spectra applied to the currents reveals that the frequency of the stripes observed in the current time-series is close to the local inertial frequency (Figure 8) highlighting that the dominant high-frequency processes (period<36h) at the two moorings are NIWs. The energy at the diurnal and semidiurnal tidal periods is low, confirming that the tides are weak (Alberola *et al.*, 1995).

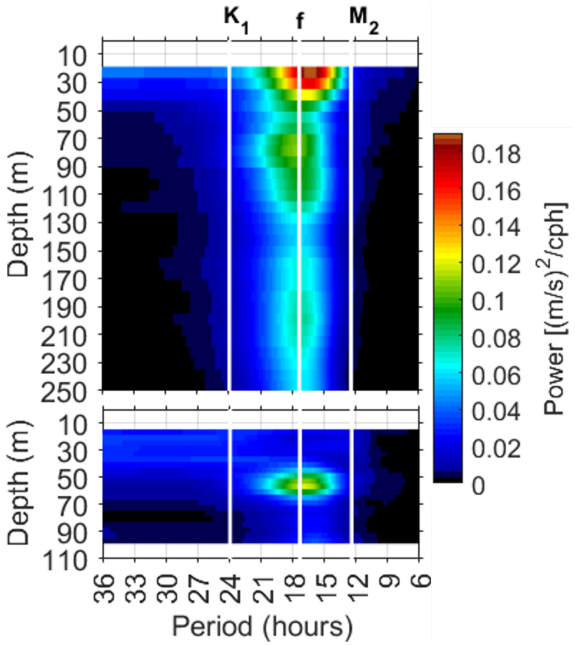

Figure 8: Rotary spectra of the currents at the deep (top) and near-coastal mooring (bottom).

The power distributions along the water column at the two moorings are different. At the deep mooring, the strongest peak occurs from 20 m, the first available ADCP layer, to 40 m depth. A second power peak occurs between 70 and 120 m depth, and a weaker inertial power peak is observed between 150 and 250 m depth.

At the near-coastal mooring, the peak is confined between 40 and 70 m depth. The lack of power below 70 m depth could be due to the shallow bathymetry (100 m). However, the reason for the absence of NIWs near the surface is less clear and will be discussed in more detail in the next section.

To determine when and where NIWs occur, the inertial power distribution at the two moorings is calculated.

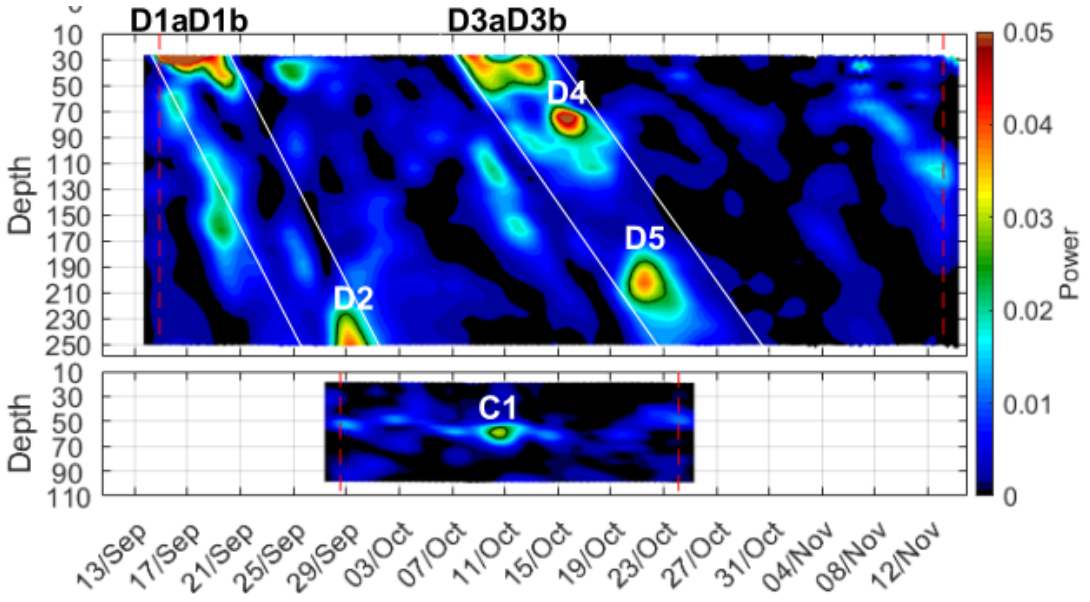

Figure 9: Inertial power distribution (in m^2s^{-2}) at the deep (top) and near-coastal mooring (bottom) respectively. The white lines denote two constrained bands within which the NIWs propagate. The vertical red dashed lines indicate the cone of influence.

Inertial power at the deep mooring (Figure 9) has a background value of 0.01 (m^2 s^{-2}), and the highest values occur within two bounded bands from the subsurface at about 30 m depth to greater depths. These bands occur every three weeks and alternate with periods without strong NIW signals. Here we consider as strong events the NIWs with energy higher than 0.025 (m^2 s^{-2}). The maximum inertial power reaches 0.06 (m^2 s^{-2}) at about 30 m depth from September 15 to 20 and at about 70 m depth from October 14 to 16 (D1 and D4 in Figure 9). The strong NIWs labelled D2, D3, and D5 occur at different depths, their inertial power is around 0.035 (m^2 s^{-2}), but they have different duration and vertical displacement. Table 2 summarises the depths of the detected NIWs, their durations, and the Brunt-Vaisala frequency values averaged during the NIWs. The two NIW events near the surface are characterised by two successive power peaks, which is why the first is labelled with the letter "a" and the second with "b." At the near-coastal mooring (bottom panel in Figure 9), only one strong NIW is identified, which is confined to intermediate layers in agreement with the rotational spectra (Figure 8). The duration of the strong NIWs averages 3 days, with the exception of the event at the near-coastal mooring, which lasts 1.4 days.

NIWs event	Depth (m)	Duration (days)	Brunt-Vaisala frequency (10^{-4} rad s^{-2})
D1a	27-35	3.4	6.6
D1b	27-51	2.5	2.6
D2	227-252	2.3	1.2
D3a	27-51	3.4	4.0
D3b	35-43	3.0	4.9
D4	67-83	2.8	1.3
D5	187-211	2.8	0.1
C1	55-63	1.4	5.8

Table 2: Depth and duration of the NIWs events and the Brunt-Vaisala frequency values averaged during the NIWs event (power>0.025 (m s^{-1})^2).

4.3.3 NIW generation and propagation

Wind blowing on the ocean surface is the main mechanism for NIWs generation (Alford *et al.*, 2016). Here we examine the relationship between wind speed time series (Figure 4) and NIW events (Figure 9).

The proximity of inertial peaks D1 and D3 to the surface indicates that they are locally generated by wind, because the wind time series shows two significant wind gusts preceding these events at the mooring location. In contrast, events D2, D4, D5, and C1 are not locally generated, as indicated by the absence of inertial power near the surface.

The orientation of the first band within which the D1 and D2 events occur (Figure 9) suggests that D2 was generated by the same wind event as D1 (September 14 at 15:00), but its origin was far from the mooring. It propagated downward from the surface and reached a depth of 227 m at the deep mooring after 10 days. Similarly, events D3, D4, and D5 were triggered by the wind gust on October 06 at 21:00, with D3 originating locally, while D4 and D5 originated far from the mooring and their energy propagated downward, so that the deep mooring observed their passages several days later at different depths.

At the near-coastal mooring, C1 is confined in intermediate layers, so it was not generated locally and the propagation path is not clear. If the NIW energy propagates analogously to the observations at the deep mooring during the same period, the wind gust on October 06 at 21:00 preceding the C1 event could generate it.

The orientation of the bands suggests that the inertial energy peaks propagate downward, implying an upward phase propagation typical of NIWs (Leaman & Sanford, 1975). This is

confirmed by cross-spectral analysis (not shown) of the currents at various depths. The exception is D3b, which is characterised by downward phase propagation. This implies that the energy propagates upward during D3b. During this period, the MLD becomes shallower (Figure 5) and the isopycnals (Figure 6) are upward directed, therefore we argue that the NIW of D3b event propagates along isopycnals. The NIW propagating along isopycnals is characterised by the minimum frequency at which it can propagate (Whitt and Thomas, 2013).

On average, the energy of the NIWs propagates within two identified bands. The estimated mean vertical group velocity within the first band (D1,D2) is $2.6 \cdot 10^{-4}$ m s^{-1} while for the second band (D3,D4,D5) it is $1.9 \cdot 10^{-4}$ m s^{-1}. The different shape of the inertial power distribution along the water column suggests that the NIWs have locally different velocities. For example, the energy of the D3a event propagates downward faster than that of the D5 event (the latter has a vertically elongated shape).

The change in NIW properties along the propagation path is also supported by the unexpected enhancement of NIW power at greater depths. Normally, the inertial power decreases with increasing depth. This is not the case, however, and the discrepancy might be explained by the fact that NIWs propagate through different water masses from their point of origin to the deep mooring and interact with other structures that change their properties.

4.3.4 NIW properties

Most of the NIW energy falls in the f±10%f region (Figure 8), which is defined as the near-inertial frequency band. Applying the bandpass filter to the current measured by the two moorings allows us to estimate the NIWs amplitude (Table 3). The strongest NIWs amplitude reaches 0.16 m s^{-1} and the minimum amplitude, which is half of the maximum, occurs at the near-coastal mooring. The average of the observed NIWs amplitude is 0.13 m s^{-1}.

A first estimation of NIW properties is performed through the complex correlation coefficient method (Kundu, 1976; Emery & Thomson 2014), and to increase the confidence level of NIW property estimates, a second method based on cross-spectral analysis is used. For NIWs characterised by redshift, the group velocities and horizontal wavelength are not calculated because the dispersion relation is not valid. Table 3 summarises the properties of the identified NIW events. The first values are estimated using the complex correlation coefficient method, while the second values, marked with asterisks, are obtained by the estimated cross-phase of the NIWs. For the vertical group velocity the third value C_{gz}^{graph} is estimated assuming that the NIWs propagate within the two identified bands (Figure 9).

Event	Amplitude (ms^{-1})	$\frac{\omega}{f}$	C / C^* (10^{-3} ms^{-1})	C_{gh} / C_{gh}^* (ms^{-1})	C_{gz} / C_{gz}^* / C_{gz}^{graph} (10^{-4} ms^{-1})	λ_H / λ_H^* (km)	λ_z / λ_z^* (m)
D1a	0.16	1.08	2.2 / 2.4	0.20 / 0.21	3.2 / 3.4 / 2.6	78 / 84	127 / 135
D1b	0.12	1.09	1.8 / 2.3	0.11 / 0.13	2.9 / 3.6 / 2.6	39 / 48	105 / 130
D2	0.11	1.03	2.8 / 2.8	0.02 / 0.02	1.7 / 1.7 / 2.6	23 / 21	171 / 164
D3a	0.11	0.99	1.9 / 2.2	-	- / - / 1.9	-	120 / 129
D3b	0.11	1.03	-12.8 / -10.6	-0.63 / -0.52	6.8 / 5.7 / 1.9	715 / 595	775 / 645
D4	0.16	0.97	1.0 / 1.0	-	- / - / 1.9	-	62 / 60
D5	0.11	1.02	2.5 / 2.4	0.01 / 0.01	0.8 / 0.7 / 1.9	26 / 23	153 / 139
C1	0.08	1.02	0.6 / 0.5	0.03 / 0.03	0.3 / 0.2 / 1.9	38 / 34	35 / 31

Table 3: NIWs event, amplitude, frequency shift as ratio between observed frequency and local inertial frequency f, phase velocity C, vertical (C_{gz}) and horizontal (C_{gh}) group velocity, horizontal (λ_H) and vertical (λ_z) wavelength. The first value is estimated using the complex correlation coefficient method while the second value, marked with an asterisk, is estimated starting from the cross-phase of the NIWs. C_{gz}^{graph} is the mean vertical group velocity estimated graphically assuming that the NIWs propagate within the two identified bands (Figure 9).

Overall, the NIWs parameters estimated by the two different methods agree well. The estimated horizontal group velocities are three orders of magnitude larger than the vertical group velocities. The properties of D3b are clearly different from all other observed NIWs. The NIW energy propagates faster near the surface than at greater depths in both vertical and horizontal directions.

The mean vertical group velocity of D1 and D2 using the two methods is $2.5 \cdot 10^{-4}$ m s^{-1}, which is comparable to the previously estimated velocity (C_{gz}^{graph}), assuming that NIWs propagate within the first constrained band (Figure 9). It confirms that NIWs propagate on average within the identified bands, but their group velocities change during their propagation path. Vertical group velocity varies from a maximum of $6.8 \cdot 10^{-4}$ m s^{-1} during the D1a event to a minimum of $0.3 \cdot 10^{-4}$ m s^{-1} at the near-coastal mooring. The horizontal group velocity reaches 0.63 m s^{-1} during D3b and 0.012 m s^{-1} during D5. The phase velocity at the deep mooring is $2.1 \pm 0.6 \cdot 10^{-3}$ m s^{-1} except during D3b, where the value is almost an order of magnitude higher. Excluding the D3b event, the mean vertical and horizontal wavelengths of the observed NIW at the deep mooring are 125±35m and 43±25km, respectively. At the near-coastal mooring, the estimated vertical wavelength is shorter, 33±2m, which is reasonable given the bathymetry of 100m depth and the horizontal wavelength of 36±2km. As an additional check (not shown), we compare the NIW wavelengths with those estimated from the bandpass filtered current, and find good agreement.

4.3.5 NIWs frequency shift

Most of the observed NIW frequencies are higher than the local inertial frequency, the so-called blue shift (Elipot *et al.*, 2010; Fu 1981). NIWs D3a and D4 are exceptions; in these cases the frequency is slightly lower than the inertial frequency (a red shift) (Table 3). Event D1b exhibits the strongest frequency shift, which is 9% higher than the local inertial frequency, while the frequency of D4 is 3% lower than the inertial frequency.

The frequency shift could be due to the nonlocal generation of NIWs. The observed NIWs could be generated at a location characterised by a local inertial frequency equal to the NIW frequency observed at the two moorings. Once generated, these waves could propagate toward the moorings, maintaining the same frequency. If one calculates the latitude of the area of origin, it is on land. Obviously, the waves could not have originated on land, so this hypothesis can be ruled out. Other mechanisms that could cause the observed frequency shift are the interaction of the NIW with strong internal tides and with mesoscale structures and fronts.

Spectral analysis of the currents shows very low tidal signals during the LOGMEC17 experiment (Figure 8). In addition, model simulations (not shown) were performed in the LOGMEC17 domain using a similar setup to the Centre for Maritime Research and Experimentation regional ocean forecast system (Storto et al., 2019) with and without tidal inputs, and in both numerical experiment setup the NIWs energy is dominant in the power spectrum of the velocity field. This confirms that tides are not responsible for the observed frequency shift.

The most likely cause of the NIWs frequency shift is the interaction of waves with small-scale structures, because the LOGMEC17 experimental area is characterised by strong mesoscale and submesoscale activity, as shown by the satellite, CTD, and ScanFish data (Figure 3). As the sampling resolution increases, smaller and smaller structures are detected, reaching a horizontal scale of 1 km. This supports the hypothesis that the interaction of the NIW with these structures is the main cause of the frequency shift observed at the two moorings. Kunze (1985) defined the effective NIWs frequency as $f_{eff} = f + \frac{\zeta}{2}$ where ζ is the background vorticity. A positive (negative) vorticity, i.e., a cyclone (anticyclone), causes a blue (red) shift in the NIWs frequency. Unfortunately, CTD and ScanFish data were not collected during the observed NIWs at the two moorings, and the resolution of the satellite data is too low to investigate the interaction of NIWs with mesoscale and submesoscale eddies. Only some information can be obtained from the deepening and shallowing of isopycnals (Figure 6). During the D3a event (from October 8), the isopycnals deepen, indicating the presence of an anticyclone, which is consistent with the observed red-shifted frequency. Around October 11, a shallowing of isopycnals could indicate the arrival of a cyclone, which probably explains the blue shift of the D3b event. The D4 event is characterised by a blue shift that appears to be consistent with the deepening of isopycnals on October 15 and thus the presence of an anticyclone. The spatial and temporal distribution of the

in situ observations is not sufficient to draw robust conclusions about the interaction of NIW with mesoscale structures.

4.4 Discussion and conclusions

During the LOGMEC17 campaign, spectral analysis of the currents measured at two fixed moorings shows that the high-frequency processes are dominated by NIWs. The observed NIWs are fully characterised in the Ligurian Sea, in terms of their depth, duration, frequency, wavelength, phase velocity and group velocity.

At the deep buoy moored at 1000 m depth, strong NIWs are identified along the entire sampled water column (from 30 to 250 m depth), while at the near-coastal mooring, anchored at 100 m depth, only a single strong NIW is detected, limited to the middle layers (55-63 m depth). The presence of NIW energy throughout the sampled water column confirms that these waves contribute to both surface and deep water mixing.

On average, the NIW energy identified at the deep mooring propagates downward within two bands occurring once every three weeks (Figure 9). The near-surface NIWs (D1 and D3) are generated locally by wind gusts, while the deeper ones (D2, D4, D5, and C1) are generated in other regions. The wind peak that occurs on September 14 at 15:00 generates the D1 event at the deep mooring but also the D2 event in another region. The D2 energy propagates downward from the surface and reaches a depth of 227 m at the deep mooring after 10 days with a mean vertical group velocity of 2.6 10^{-4} m s^{-1}. Similarly, events D3, D4 and D5 are triggered by a second wind gust on October 06 at 21:00. The D3 event is generated locally at the deep mooring while D4 and D5 originated far from the mooring and their energy propagates downward with a mean velocity of $1.9 \cdot 10^{-4}$ m s^{-1}. The D4 event was generated at a shorter distance from the deep mooring with respect to the D5 event as the mooring observed it several days before than D5.

At the near-coastal mooring the C1 event is originated by the same wind burst as D3, D4 and D5 (October 06 at 21:00) but it is not locally generated and it is confined in intermediate layers only likely due to the presence of the seafloor at 100 m depth.

The vertical group velocity of the NIWs changes along the water column. The energy of NIWs propagates both vertically and horizontally faster near the surface than at greater depths. Only one NIW (D3b) is characterised by upward energy propagation (downward phase) along isopycnals. Most of the observed NIWs are characterised by a blue shift, consistent with many other observations. During LOGMEC17, the blue shift reaches 9% above the local inertial frequency and two NIWs show a slight red shift up to 3% below the inertial frequency. The frequency shift is likely caused by the interaction between NIWs and mesoscale eddies. Intense mesoscale and submesoscale activity is observed in the studied area with satellite, CTD casts and

ScanFish (Figure 3), but *in situ* observations are not enough to conduct an in-depth investigation on the interaction between NIWs and mesoscale and submesoscale structures.

The average amplitude of the observed NIWs is 0.13 m s^{-1}, which is 0.03 m s^{-1} higher than the global average NIW amplitude (Chaigneau *et al*., 2008). The NIW amplitude does not decrease with increasing depth, likely due to interaction with various processes and water masses along the propagation path. The horizontal and vertical wavelengths of the downward propagating NIWs at the deep mooring are 43±25 km and 125±35 m, respectively. At the near-coastal mooring, the estimated horizontal and vertical wavelengths are 36±2 km and 33±2 m, respectively. These values are comparable to estimates from a previous study in the Eastern Mediterranean Sea (Cuypers *et al*., 2012), which determined horizontal and vertical wavelengths of 10 to 100 km and 100 to 150 m, respectively. The shorter vertical wavelength at the near-coastal mooring is likely due to the presence of the seafloor at 100 m depth.

This study confirms that the study of NIWs is challenging (Alford *et al.*, 2016). Although LOGMEC17 is a multiplatform and multiscale campaign, the interaction of NIWs with mesoscale structures was not fully investigated because the mesoscale and submesoscale in the experimental area were not sampled during the strong NIWs events. Collecting high-resolution *in situ* observations over a long period of time is difficult and costly: moorings are sparse and fixed, gliders are slow and collect data on a zigzag trajectory, ships collect data in a limited area and for a limited period of time, satellites measure only the sea surface, and horizontal resolution is insufficient to detect submesoscale structures.

In support of *in situ* observations, a high-resolution numerical model would greatly improve understanding of the generation region of NIWs and their interaction with meso- and submesoscale structures.

Appendix

This study is based on data collected during the LOGMEC17 sea trial at two fixed moorings: the near-coastal mooring and the deep mooring. The moorings were equipped with multiple sensors. The sensors in operation and their average depths from surface to ADCP depth are listed in Table A-1. The Starmon sensors measure temperature, the RBR sensors collect temperature and pressure data, while the SBE measures temperature, salinity, and pressure with a sampling period of 10 seconds.

Sensor type	Average depth (m)
RBR	30
Starmon	30
Starmon	35
Starmon	41
Starmon	51
SBE	57
Starmon	57
Starmon	62
Starmon	67
Starmon	72
Starmon	78
Starmon	88
Starmon	93
Starmon	98
Starmon	103
SBE	108
Starmon	108
Starmon	129
Starmon	150
Starmon	170
Starmon	190
Starmon	211
Starmon	231
RBR	249
SBE	250
ADCP	251

Sensor type	Average depth (m)
RBR	10
Starmon	10
Starmon	12
Starmon	14
Starmon	17
Starmon	19
Starmon	21
SBE	26
Starmon	26
Starmon	30
Starmon	34
Starmon	38
Starmon	42
SBE	47
Starmon	60
SBE	69
Starmon	69
Starmon	81
RBR	103
Starmon	103
ADCP	103

Table A-1: Deep mooring (left) and near-coastal mooring (right), the operating sensors and their average depths from the surface to the depth of the ADCPs.

5. Near-inertial waves interaction with mesoscale structures in the Northwestern Mediterranean Sea

This chapter is a manuscript to be submitted to a scientific journal for publication.

Abstract

A high-resolution numerical model is used to support studies of strong Near-inertial internal waves (NIWs) observed during the Long-term Glider Missions for Environmental Characterization (LOGMEC17) sea trial led by the NATO Centre for Maritime Research and Experimentation in the northwestern Mediterranean Sea in fall 2017. The model, based on NEMO v4.0.4, uses the two-way nesting approach to achieve the required high horizontal resolution in the studied area. Simulation results, performed under realistic conditions, show good agreement with observations. The model confirms that NIWs are the dominant high frequency processes (period < 36h) in the Ligurian Sea during the LOGMEC17 experiment. The model results also confirm that the studied region is characterised by strong mesoscale activities that strongly interact with NIWs by modifying their properties. The most energetic NIWs are wind-generated in the northwestern part of the domain and their frequency changes over the studied area. In agreement with previous studies, anticyclones (cyclones) shift the NIW frequency to lower (higher) frequencies. The interaction between the most energetic NIWs and the strongest mesoscale structures is analysed in detail. A cyclone dampens the NIW energy, while an anticyclone $\left(\frac{\zeta}{f}\sim -0.2\right)$ traps the NIWs energy downward into the deep ocean. In contrast, another strong anticyclone $\left(\frac{\zeta}{f}\sim -0.42\right)$ is characterised by the absence of NIWs energy. We argue that in the surface layers some of the NIW energy coming from the north of this anticyclone is diverted around it, while part of the energy could be dissipated as it encounters strongly slanted isopycnals. At greater depths, energy follows isopycnals passing beneath the anticyclone and rising to the surface farther south.

5.1 Introduction

Near-inertial internal waves play a key role in the ocean circulation energy balance, containing half of the energy of the ocean internal wave spectrum (Ferrari and Wunsch 2009). These waves cause strong vertical shear and therefore contribute significantly to vertical mixing in shallow water (Hebert and Moum 1994; Alford and Gregg 2001) and in the deep ocean (Silverthorne and Toole 2009). NIWs are capable of increasing the ocean mixed layer depth by up to 30%, they affect climate (Jochum *et al*., 2013), and they impact a variety of processes by transporting energy at different scales.

NIW are generated primarily by wind (Alford *et al*., 2016), and they can propagate far from their source areas before breaking (Ray & Mitchum 1996, Alford 2003, Zhao & Alford 2009). Most NIW energy propagates downward, suggesting upward phase propagation (Sanford 1975; Leaman and Sanford 1975, D'Asaro and Perkins 1984), but exceptions have been observed (Alford *et al*., 2016).

The horizontal wavelengths of NIW vary from tens to hundreds of kilometres, while the vertical wavelength is three orders of magnitude shorter (Kundu 1976, Kawaguchi *et al*., 2020). The interaction of NIW with mesoscale features is one of the possible causes of the shift in wave frequency with respect to the local inertial frequency (Kunze 1985, Poulain 1992, Rainville and Pinkel 2004, Young and Jelloul 1997, Asselin and Young 2020). Kunze (1985) proved that anticyclones (cyclones) shift the frequency of NIWs to lower (higher) frequencies, which determines the so-called red shift (blue shift). He defined the lowest limit of the internal wave frequency band, also called the effective Coriolis frequency, as the local inertial frequency plus half the background relative vorticity. Most of the observed NIW frequencies are blue-shifted, but this could also be due to the latitudinal variation of the Coriolis frequency, the so-called β effect (D'Asaro *et al*., 1995), since NIW propagate mainly equatorward and the inertial frequency in the source region is higher than that of the observation site (Simmons and Alford 2012). Both the β effect and mesoscale features contribute to reducing the horizontal scale and increasing the vertical speed of waves (Klein *et al.*, 2004). Moreover, anticyclones can act as waveguides that trap NIWs energy downward into the deep ocean (Zhai *et al.* 2005; Danioux *et al*. 2008), this is the so-called "inertial chimney effect" (Lee and Niiler 1998), but NIWs could also be trapped only at the base of the anticyclone (Kunze 1986; Kunze *et al*., 1995; Oey *et al*. 2008; Joyce *et al*., 2013; Martínez-Marrero *et al.*, 2019; Kawaguchi *et al*., 2019; Asselin and Young 2019). Observations of the "inertial chimney effect" in anticyclonic regions are scarce and incomplete (Alford *et al.*, 2016). Since the anticyclone shifts the frequency of NIWs below the local inertial frequency, NIWs cannot propagate out of the anticyclonic region but remain trapped and reflect both horizontally and vertically off the sides of the anticyclone. The NIWs propagate downward and encounter a critical layer at the base of the anticyclone, where the group velocity vanishes.

The present work is motivated by observations of strong NIWs (Cozzani *et al*., to be submitted) during the multi-platform, multi-scale and multi-disciplinary Long-term Glider Missions for Environmental Characterization (LOGMEC17) experiment led by NATO-CMRE and conducted in the Ligurian Sea (northwestern Mediterranean) in fall 2017. The Ligurian Sea is the region where the Western Corsican Current (WCC) and the Eastern Corsican Current (ECC) (Astraldi and Gasparini, 1992) form the Liguro-Provencal Catalan Current (LPCC). Strong mesoscale structures have been observed in this region (Crépon *et al*., 1982, Flexas *et al*., 2005) and eddy activity north of Corsica, where WCC and ECC form the LPCC, has been studied (Casella *et al.*, 2014, Borrione *et al*., 2016). The time windows of mesoscale activity from late fall to winter are 3-6 days, while in summer they are 10-20 days (Taupier-Letage and Millot, 1986, Sammari *et al*., 1995; Echevin *et al.*, 2003). Modelling studies in this region revealed mesoscale structures with a horizontal scale of 18-20 km (Casella *et al.*, 2014), which was confirmed by observations (Schroeder *et al.*, 2014; Borrione *et al.*, 2016). This can be explained by the magnitude of the Rossby radius of deformation in the northwestern Mediterranean, which ranges from 10 to 20 km (Marullo *et al*., 1985; Guihou *et al*., 2013).

Despite the key role of NIW in the ocean, observations and numerical studies of NIW in the Mediterranean Sea are scarce. Recently, strong NIWs have been observed in the eastern Mediterranean (Cuypers *et al.*, 2012) with horizontal and vertical wavelengths of 10 to 100 km and 100 to 150 m, respectively. Based on these observations, a numerical model was implemented to study the interaction of NIW with the semipermanent anticyclonic Cyprus Eddy (Lelong *et al*., 2020). The latter study showed that the eddies interact with NIWs by changing their wavelengths and that the anticyclone facilitates the transfer of wind-driven inertial energy to propagating waves. In addition, ray-tracing analysis showed that multiple critical levels (where the wavenumber tends to infinity and the group velocity tends to zero) form when inertial rays originate within the anticyclone and most of the energy is located at the base of the eddy, while rays generated outside this region are not associated with critical levels but can concentrate at the base of the eddy and propagate downward.

In the northwestern Mediterranean, NIWs are the main components of the regional internal wave spectrum, as observed by Millot and Crèpon (1981), Van Haren and Millot (2003), and Picco *et al*. (2010). Numerical simulations in this region have shown that NIWs cause shear-induced mixing and SST cooling (Small *et al*., 2012).

The NIWs observed during the LOGMEC17 campaign were characterised in Cozzani *et al*. (to be submitted), and to better investigate how NIWs frequency is affected by mesoscale features, a numerical model was implemented. The present study investigates the interaction of NIW with mesoscale structures in the experimental area.

The paper is organised as follows. Section 2 describes the NIWs observed during the LOGMEC17 campaign, the model setup we implemented, and the methods used to analyse the

data. Numerical model results are presented in Section 3, starting with the comparison between observed and simulated NIWs and the study of their interaction with mesoscale activities in horizontal and vertical directions. Section 4 discusses the modelling results and provides a conclusion of the study.

5.2 Data and Methods

5.2.1 Observations: LOGMEC17 experiment

The Long-term Glider Missions for Environmental Characterization 2017 (LOGMEC17) is a multi-platform, multi-scale, multi-disciplinary combined acoustic and oceanographic campaign led by the NATO Centre for Maritime Research and Experimentation. The sea trial took place in the Ligurian Sea from 13 September to 14 November 2017, and aimed to investigate the variability and predictability of Ligurian Sea properties at different scales. The large scale was sampled by two oceanographic deep gliders, while two oceanographic moorings equipped with several multidisciplinary sensors provided high-frequency observations at fixed points (Figure 1). Spectral analysis of the currents detected by the two moorings showed that NIW dominated the high-frequency processes in the study area. At the buoy moored at 1000 m depth, strong NIWs were detected from 30 to 250 m depth (ADCP depth), while at the near-coastal mooring, anchored at 100 m depth, only one strong NIW was observed, located in intermediate layers (55-63 m depth).

The NIW observed near the surface were generated locally by wind gusts, while the deeper NIW were generated in other regions. On average, the identified NIWs energy at the deep mooring propagated downward within two constrained bands with a mean vertical group velocity of $1.9 \cdot 10^{-4}$ and $2.6 \cdot 10^{-4}$ m s^{-1} , but it changed locally along the water column varying from $0.7 \cdot 10^{-4}$ to $6.8 \cdot 10^{-4}$ m s^{-1}. Near the surface, the energy of the NIWs propagated faster in both vertical and horizontal directions than at greater depths.
Most of the observed NIW frequencies were characterised by a blue shift that was up to 9% above the local inertial frequency, and two NIWs exhibited a slight red shift that was up to 3% below the inertial frequency. The analysis of the data set collected during the LOGMEC17 experiment showed strong mesoscale activity in this region, as described in the literature (Casella *et al*., 2014; Borrione *et al.*, 2016). Nevertheless, the spatial and temporal distribution of the *in situ* observations was not sufficient to draw robust conclusions about the interaction of NIW with mesoscale structures, so we decided to implement a numerical model to better investigate this.

A full characterization of the observed NIWs that motivated the present numerical study is provided in Cozzani *et al.,* (to be submitted).

5.2.2 Ocean model

The ocean model implemented for the present study, called Ligurian Sea Model (hereafter LISM), is based on the Nucleus for European Modelling of the Ocean (NEMO) version 4.0.4 (Madec *et al*., 2019). The NEMO model solves the three-dimensional primitive equations under the Boussinesq, hydrostatic and incompressibility approximations. The horizontal resolution of the parent LISM is about 1.3 km and a two-way nested domain, so-called child domain (Figure 1), reaches 400 m in the experimental area.

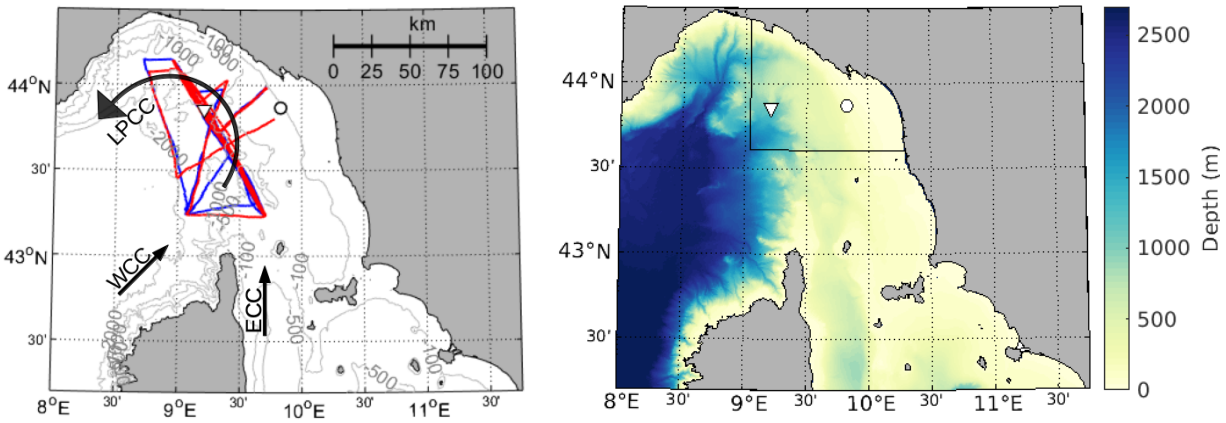

Figure 1: Left panel: Map of the Ligurian Sea showing bathymetry (thin grey lines), main currents, and locations of the deep mooring (triangle) and near-coastal mooring (dot). The trajectories of the two deep gliders during LOGMEC17 are indicated by the red and blue lines. Right panel: parent domain with bathymetry and boundaries of the LISM child domain area denoted by black lines.

In both domains, the vertical grid of 141 unevenly zeta spaced levels is discretized with partial steps (Barnier *et al*., 2006). The parent domain is bounded by two open boundaries on the western and southern sides at 8.0°E and 42.2°N, respectively, while the child domain is centred on the two moorings observed by NIWs during the LOGMEC17 experiment. Bathymetry is provided by the General Bathymetric Chart of the Oceans (GEBCO) (Weatherall *et al*., 2015).

To optimise the computation time, the slow and fast processes are solved using a split-time-step technique. In the parent model, the time step for the baroclinic component is 150s, while in the child it is 50s and the barotropic part is computed in 40 and 20 subloops, respectively.

Previous modelling work on NIW (Alford, 2020) has shown that absolute wind work values are overestimated compared to values calculated using the wind relative to the ocean current, so relative wind is used.

The advection scheme for active tracers is the 4th order Flux Correct Transport scheme (Zalesak, 1979) and horizontal diffusion is solved by a bi-laplacian operator along iso-neutral surfaces. A 3rd order upstream scheme (Shchepetkin and McWilliams, 2005) is used to solve the advective terms of the momentum equation, while for the viscous term a bi-laplacian operator is applied

along the iso-level surfaces. To ensure numerical stability and minimise numerical dissipation, the horizontal diffusivity and viscosity values are uniform in the interior of the model domain ($5 \cdot 10^5$ m^4s^{-1} and 10^6 m^4s^{-1}, respectively) and double starting from ten grid points near the coast and at the lateral open boundaries. For consistency with the CMEMS model, the atmospheric pressure term is added to the governing equations. The vertical turbulence coefficients are calculated using the Generic Length-Scale turbulence closure scheme (Umlauf and Burchard 2003, 2005), where the generic length scale is calculated using a k-kl turbulence closure (Mellor and Yamada 1982).

In LISM, eight major components (Q1, O1, P1, K1, N2, M2, S2, and K2) of tidal elevations and velocities from TPXO (Padman and Erofeeva, 2004) are superimposed on the lateral open boundary conditions, and the tidal potential is added to the surface pressure gradient calculations.

5.2.3 Numerical experiment setup

The parent model is initialised with the Copernicus Marine Environmental Monitoring Service (CMEMS) (Le Traon *et al*., 2019) Mediterranean Sea operational model output (Oddo *et al.*, 2014) at 1/24° spatial resolution. The CMEMS reanalysis products with hourly resolution are also used as lateral open boundary conditions (LOBCs). The LOBCs are one-way nested with a procedure that uses a Flather formula (Flather *et al*., 1976) for barotropic velocities, a flow relaxation scheme for baroclinic velocities, and a radiation scheme for active traces (Oddo and Pinardi, 2008).

The model was initialised on July 15, 2017, two months before the start of the LOGMEC17 experiment, to allow for proper evolution of the dynamics solved by the higher resolution of the model.

The surface heat flux is adjusted with the satellite level-4 Sea Surface Temperature provided by CMEMS using a Newtonian relaxation algorithm. A retroaction term is added to the surface heat flux using a flux formulation. The feedback coefficient is -40 $Wm^{-2}K^{-1}$ at night time and gradually decreases to zero at noon time because the SST analysis is based on nighttime measurements. Chlorophyll satellite products provided monthly by CMEMS are used to calculate the light extinction coefficient (Lengaigne *et al*., 2007).

Surface boundary condition fields are calculated using the COARE 3.5 algorithm (Edson *et al*., 2013), starting from the atmospheric fields of air temperature, humidity, winds, and cloud cover provided by the European Centre for Medium-Range Weather Forecasts (ECMWF).

A comparison of ECMWF wind data with a time series collected from a buoy in the Ligurian Sea near the deep mooring of the LOGMEC17 experiment has shown that ECMWF overestimates the measured wind during calm conditions and underestimates the wind intensity during near

gale and gale conditions (Bozzano *et al*., 2004). Since wind is the main mechanism for generating NIWs, we compared the ECMWF and the scatterometer level-3 data near the two moorings (Figure 2) and concluded that, overall, the ECMWF wind data agreed well with the satellite-measured data, but the wind speed at 21:00 on 06 October (before the main NIWs observed during the LOGMEC17 experiment) was almost half that observed by the scatterometer. Another wind peak at 03:00 on 08 October appears from the ECMWF time-series but no scatterometer data is available during this event. Considering the study conducted by Bozzano and co-authors and the fact that the observed and simulated NIWs were comparable when doubling the intensity of both the first and second wind peaks (Figure 3), we decided to force the LISM using the doubled wind speed for both wind peaks (Figure 2) over the studied area.

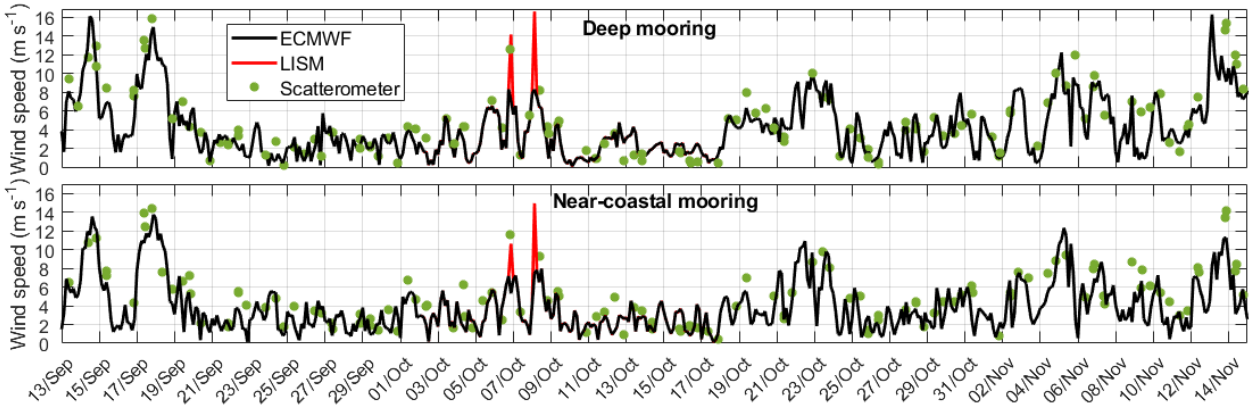

Figure 2: Original ECMWF time series (black) of wind speed, the two wind peaks used for LISM (red), and scatterometer L3 data (green dots) at the deep (top) and near-coastal (bottom) mooring.

5.2.4 Data analysis method

The time series of current vector fields are often analysed using rotating circularly polarised components (Gonella, 1972, Mooers, 1973, Denbo and Allen 1984, Chen et al., 1996). The complex horizontal velocity vector is defined by combining the zonal (u) and meridional (v) components of the currents as follows:

$w(t)=u(t)+iv(t)$

Rotary analysis of currents considers the velocity vector for a given frequency ω as two separate rotating circular components: the clockwise component with negative angular frequency and the counterclockwise component with positive angular frequency. In the northern hemisphere,

inertial motions rotate clockwise (Thomson and Emery, p. 454), so only the clockwise components of the spectra are presented in this study.

The spectral analysis applied to the current time series is based on Welch's method (Welch, 1976; Hayes, 1996; Stoica, 2005), using 3 days as the window length and 50% of the overlap.

To determine the period when the most energetic NIWs occur, the continuous wavelet transform is applied to the currents sampled at different depths, using the analytical Morse wavelet (Olhede and Walden, 2002). The zonal and meridional currents are combined to form the complex horizontal velocity vector as described previously. Since we focus on the NIWs rotating clockwise in the northern hemisphere, only the clockwise component is considered (Liu and Miller, 1996). In the present work, we refer to the inertial power distribution as the power time series associated with the local inertial frequency.

According to Kunze (1985), the effective NIWs frequency is defined as $f + \frac{\zeta}{2}$, where f is the local inertial frequency and ζ the vertical relative vorticity. To remove the high frequency signal, the vorticity field is filtered with a moving average over 36 hours.

5.3 Results

5.3.1 Comparison observed and simulated NIWs

To qualitatively evaluate the performance of the model in reproducing the observed NIWs, the rotary spectra of the currents measured at the two moorings during LOGMEC17 are compared with the spectra of the simulated currents (Figure 3).

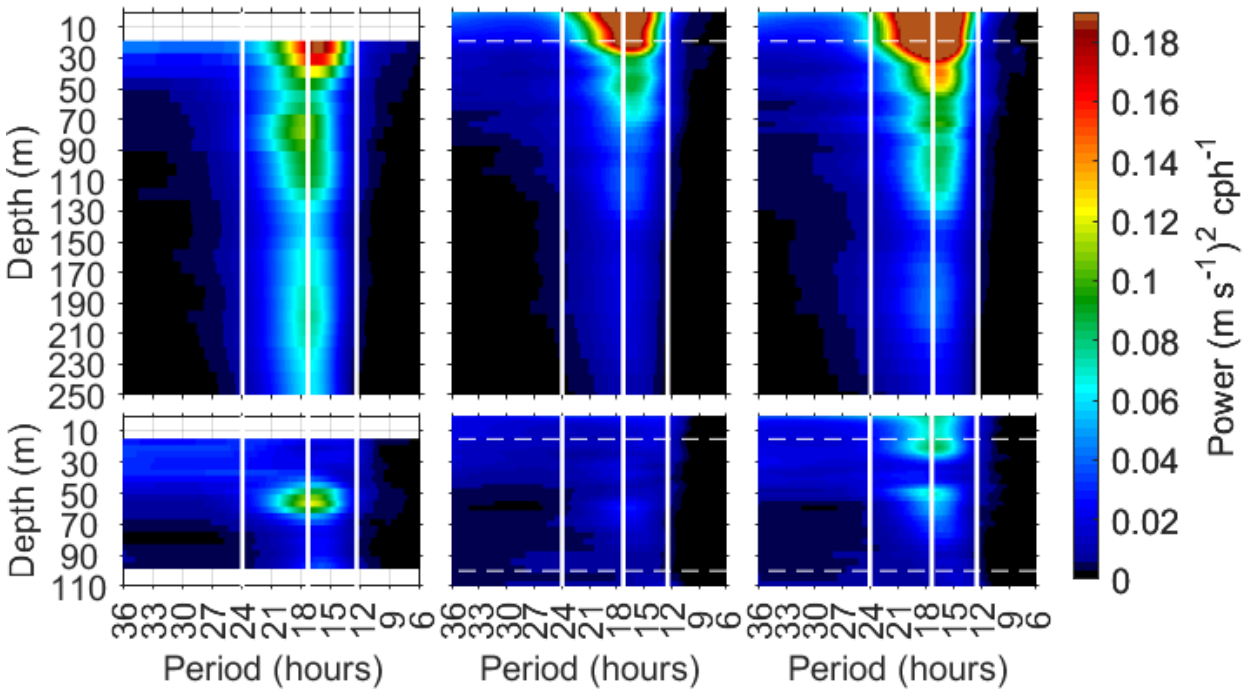

Figure 3: Rotary spectra of the observed currents (left), spectra simulated with the original ECMWF data (centre), and spectra simulated by doubling the two wind peaks before the NIWs main event (right) at the deep (top) and near-coastal (bottom) mooring. Spectra are calculated for the LOGMEC17 data collection period (13/Sep-14/Nov for the deep mooring and 27/Sep-25/Oct for the near-coastal mooring). Vertical white lines represent the diurnal tidal period, the inertial period (17.3h), and the semidiurnal tidal period. Horizontal dashed lines indicate the depth range where observations are available.

Using the original ECMWF wind data (Figure 3, central panels), the NIWs energy at the two moorings is underestimated compared to the observed one (Figure 3, left panels). By doubling the two wind peaks, the NIW energy simulated by the LISM (Figure 3, right panels) is closer to the observations. From now on, only the results of the LISM simulations performed by doubling the two wind peaks (as shown in Figure 2) will be considered. Overall, the LISM reproduces the NIWs as dominant high-frequency processes (from 6 to 36 hours) in agreement with the observations. The comparison shows good agreements in both amplitude and frequency band of the observed and simulated NIWs. At the near-coastal mooring, the simulated NIW energy is confined to intermediate layers, comparable to what was observed but somewhat weaker, and a

power peak appears in the surface layers down to 30 m depth that was not observed. Despite the overall good agreement with observations, the simulated NIWs energy below 50 m depth at both moorings is lower than that observed. To better investigate the difference between observed and simulated NIWs energy, we identify the most energetic NIWs during LOGMEC17 and focus the analysis on a selected period. The time series of inertial energy for the entire four months of LISM simulation, averaged over the studied area at selected depths (Figure 4), was calculated. The most energetic NIWs occur from 07 to 17 October, generated by the strong wind peaks at 21:00 on 06 October and 03:00 on 08 October, reaching 0.30 N m^{-2} and 0.22 N m^{-2}, respectively.

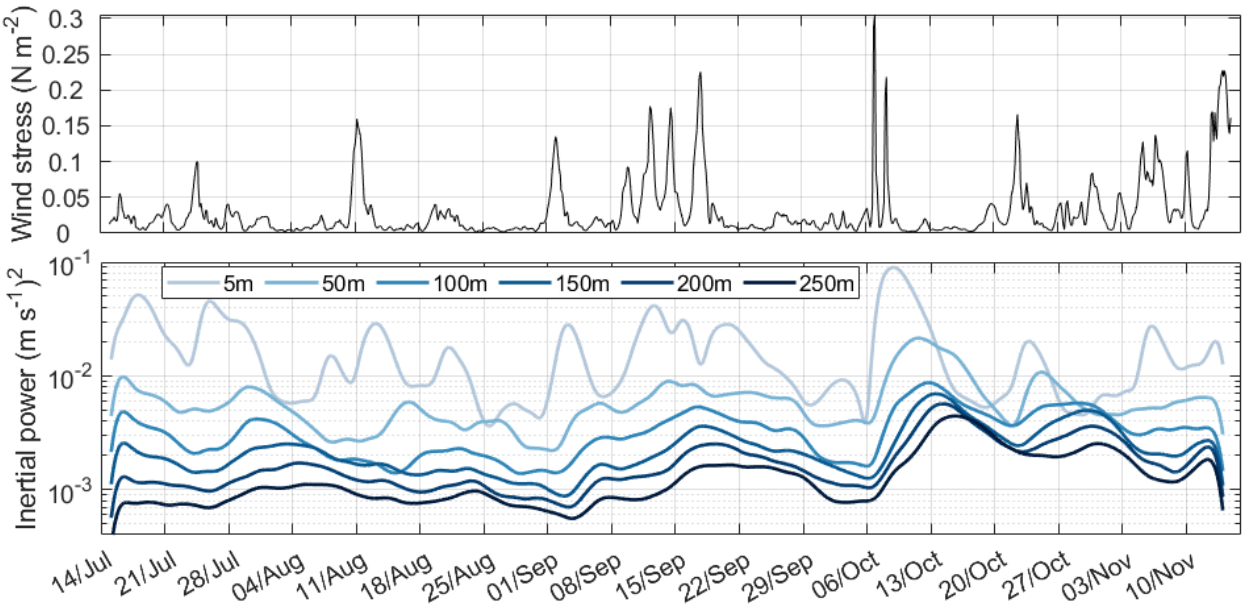

Figure 4:Time series of wind stress (top) and inertial energy (bottom) at 5, 50, 100, 150, 200, and 250 m depth throughout the LISM simulation. The first and last 36 hours are not reliable because they are outside the influence cone of the wavelet.

Figure 4 shows a clear relationship between wind stress peaks and inertial peaks, indicating that NIW are generated by wind. The inertial energy time series clearly shows a time shift in power peaks with increasing depth, indicating a predominantly downward energy propagation of the NIWs, consistent with observations.

From now on, the analysis will focus on the most energetic NIWs from 07 to 17 October. The vertical group velocity of the NIWs during the selected period is estimated as follows:

$$C_{gz} = \frac{\Delta z}{\Delta t}$$

where Δz is the depth difference at which the power peaks occur and Δt is the time difference between the two power peaks. The estimated mean vertical group velocity of NIWs from 07 to 17 October between 5 and 250 m depth is $4.2 \cdot 10^{-4}$ m s^{-1}, almost twice the observed mean group velocity ($2.6 \cdot 10^{-4}$ m s^{-1}) of NIWs (Cozzani *et al*., to be submitted).

Rotary spectra of the observed and simulated currents at the two moorings during the most energetic NIW period were performed (Figure 5).

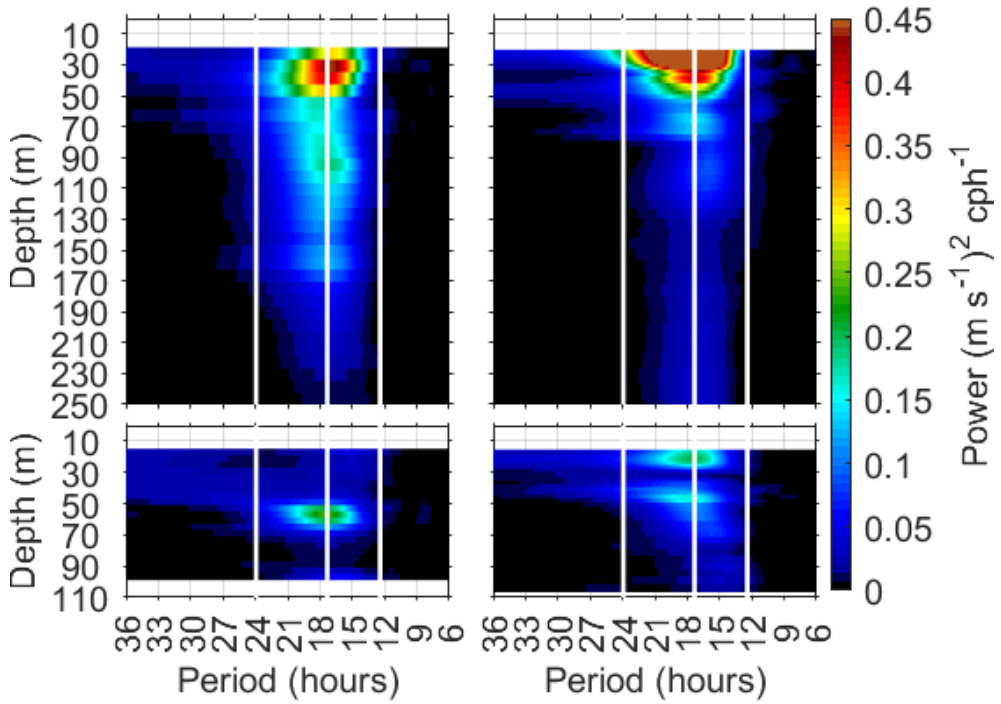

Figure 5: Same as Figure 3 but for observations (left) and LISM (right) during the most energetic NIWs period, from 07 17 October. The upper colorbar limit is higher compared to Figure 3 to highlight the power peaks.

At the deep mooring, the NIW energy in the surface layers is stronger than the observed one, while it is comparable between 30 and 50 m depth. According to the spectra for the entire LOGMEC17 period (Figure 3), the simulated NIWs energy for the selected period (Figure 5) is lower than the observed power below 50 m depth. At the near-coastal mooring, the simulated power peak occurs at about 45 m depth, which is closer to the surface compared to the observations.

To explain the difference between observed and simulated NIWs below 50 m depth, we first ruled out the hypothesis that the vertical resolution of the LISM is low. Sensitivity tests on the vertical resolution (not shown) indicated that it is not a limiting factor for NIWs vertical propagation of the NIW. In fact, the LISM has 77 vertical levels in the first 250 m, which is much higher than previous studies of NIW modelling (Raja *et al*., 2022).

The vertical propagation of NIWs could be affected by their interaction with mesoscale structures, which can change the properties of NIWs and drain the energy downward (Kunze 1985; Young and Ben Jelloul 1997; Whitt and Thomas 2013; Danioux *et al.* 2015; Wagner and Young 2016), but reproducing the intensity and location of small-scale structures is a difficult task in ocean modelling. Nevertheless, a good model would be able to reproduce the mesoscale

statistics, so we expect the dynamics observed at the two moorings to evolve in other regions of the domain. In the next sections, we will examine the model results for the entire domain.

5.3.2 Spatial distribution of wind-generated NIWs

We now examine the generation range of the most energetic NIWs. The first step is to calculate the wind kinetic energy transfer as a product of wind stress and relative ocean current. During the two wind peaks before the NIWs event, the kinetic energy transfer is stronger in the northwestern part of the area, but the spatial distribution on 06 October at 21:00 and on 08 October at 03:00 is different (Figure 6).

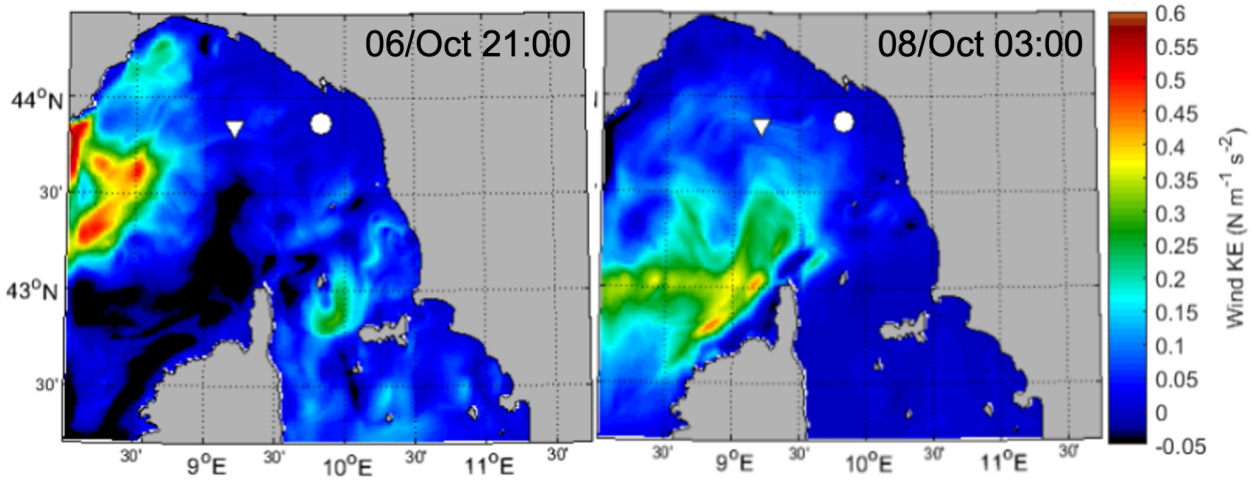

Figure 6: Wind kinetic energy transfer during the two wind peaks before the main NIWs event.

On 06 October at 21:00, the strongest kinetic energy transfer occurs at a latitude above 43°N and a longitude below 9°E, while on 08 October at 03:00 this area is characterised by low energy and the strong kinetic energy transfer occurs northwest of Corsica at a latitude below 43.5°N. Considering the spatial distribution and knowing that the wind is the main generation mechanism of the NIWs, we can hypothesise that the NIWs are generated by the wind in the northwestern region of the area. To confirm this hypothesis, spectral analysis was applied to the currents simulated from 07 to 17 October at selected depths. The averaged energy within the near-inertial frequency band, also called near-inertial energy (Figure 7a), shows that the maximum of near-inertial energy occurs in the surface layer (43.3°N; 8.7°E), confirming that the northwestern region is the generating region of the NIWs.

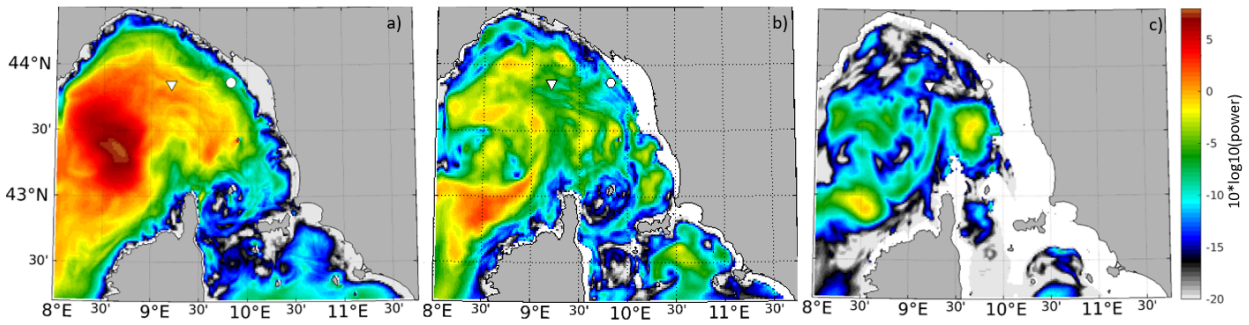

Figure 7: Near-inertial energy ([m s^{-1}]^2 cph^{-1}) at 5 (a), 50 (b), and 150 (c) metres depth.

From the surface (Figure 7a), inertial energy propagates downward and horizontally in all directions, with a significant portion of the energy flowing southward (from 42.8 to 43.1°N) at 50 m depth (Figure 7b).

The eastern part of the area is characterised by low inertial energy, due to the weak kinetic energy transfer in this area (Figure 6), and no NIWs are evident, especially around the Capraia island (43.1°N; 9.8°E) and southwest of the Elba island (42.7°N; 10.3°E). Towards the seafloor, at a depth of 150 m (Figure 7c), two regions can be identified north and northwest of Corsica island where inertial energy is trapped.

5.3.3 Variability of relative vorticity

During the most energetic NIWs period, from 07 to 17 October, the averaged vertical vorticity at 50 and 150 m depth (Figure 8) shows strong mesoscale activity.

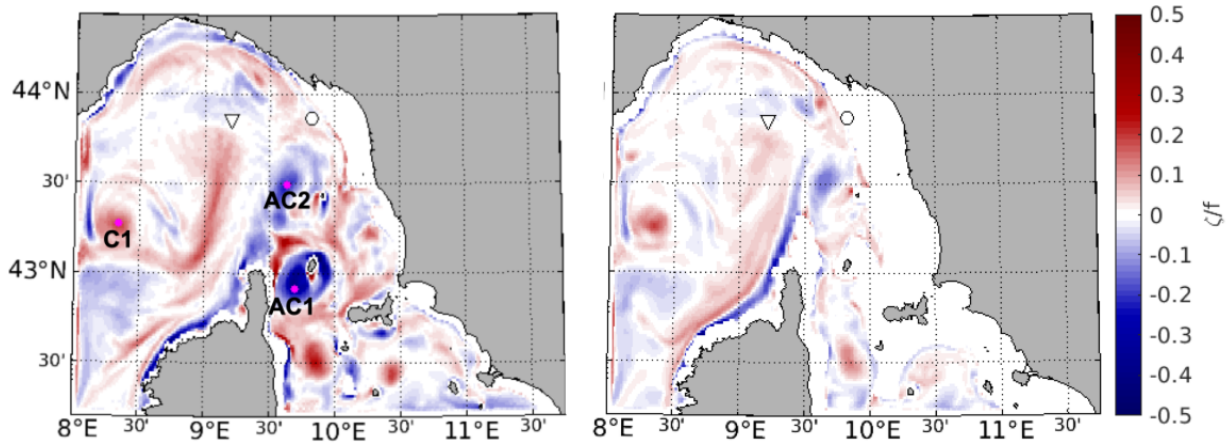

Figure 8: Vorticity field normalised by the local inertial frequency f at 50 m (left) and 150 m depth (right). The white triangle and dot indicate the deep and near-coastal mooring respectively.

The LISM simulates some mesoscale structures consistent with the literature, such as the cyclonic circulation in the western part of the area and the anticyclone around the Capraia island

(Poulain *et al*., 2012; Pinardi *et al.*, 2015) as well as other features that have never been observed but seem realistic. The anticyclone northeast of Corsica island was also observed by satellite (not shown).

The vorticity normalised by the inertial frequency provides an estimate of the local Rossby number, which reaches 0.42 at 50 m depth near Capraia island. The Rossby number quantifies the nonlinearity of the flow, and for small Rossby numbers the quasi-geostrophic approximation is valid and inertial forces are dominant.

At 50 m depth, the strongest anticyclone is clearly identified around the Capraia island (AC1). Another strong anticyclone (AC2) is located south of the two moorings and a cyclone (C1) is located near the western boundary of the area. The deep mooring is located between areas of negative vorticity (north) and positive vorticity (south). A clear change in the sign of the vorticity is also evident near the western boundary around 43°N.

At 150 m depth, AC1 is not present, but overall the mesoscale structures are similar but weaker than at 50 m depth. At 150 m depth, regions of negative vorticity can be identified to the north (AC2) and northeast of Corsica island (south of C1), corresponding to areas where NIWs energy is trapped (Figure 7c). This suggests that negative vorticity is responsible to drain the NIWs energy toward the seafloor, which is consistent with previous studies (Lee and Niiler 1998; Zhai et al. 2005; Danioux et al. 2008).

In the following, we will focus on the interaction between the identified strong mesoscale structures and the NIWs to investigate how this interaction changes the properties of the NIWs.

5.3.4 Influence of mesoscale eddies on NIWs

Frequency shift

The NIWs period determined from spectral analysis at 50 and 150 m depth (Figure 9, left panels) changes significantly in the LISM domain, reaching a 10% shift with respect to the local inertial period.

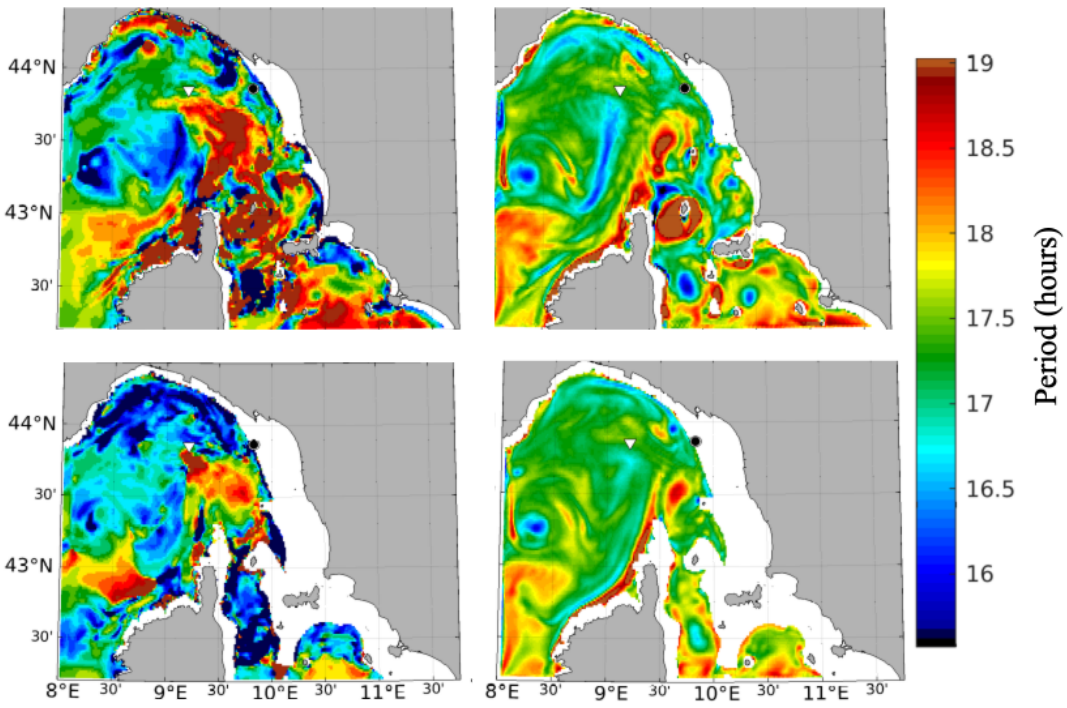

Figure 9: NIWs period from spectral analysis (left) and effective NIWs period (right) at 50m (top) and 150m depth (bottom). The green colour denotes the inertial period (17.3h).

At 50 m depth, the so-called blueshift (frequency higher / period lower than the inertial period) occurs mainly in the northwestern part of the studied area, while the southern and eastern area are characterised by NIWs with a period higher than the local inertial period. At 150 m depth, the spatial variability of the NIWs period is comparable to that at 50 m depth, but north of the two moorings and west of Corsica island the period is lower.

To understand how mesoscale and submesoscale structures affect the NIWs frequency shift, the NIWs period obtained from spectral analysis is compared with the effective NIWs period at 50 and 150 m depth (Figure 9).

In the western part of the area, spectral analysis shows that the NIWs period is shifted to periods lower than that of the inertial period, which is consistent with the effective NIWs period due to cyclonic circulation. Indeed, at both depths, the lower period is located at the centre of cyclone C1. Similarly, the effective NIWs period at 50 m depth is shifted toward higher periods within anticyclones AC1 and AC2, which is consistent with the spectral analysis.

The good agreement between the NIWs period from spectral analysis and the effective NIWs period indicates that the main responsible for the NIWs frequency shift is the wave interaction with mesoscale features.

Vertical propagation

In the following, we examine how the strong anticyclones (AC1, AC2) and the cyclone (C1) affect the propagation of NIW along the water column (Figure 10).

The penetration depth of the mesoscale structures is not proportional to their horizontal extent, contrary to what Lapeyre (2017) simulated.

The horizontal scale of anticyclone AC1 is about 50 km (Figure 5) and extends from the surface to 85 m depth ($\frac{\zeta}{f}$>0.1), whereas anticyclone AC2 is smaller than AC1, has almost half the horizontal scale, but extends to 210 m depth ($\frac{\zeta}{f}$>0.1) and disappears at 350 m depth. The horizontal scale of cyclone C1 is comparable to that of AC2 and extends to a depth of 2550 m (not shown).

To investigate the energy propagation of NIWs within the identified mesoscale structures, the rotary spectra from 07 to 17 October at the centre of AC1, AC2, and C1 are calculated and the normalised vorticity is averaged over the selected period.

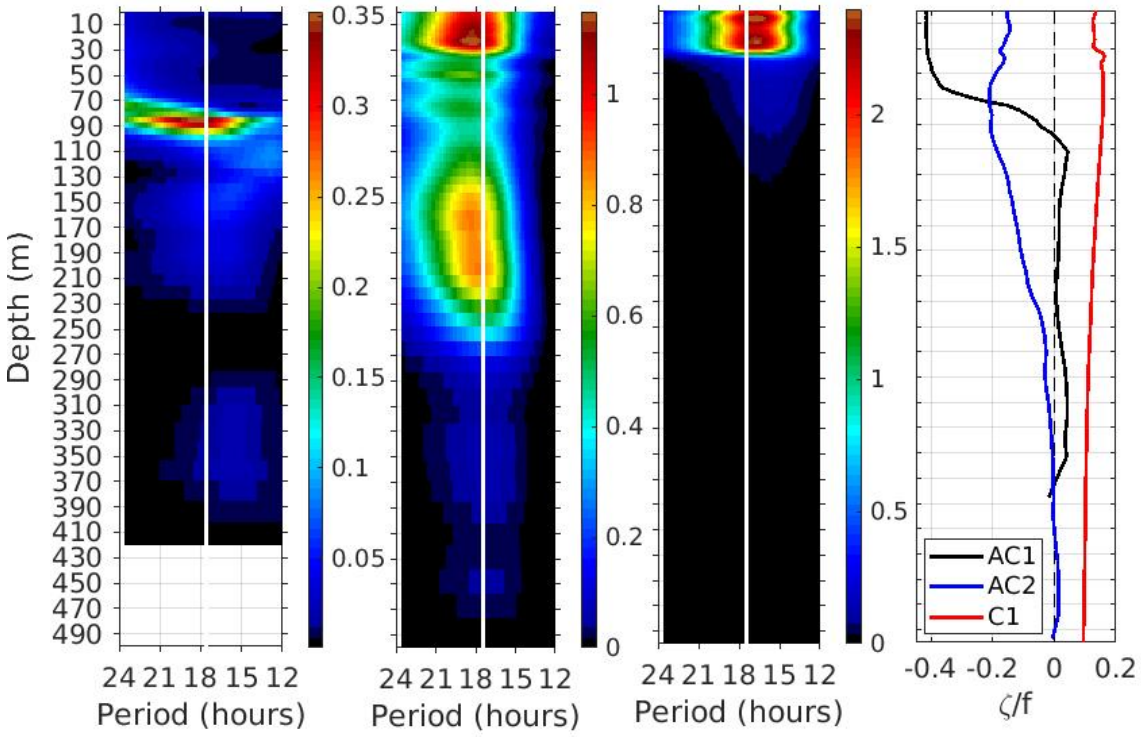

Figure 10: From left to right: rotary spectra at anticyclones AC1, AC2, cyclone C1 and their normalised vorticity profile from 07 to 17 October.

Anticyclone AC1 is characterised by a strong normalised vorticity (-0.42) from the surface to 50 m depth, which then decreases sharply and disappears at about 100 m depth, while within

anticyclone AC2 the maximum vorticity (-0.2) is found between 60 and 90 m depth and gradually decreases and disappears at about 350 m depth. Cyclone C1 is more evenly distributed throughout the water column, reaching a maximum value of 0.18 at 50 m depth, decreasing slightly and maintaining a normalised vorticity value above 0.1 until 500 m depth.

There is no NIWs signal within AC1, but NIWs are present below the anticyclone in a confined layer from 85 to 100 m depth, assuming a power of 0.35 $(m\ s^{-1})^2 cph^{-1}$.

Previous studies have shown that anticyclones can act as waveguides that drain the NIWs energy downward into the deep ocean (Lee and Niiler 1998; Zhai *et al.* 2005; Danioux *et al*. 2008; Lelong *et al*., 2020), and in other cases NIW could be trapped only at the base of the anticyclone (Kunze *et al*. 1995; Joyce *et al.* 2013; Lelong *et al*., 2020), but in the present study the NIWs are concentrated below anticyclone AC1 and we will investigate further in the next sections.

Within the anticyclone AC2, the NIWs are trapped and propagate downward into the deep ocean, this is the so-called "inertial chimney effect". In particular, the energy of the NIWs is trapped within anticyclone AC2 and weakens around 250 m depth, where the vorticity is close to zero. Two power peaks occur around 25 m depth and from 150 to 210 m depth, reaching energies of 1.15 and 0.85 $(m\ s^{-1})^2 cph^{-1}$, respectively.

The vertical propagation of NIWs is also studied within cyclone C1 at the western boundary of the domain. The strongest normalised vorticity (0.18) occurs at about 35 m depth, which corresponds to the layer where the NIWs energy sharply decreases, suggesting that the cyclone dampens the NIWs vertical propagation. In the surface layers, two power peaks occur at 5 and 25 m depth, reaching 2.4 $(m\ s^{-1})^2 cph^{-1}$.

The trapping of NIWs energy in anticyclonic regions and the repulsion of cyclones have been frequently observed (Weller 1985; Kunze 1986; Kunze *et al.,* 1995; Elipot *et al*., 2010).

The NIWs below anticyclone AC1 and those inside anticyclone AC2 are characterised by a red shift, while the NIWs frequency at cyclone C1 is blue shifted in agreement with the Kunze (1985) theory.

The time series of inertial energy within the eddies (not shown) confirms the absence of NIWs energy within anticyclone AC1, even before 07 October, indicating that the NIWs below AC1 are not locally generated. Moreover, the inertial power peak below AC1 occurs on 10 October and, assuming that the NIW is generated by the wind event on 06 October at 21:00, the estimated vertical group velocity is $2.6 \cdot 10^{-4}$ m s^{-1}, while the estimated vertical group velocity within anticyclone AC2 is $4.8 \cdot 10^{-4}$ m s^{-1}. The magnitude of the estimated vertical group velocity is consistent with the downward NIWs observed during LOGMEC17 ($(2.2 \pm 0.3) \cdot 10^{-4}$ m s^{-1}) (Cozzani *et al.*, to be submitted).

Transects

To understand how the NIW propagates within the domain, vertical sections of vorticity and NIWs energy were analysed (Figure 11). In particular, we will examine the special case of AC1, focusing on the origin of the NIWs energy detected below AC1.

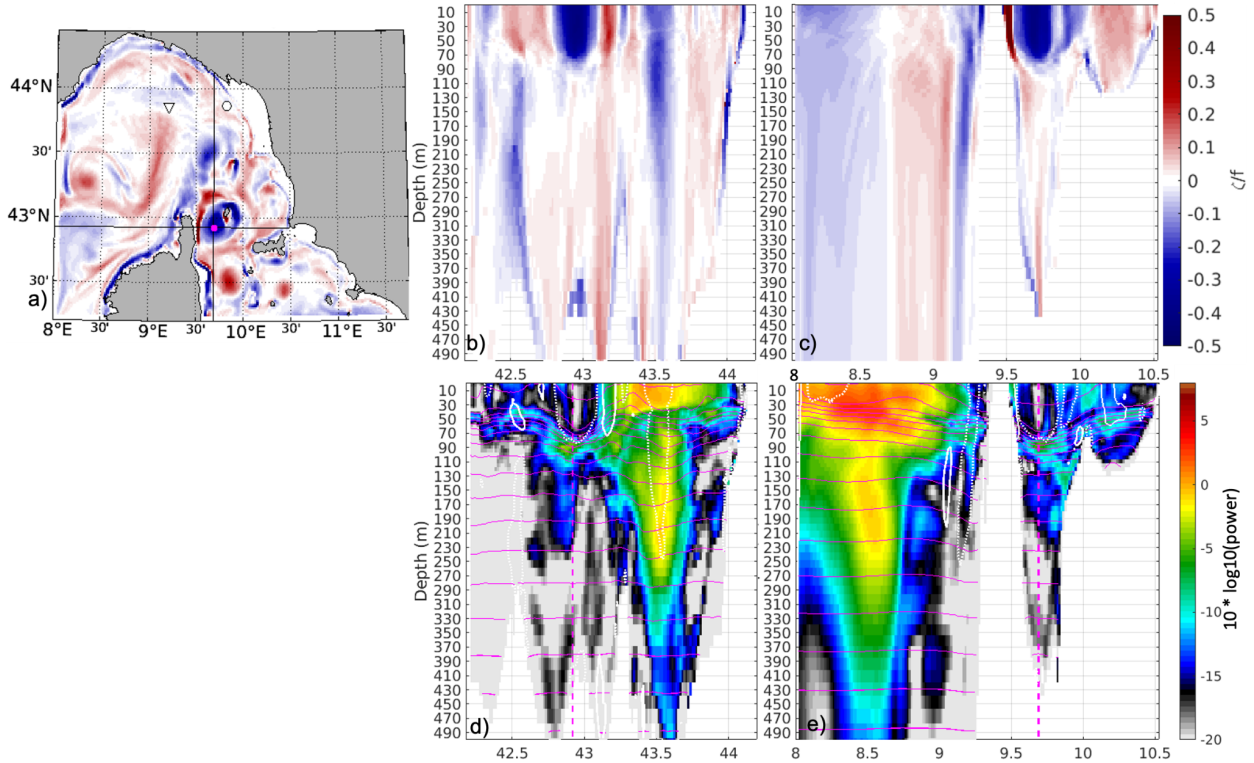

Figure 11: (a) Horizontal section of normalised vorticity at 50 m depth, averaged from 07 to 17 October with vertical and horizontal black lines representing the location of the zonal and meridional transect passing through anticyclone AC1 indicated by the magenta dot; normalised vorticity (b,c) and near-inertial energy (d,e) in ([m s^{-1}]^2 cph^{-1}) along the meridional and zonal transects, respectively. The vertical dashed magenta line represents the location of AC1 along the transects, and the thin magenta lines denote the isopycnals (contour interval of 0.25 Kg m^{-3} between 27 and 31.25 Kg m^{-3}). The white solid and dotted lines represent the normalised vorticity of 0.1 and -0.1, respectively.

The zonal and meridional transects passing through AC1 confirm that NIW energy does not penetrate anticyclone AC1. The small amount of energy near the boundary of the anticyclone is justifiable because the anticyclone moves horizontally during the selected period (07-17 October); the lowest energy is found in the centre of AC1, where the vorticity remains strong throughout the period. AC1 is surrounded by positive vorticity where the NIWs energy is present, although the energy is weak due to the low wind kinetic energy transfer in this area (Figure 6).

The meridional transect (Figure 11b,d) shows high NIWs energy trapped in anticyclone AC2 (43.5°N), and southward the energy decreases sharply as it encounters anticyclone AC1. In the surface layers, the slanted isopycnals around 43.2°N (Figure 11d) that characterise the

anticyclone can be considered as front. In fronts, the NIWs with effective inertial frequency can undergo critical reflections that dissipate energy (Thomas, 2017). The four possible directions of NIWs energy propagation are symmetric about the isopycnal slope. This atypical wave physics can facilitate energy transfers between NIWs, inertial-gravity waves of different frequencies, and balanced flow. Critical reflection reduces the vertical scale of NIWs and promotes viscous dissipation.

In summary, in the surface layers, part of the near-inertial energy coming from the north flows around the AC1 anticyclone (Figure 7 and Figure 11d,e) and part is dissipated at the front formed by the anticyclone. At deeper depths, the energy follows isopycnals passing below AC1, where the Brunt-Vaisala frequency is high (not shown), and tends to rise to the surface south of AC1. NIW propagating along the isopycnals reach the minimum frequency above which propagation is possible (Thomas, 2017).

The zonal transect (Figure 11c,e) shows the strongest NIWs energy in the western part of the domain, near the NIWs generation area, where the negative vorticity acts as a waveguide that traps the NIWs energy downward into the deep ocean, while east of Corsica the NIWs energy tends to follow the isopycnals and the lowest values are found inside AC1.

5.4 Discussion and conclusions

Motivated by strong NIWs observed with two moorings during the LOGMEC17 campaign in the Ligurian Sea (Cozzani *et al*., to be submitted), the present study investigates the interaction between NIWs and mesoscale structures using a dedicated numerical model, the Ligurian Sea Model (LISM). The implemented numerical model is based on NEMO (Madec *et al*., 2019), the parent domain has a horizontal resolution of about 1300 m and a two-way nested child model reaches 400 m near the two moorings of the LOGMEC17 experiment. The vertical grid is discretized by 141 unevenly spaced levels with partial steps (Barnier *et al*., 2006). Atmospheric fields are provided by ECMWF, but two wind peaks are doubled based on comparison with scatterometer data and a previous study in the area (Bozzano *et al*., 2004) that showed an underestimation of wind peaks from ECMWF data. The parent model is initialised and one-way nested (Oddo and Pinardi 2008) with the Copernicus Mediterranean Sea operational model (Oddo *et al*., 2014).

The LISM reproduces the NIWs as dominant high-frequency processes (period < 36h) in the Ligurian Sea, in agreement with the observations (Figure 3). Despite the overall good agreement with the observations, the simulated NIWs energy is weaker at the two mooring locations below 50 m depth. Differences between simulations and observations are likely due to the difficult task of reproducing the real location of mesoscale and submesoscale structures in ocean modeling. In fact, these structures strongly interact with NIWs. Anticyclone can act as waveguides that trap NIW energy downward along the water column, while the cyclone dampens NIW energy (Lee

and Niiler 1998; Danioux *et al*. 2008; Joyce *et al.* 2013; Asselin and Young 2019). Nevertheless, the LISM is capable of reproducing the known structures in the Ligurian Sea and other features that have never been observed but appear realistic. Therefore, the interaction between NIW and the mesoscale features over the whole area during the most energetic NIWs period from 07 to 17 October is studied. The vorticity field shows strong mesoscale activity consistent with previous studies (Crépon *et al.*, 1982, Flexas *et al.*, 2005; Casella *et al.*, 2014, Borrione *et al*., 2016). The comparison between the NIWs period obtained from spectral analysis and the effective NIWs period (Kunze, 1985) shows that the interaction of NIWs with mesoscale features is the main factor for the shift in wave frequency (Figure 9).

The most energetic NIWs are wind-generated in the northwestern part of the domain and their frequency changes over the studied area. According to the theory of Kunze (1985), anticyclones (cyclones) shift the NIWs frequency to lower (higher) frequencies. An anticyclone characterised by a negative normalised vorticity between 0.1 and 0.2 from the surface to 200 m depth traps the NIWs energy and facilitates its downward propagation, while a cyclone with a positive vorticity between 0.1 and 0.2 from the surface to 500 m depth dampens the NIWs energy, consistent with previous studies. A particular case shows the absence of NIWs energy within an anticyclone (AC1). This anticyclone is characterised by a strong normalised vorticity $\left(\frac{\zeta}{f} = -\ 0.42\right)$ from the surface to 50 m depth (Figure 10), while the vorticity decreases sharply below this depth and vanishes at about 100 m depth. In the surface layers, the absence of inertial energy suggests that the NIWs are not generated locally at AC1. Analysing the zonal and meridional transect passing through AC1 (Figure 11), it can be argued that some of the NIWs energy coming from the north of the anticyclone is diverted around it, while some of the energy could be dissipated according to Thomas (2017) as it encounters strongly slanted isopycnals (due to the presence of AC1), which can be considered as a front. At deeper depths, the energy follows isopycnals passing beneath the AC1 and rising to the surface south of the anticyclone. According to Thomas (2017), NIW propagating along isopycnals reach their minimum frequency above which propagation is possible.

A second anticyclone (AC2) with a more evenly distributed vorticity along the water column, reaching a maximum normalised vorticity of -0.2 between 60 and 90 m depth, traps the locally wind-generated NIWs and facilitates their downward propagation, which is known as the "inertial chimney effect" (Lee and Niiler 1998).

This study highlights the relevance of downscaling in numerical models, given the importance of mesoscale and submesoscale dynamics in the ocean. Previous studies in this region (Oddo *et al*., 2022) have also shown that downscaling improves model performance.

Combining data collected during a multi-platform, multi-scale and multi-disciplinary campaign such as LOGMEC17 with a dedicated numerical model improves scientific understanding of NIW. Since NIWs play a key role in the energy balance of ocean circulation, this study can form the basis for future developments of numerical ocean models and their products.

How the interaction between NIWs and mesoscale structures affects the large scale through the

inverse energy cascade is still an open question that should be the subject of future research.
In addition, future numerical model simulations could be performed with a non-hydrostatic core to evaluate the improvement in solving sub-mesoscale processes as the non-hydrostatic effects become strong at submesoscales (Mahadevan, 2006; Hamlington *et al.*, 2014).

6. Summary and conclusions

The goal of this work is to better understand small-scale, high-frequency processes in the ocean. *In situ* observations collected during a multi-platform, multi-disciplinary and multi-scale oceanographic campaign (LOGMEC17) in the northwestern Mediterranean Sea in autumn 2017 have shown that Near-Inertial Internal Waves (NIWs) are the dominant high-frequency processes (period < 36 hours). NIWs play a key role in the ocean because they are highly energetic, cause vertical mixing, deepen the mixed layer depth by up to 30%, and can affect climate. Despite the relevance of NIWs, few theoretical, observational, and modelling studies have been published for the Mediterranean Sea. The present study has led to the achievement of the following set of objectives:

1. characterise the studied area at different scales during the LOGMEC17 experiment;
2. study the NIWs generation and their propagation;
3. estimate the NIWs properties such as frequency, wavelength, phase velocity and group velocity;
4. study the NIWs interaction with mesoscale structures.

The large-scale circulation, water masses, and their long- and short-term variability during LOGMEC17 are studied by combining satellite, glider, and mooring data. The results show that the studied area is characterised by strong mesoscale activity, with high variability also observed at the submesoscale (~1 km). In addition, the variability of the main currents affects the water masses entering the experimental area.
During the LOGMEC17 experiment (from September 13 to November 14 2017), two fixed moorings measured water currents allowing the identification of the NIWs signal by applying spectral analysis. The buoy moored at 1000 m depth (deep mooring) observes strong NIWs along the entire sampled water column (from 30 to 250 m depth), while a near-coastal mooring, located near the bathymetric line of 100 m, identifies only one strong NIWs confined from 55 to 63 m depth.
The NIWs near the surface (D1 and D3) are generated by local wind gusts, while those observed at greater depths (D2, D4, D5, and C1) are generated in other regions and arrive at the moorings.

A first wind peak (September 14 at 15:00) generates the D1 event at the deep mooring and also the D2 event in another region. The latter propagates downward with a mean vertical group velocity of $2.6 \cdot 10^{-4}$ m s^{-1} and reaches the mooring 10 days later at 227 m depth. Similarly, events D3, D4 and D5 are triggered by a second wind gust (October 06 at 21:00). The D3 event is generated locally at the deep mooring while D4 and D5 originated far from the mooring and their energy propagates downward with a mean velocity of $1.9 \cdot 10^{-4}$ m s^{-1}.

At the near-coastal mooring, the C1 event is not locally generated and is confined only in intermediate layers, probably due to the presence of the seafloor at 100 m depth.

To the author's knowledge, the observed NIWs are characterised for the first time in the Mediterranean Sea in terms of amplitude, frequency, wavelengths, phase, and group velocity.
The mean amplitude of the observed NIWs is 0.13 m s^{-1}, which is 0.03 m s^{-1} higher than the global average NIW amplitude (Chaigneau *et al*., 2008).
On average, the NIWs energy propagates downward within two constrained bands occurring once every three weeks, with a mean vertical group velocity of (2.2±0.3) $\cdot 10^{-4}$ m s^{-1} (~20 m day^{-1}). Vertical and horizontal group velocities change along the water column and slow down toward the seafloor. Only one NIW (D3b) is characterised by an upward energy propagation along isopycnals.
To complete the characterization of the observed NIWs, the wavelengths are calculated using the dispersion relation (1.3-18). The estimated horizontal and vertical wavelengths at the deep mooring are 43±25 km and 125±35 m, while they are shorter at the near-coastal mooring, 36±2 km and 33±2 m, respectively. The wavelengths at the deep mooring are within the range estimated in the eastern Mediterranean (Cuypers *et al.*, 2012), while the shorter vertical wavelength at the near-coastal mooring is likely due to the presence of the seafloor at 100 m depth.
Consistent with observations in other regions of the world, most of the observed NIWs experience a blue shift, with a frequency higher (up to 9%) than the local inertial frequency, while two NIWs are red-shifted, reaching a frequency 3% lower than the local inertial frequency. The main reason for the frequency shift of the NIW is the interaction of the waves with the strong mesoscale and submesoscale structures in the region.
To complement the *in-situ* observations, a numerical model is implemented using NEMO v4.0.4. The so-called Ligurian Sea Model (LISM) has a horizontal resolution of 1300 m and reaches 400 m in the experimental area, using a two-way nested approach. The vertical grid is discretized with 141 unevenly spaced levels. Atmospheric fields are provided by ECMWF, but comparison with scatterometer data shows that wind gusts are underestimated before the main NIWs event. Based on this comparison, and since wind is the main generation mechanism of NIWs, two wind peaks are doubled in intensity. The LISM simulations performed under realistic conditions reproduce the known circulation, some known strong structures in the Ligurian Sea and other eddies that have never been observed but appear realistic.
The model reproduces NIWs as dominant high-frequency processes during the LOGMEC17 campaign, in agreement with observations. The interaction of NIWs with eddies is studied over the domain during the most energetic NIWs event (from October 07 to 17).
The NIWs are generated by winds in the northwestern part of the area, and their frequency is modified according to the theory of Kunze (1985), i.e., the anticyclone (cyclone) shifts the NIWs frequency to lower (higher) frequencies. An anticyclone with a negative normalised vorticity in the range of 0.1 to 0.2 acts as a waveguide for the NIWs energy and facilitates downward propagation, while a cyclone, with a positive normalised vorticity of the same order of magnitude of the anticyclone, dampens the energy according to previous studies. Conversely, NIW energy is not present within a strong anticyclone (AC1). The latter is characterised by a

strong normalised vorticity $\left(\frac{\zeta}{f} = -0.42\right)$ from the surface to 50 m depth, while the vorticity decreases sharply below this depth. We argue that in the surface layers some of the NIW energy coming from the north of anticyclone AC1 is diverted around it, while some of the energy could be dissipated as it encounters strongly slanted isopycnals, according to Thomas (2017).
The energy at greater depths follows the isopycnals passing beneath the anticyclone and rising to the surface farther south.
A second anticyclone (AC2) with a more evenly distributed vorticity along the water column (reaching $\frac{\zeta}{f} = -0.2$ from 60 to 90 m depth) traps the locally wind-generated NIWs and facilitates their downward propagation, which is the so-called "inertial chimney effect" (Lee and Niiler 1998).

The observations and simulations in this work show that NIW energy is present throughout the water column, confirming that these waves contribute to both surface and deep water mixing. Mixing plays an important role in regulating the mean state of the ocean and its response to climate change (Melet *et al.*, 2022), so better knowledge of NIWs is relevant.

Since wind plays an important role in wave generation, future oceanographic campaigns to study NIWs should be designed to collect wind data with high temporal resolution. Thus, moorings should be equipped with meteorological stations to reduce uncertainties in wind strength when studying NIW generation.

This study also shows that combining *in situ* observations with an appropriate numerical model significantly improves the understanding of NIWs. As pointed out by Alford and coauthors (2016), the study of NIWs is challenging because it requires synoptic sampling with very high temporal and spatial resolution. Collecting high-resolution *in situ* observations over a long period of time is difficult and costly: moorings are sparse and fixed, gliders are slow and collect data on a zigzag trajectory, ships collect data in a limited area and for a limited period of time, satellites measure only the ocean surface, and horizontal resolution is insufficient to detect submesoscale structures. For this reason, although LOGMEC17 is a multi-platform and multi-scale campaign, modelling support plays a key role in investigating the NIWs. The methodology used in this work can be applied to other regions to gain a better understanding of these waves in the world.

The present study also highlights the crucial role of mesoscale and submesoscale structures in the ocean, which should be considered in future research. Indeed, downscaling in numerical ocean models is becoming increasingly important to improve model performance, as previous studies have shown (Bendoni *et al*., 2022; Oddo *et al.*, 2022).
In addition, future numerical model simulations could be performed with a non-hydrostatic core to evaluate the improvement in solving sub-mesoscale processes as the non-hydrostatic effects become strong at submesoscales (Mahadevan, 2006; Hamlington *et al.*, 2014).

Other future directions could address the inverse energy cascade to understand how the interaction of NIW with mesoscale structures affects large-scale processes, since energy balance is one of the most important issues in oceanography.

In order to combine the model with *in situ* observations, further future research could use data assimilation methodology, which is an increasingly important tool for understanding ocean dynamics. Although small-scale, high-frequency data assimilation techniques are challenging, they could become very important. They add value to observations, fill in the spatiotemporal gaps, and support the model by constraining it with *in situ* measurements (Lahoz and Schneider, 2014).

Since NIWs play a critical role in the ocean energy cascade and can influence climate (Jochum *et al.*, 2013), this study can provide the basis for future developments in numerical ocean models and their products.

References

Acoustic Doppler Current Profiler Principles of Operation A Practical Primer. (2011). http://www.rdinstruments.com

Adcroft, A., & Campin, J.-M. (2004). Rescaled height coordinates for accurate representation of free-surface flows in ocean circulation models. *Ocean Modelling*, *7*(3), 269–284. https://doi.org/https://doi.org/10.1016/j.ocemod.2003.09.003

Albérola, C., Millot, C., & Font, J. (1995). On the seasonal and mesoscale variabilities of the Northern Current during the PRIMO-0 experiment in the western Mediterranean Sea. *Oceanologica Acta*, *18*(2), 163–192. https://archimer.ifremer.fr/doc/00096/20770/

Alford, M. H. (2003). Redistribution of energy available for ocean mixing by long-range propagation of internal waves. *Nature*, *423*(6936), 159–162. https://doi.org/10.1038/nature01628

Alford, M. H. (2020). Revisiting near-inertial wind work: Slab models, relative stress, and mixed layer deepening. *Journal of Physical Oceanography*, *50*(11), 3141–3156. https://doi.org/10.1175/JPO-D-20-0105.1

Alford, M. H., & Gregg, M. C. (2001). Near-inertial mixing: Modulation of shear, strain and microstructure at low latitude. *Journal of Geophysical Research: Oceans*, *106*(C8), 16947–16968. https://doi.org/10.1029/2000jc000370

Alford, M. H., MacKinnon, J. A., Simmons, H. L., & Nash, J. D. (2016). Near-Inertial Internal Gravity Waves in the Ocean. *Annual Review of Marine Science*. https://doi.org/10.1146/annurev-marine-010814-015746

Alford, M. h., Shcherbina, A. Y., & Gregg, M. C. (2013). Observations of Near-Inertial Internal Gravity Waves Radiating from a Frontal Jet. *Journal of Physical Oceanography*, *43*(6), 1209–1224. https://doi.org/10.1175/JPO-D-12-0146.1

Aracri, S., Borghini, M., Canesso, D., Chiggiato, J., Durante, S., Schroeder, K., Sparnocchia, S., Vetrano, A., Honda, T., Kitawaza, Y., Kawahara, H., & Nakamura, T. (2016). Trials of an autonomous profiling buoy system. *Journal of Operational Oceanography*. https://doi.org/10.1080/1755876X.2015.1115631

Asselin, O., & Young, W. R. (2020). Penetration of wind-generated near-inertial waves into a turbulent ocean. *Journal of Physical Oceanography*, *50*(6), 1699–1716. https://doi.org/10.1175/JPO-D-19-0319.1

Astraldi, M., & Gasparini, G. P. (1992). The seasonal characteristics of the circulation in the north Mediterranean basin and their relationship with the atmospheric-climatic conditions. *Journal of Geophysical Research: Oceans*, *97*(C6), 9531–9540. https://doi.org/https://doi.org/10.1029/92JC00114

Ayoub, N., Le Traon, P.-Y., & De Mey, P. (1998). A description of the Mediterranean surface variable circulation from combined ERS-1 and TOPEX/POSEIDON altimetric data. *Journal of Marine Systems*, *18*(1), 3–40. https://doi.org/https://doi.org/10.1016/S0924-7963(98)80004-3

Bendoni, M., Fattorini, M., Taddei, S., & Brandini, C. (2022). High-resolution downscaling of CMEMS oceanographic reanalysis in the area of the Tuscany Archipelago (Italy). *Ocean Dynamics*, *72*(5), 295–312. https://doi.org/10.1007/s10236-022-01501-3

Barnier, B., Madec, G., Penduff, T., Molines, J. M., Tréguier, A. M., Sommer, J. Le, Beckmann, A., Biastoch, A., Böning, C. W., Dengg, J., Derval, C., Durand, E., Gulev, S. K., Rémy, E., Talandier, C., Theetten, S., Maltrud, M. E., McClean, J. L., & de Cuevas, B. A. (2009). Impact of partial steps and momentum advection schemes in a global ocean circulation model at eddy-permitting resolution. *Ocean Dynamics*, *59*, 537.

Berman, T., Paldor, N., & Brenner, S. (2000). Simulation of wind-driven circulation in the Gulf of Elat (Aqaba). *Journal of Marine Systems*, *26*(3–4), 349–365. https://doi.org/10.1016/S0924-7963(00)00045-2

Bethoux, J. P., Gentili, B., Morin, P., Nicolas, E., Pierre, C., & Ruiz-Pino, D. (1999). The Mediterranean Sea: A miniature ocean for climatic and environmental studies and a key for the climatic functioning of the North Atlantic. *Progress in Oceanography*, *44*(1–3), 131–146. https://doi.org/10.1016/S0079-6611(99)00023-3

Beuvier, J., Béranger, K., Lebeaupin Brossier, C., Somot, S., Sevault, F., Drillet, Y., Bourdallé-Badie, R., Ferry, N., & Lyard, F. (2012). Spreading of the Western Mediterranean Deep Water after winter 2005: Time scales and deep cyclone transport. *Journal of Geophysical Research: Oceans*, *117*(C7). https://doi.org/https://doi.org/10.1029/2011JC007679

Bindoff, N.L., W.W.L. Cheung, J.G. Kairo, J. Arístegui, V.A. Guinder, R. Hallberg, N. Hilmi, N. Jiao, M.S. Karim, L. Levin, S. O'Donoghue, S.R. Purca Cuicapusa, B. Rinkevich, T. Suga, A. Tagliabue, and P. Williamson, 2019: Changing Ocean, Marine Ecosystems, and Dependent Communities. In: IPCC Special Report on the Ocean and Cryosphere in a Changing Climate [H.-O. Pörtner, D.C. Roberts, V. Masson-Delmotte, P. Zhai, M. Tignor, E. Poloczanska, K. Mintenbeck, A. Alegría, M. Nicolai, A. Okem,

J. Petzold, B. Rama, N.M. Weyer (eds.)]. Cambridge University Press, Cambridge, UK and New York, NY, USA, pp. 447-587. https://doi.org/10.1017/9781009157964.007.

Birol, F., Cancet, M., & Estournel, C. (2010). Aspects of the seasonal variability of the Northern Current (NW Mediterranean Sea) observed by altimetry. *Journal of Marine Systems*, *81*(4), 297–311. https://doi.org/10.1016/j.jmarsys.2010.01.005

Borrione, I., Falchetti, S., & Alvarez, A. (2016). Physical and dynamical characteristics of a 300 m-deep anticyclonic eddy in the Ligurian Sea (Northwest Mediterranean Sea): Evidence from a multi-platform sampling strategy. *Deep-Sea Research Part I: Oceanographic Research Papers*, *116*, 145–164. https://doi.org/10.1016/j.dsr.2016.07.013

Borrione, I., Oddo, P., Russo, A., & Coelho, E. (2019). Understanding altimetry signals in the Northeastern Ligurian sea using a multi-platform approach. *Deep-Sea Research Part I: Oceanographic Research Papers*, *145*, 83–96. https://doi.org/10.1016/j.dsr.2019.02.003

Bosse, A., Testor, P., Mortier, L., Prieur, L., Taillandier, V., D'Ortenzio, F., & Coppola, L. (2015). Spreading of Levantine Intermediate Waters by submesoscale coherent vortices in the northwestern Mediterranean Sea as observed with gliders. *Journal of Geophysical Research C: Oceans*, *120*(3), 1599–1622. https://doi.org/10.1002/2014JC010263

Boyer, Tim P.; Garcia, Hernan E.; Locarnini, Ricardo A.; Zweng, Melissa M.; Mishonov, Alexey V.; Reagan, James R.; Weathers, Katharine A.; Baranova, Olga K.; Seidov, Dan; Smolyar, I. V. (2018). *World Ocean Atlas. NOAA National Centers for Environmental Information.*

Bozzano, R., Siccardi, A., Schiano, M. E., Borghini, M., & Castellari, S. (2004). Comparison of ECMWF surface meteorology and buoy observations in the Ligurian Sea. *Annales Geophysicae*, *22*(2), 317–330. https://doi.org/10.5194/angeo-22-317-2004

Bretherton, Francis P.; Daveis, Russ E.; Fandry, C. B. (1976). A technique for objective analysis and design of oceanographic experiments applied to MODE-73. *Deep-Sea Research*, *23*, 559–582. http://www.tandfonline.com/doi/full/10.3810/pgm.2000.5.1.1062

Byun, S. S., Park, J. J., Chang, K. Il, & Schmitt, R. W. (2010). Observation of near-inertial wave reflections within the thermostad layer of an anticyclonic mesoscale eddy. *Geophysical Research Letters*, *37*(1). https://doi.org/10.1029/2009GL041601

Callies, J., & Ferrari, R. (2013). Interpreting Energy and Tracer Spectra of Upper-Ocean Turbulence in the Submesoscale Range (1–200 km). *Journal of Physical Oceanography*, *43*(11), 2456–2474. https://doi.org/10.1175/JPO-D-13-063.1

Casella, E., P.Tepsich, Couvelard, X., Caldeira, R. M. A., & Schroeder, K. (2014). Ecosystem dynamics in the Liguro-Provençal Basin: The role of eddies in the biological production. *Mediterranean Marine Science*, *15*(2), 274–286. https://doi.org/https://doi.org/10.12681/mms.520

Chaigneau, A., Pizarro, O., & Rojas, W. (2008). Global climatology of near-inertial current characteristics from Lagrangian observations. *Geophysical Research Letters*, *35*(L13603,). https://doi.org/https://doi.org/ 10.1029/2008GL034060

Chen, C., Reid, R. O., & Nowlin, W. D. (1996). Near-inertial oscillations over the Texas-Louisiana shelf. *Journal of Geophysical Research C: Oceans*. https://doi.org/10.1029/95JC03395

Conan, P., & Millot, C. (1995). Variability of the Northern Current off Marseilles, western Mediterranean Sea, from February to June 1992. *Oceanologica Acta*, *18*, 193–205.

Crepon, M., Wald, L., & Monget, J. M. (1982). Low-frequency waves in the Ligurian Sea during December 1977. *Journal of Geophysical Research*, *87*(C1), 595–600. https://doi.org/10.1029/JC087iC01p00595

Cruzado, A., Bernardello, R., Ahumada-Sempoal, M. Á., & Bahamon, N. (n.d.). *Modelling the Pelagic Ecosystem Dynamics : The NW Mediterranean*. https://doi.org/10.5772/39267

Cushman-Roisin, B. (1994). *Introduction to Geophysical Fluid Dynamics*.

Cuypers, Y., Bouruet-Aubertot, P., Marec, C., & Fuda, J.-L. (2012). Characterization of turbulence from a fine-scale parameterization and microstructure measurements in the Mediterranean Sea during the BOUM experiment. *Biogeosciences*, *9*(8), 3131–3149. https://doi.org/10.5194/bg-9-3131-2012

D'Asaro, E. A. (1985). The Energy Flux from the Wind to Near-Inertial Motions in the Surface Mixed Layer. *Journal of Physical Oceanography*, *15*, 1043–1059.

D'Asaro E. A., P. H. (1984). A Near-Inertial Internal Wave Spectrum for the Sargasso Sea in Late Summer. *Journal Of Physical Oceanography*, *14*, 489–505.

D'Asaro, E. A., Eriksen, C. C., Levine, M. D., Niller, P., Paulson, C. A., & Van Meurs, P. (1995). Upper-Ocean Inertial Currents Forced by a Strong Storm. Part I: Data and Comparisons with Linear Theory. *Journal of Physical Oceanography*.

D'Ortenzio, F., Iudicone, D., de Boyer Montegut, C., Testor, P., Antoine, D., Marullo, S., Santoleri, R., & Madec, G. (2005). Seasonal variability of the mixed layer depth in the Mediterranean Sea as derived from in situ profiles. *Geophysical Research Letters*, *32*(12), 1–4. https://doi.org/10.1029/2005GL022463

Danioux, E., Klein, P., & Rivièr, P. (2008). Propagation of wind energy in to the deep ocean through a fully turbulent mesoscale eddy field. *Journal of Physical Oceanography*, *38*(10), 2224–2241. https://doi.org/10.1175/2008JPO3821.1

Danioux, E., Vanneste, J., & Bühler, O. (2015). On the concentration of near-inertial waves in anticyclones. *Journal of Fluid Mechanics*, *773*, R2. https://doi.org/DOI: 10.1017/jfm.2015.252

Debreu, L., Vouland, C., & Blayo, E. (2008). AGRIF: Adaptive Grid Refinement in Fortran. *Comput. Geosci.*, *34*(1), 8–13. https://doi.org/10.1016/j.cageo.2007.01.009

Denbo D.W., A. J. S. (1984). Rotary Empirical Orthogonal Function Analysis of Currents near the Oregon Coast. *Journal of Physical Oceanography*.

Echevin, V., Crépon, M., & Mortier, L. (2003). Simulation and analysis of the mesoscale circulation in the northwestern Mediterranean Sea. *Annal. Geophys.*, *21*. https://doi.org/10.5194/angeo-21-281-2003

Edson, J. B., Jampana, V., Weller, R. A., Bigorre, S. P., Plueddemann, A. J., Fairall, C. W., Miller, S. D., Mahrt, L., Vickers, D., & Hersbach, H. (2013). On the Exchange of Momentum over the Open Ocean. *Journal of Physical Oceanography*, *43*(8), 1589–1610. https://doi.org/10.1175/JPO-D-12-0173.1

Elipot, S., Lumpkin, R., & Prieto, G. (2010). Modification of inertial oscillations by the mesoscale eddy field. *Journal of Geophysical Research: Oceans*, *115*(C9). https://doi.org/https://doi.org/10.1029/2009JC005679

Eric, K. (1985). Near-Inertial Wave Propagation in Geostrophic Shear. *Journal of Physical Oceanography*, *15*, 544–565.

Escudier, R., Renault, L., Pascual, A., Brasseur, P., Chelton, D., & Beuvier, J. (2016). Eddy properties in the Western Mediterranean Sea from satellite altimetry and a numerical simulation. *Journal of Geophysical Research: Oceans*, *121*(6), 3990–4006. https://doi.org/https://doi.org/10.1002/2015JC011371

Farge, M. (1992). WAVELET TRANSFORMS AND THEIR APPLICATIONS TO TURBULENCE. *Annual Review of Fluid Mechanics*, *24*(1), 395–458. https://doi.org/10.1146/annurev.fl.24.010192.002143

Fedele, G., Mauri, E., Notarstefano, G., & Poulain, P. M. (2022). Characterization of the Atlantic Water and Levantine Intermediate Water in the Mediterranean Sea using 20 years of Argo data. *Ocean Science*, *18*(1), 129–142. https://doi.org/10.5194/os-18-129-2022

Ferrari, R., & Wunsch, C. (2009). Ocean circulation kinetic energy: Reservoirs, sources, and sinks. *Annual Review of Fluid Mechanics*, *41*, 253–282. https://doi.org/10.1146/annurev.fluid.40.111406.102139

Flather, R. A. (1976). *A tidal model of the north-west European continental shelf*.

Flexas, M. M., Van Heijst, G. J. F., & Trieling, R. R. (2005). The Behavior of Jet Currents over a Continental Slope Topography with a Possible Application to the Northern Current. *Journal of Physical Oceanography*, *35*(5), 790–810. https://doi.org/https://doi.org/10.1175/JPO2705.1

Flexas, M. M., Durrieu de Madron, X., Garcia, M. A., Canals, M., & Arnau, P. (2002). Flow variability in the Gulf of Lions during the MATER HFF experiment (March-May 1997). *Journal of Marine Systems*, *33–34*, 197–214. https://doi.org/10.1016/S0924-7963(02)00059-3

Fratianni, C., Nadia, P., Lalli, F., Simoncelli, S., Coppini, G., Pesarino, V., Bruschi, A., Cassese, M. L., & Drudi, M. (2016). Operational oceanography for the Marine Strategy Framework Directive: the case of the mixing indicator. *Journal of Operational Oceanography*, *9*, s223–s233. https://doi.org/10.1080/1755876X.2015.1115634

Fu, L. (1981). Observations and models of inertial waves in the deep ocean. In *Reviews of Geophysics*. https://doi.org/10.1029/RG019i001p00141

Ganachaud, A., & Wunsch, C. (2000). Improved estimates of global ocean circulation, heat transport and mixing from hydrographic data. *Nature*, *408*(6811), 453–457. https://doi.org/10.1038/35044048

Gandin, L. S. (1965). *Objective analysis of meteorological fields. By L. S. Gandin. Israel Program for Scientific Translations, Jerusalem*. 447. https://doi.org/https://doi.org/10.1002/qj.49709239320

Gent, P. R., & Mcwilliams, J. C. (1990). Isopycnal Mixing in Ocean Circulation Models. *Journal of Physical Oceanography*, *20*(1), 150–155. https://doi.org/10.1175/1520-0485(1990)020<0150:IMIOCM>2.0.CO;2

Gill, A. E. (1984). On the Behavior of Internal_waves in the Wakes of Storms. *Journal of Physical Oceanography*, *14*, 1129–1151.

Gonella, J. (1972). A rotary-component method for analysing meteorological and oceanographic vector time series. *Deep Sea Research and Oceanographic Abstracts*, *19*(12), 833–846. https://doi.org/10.1016/0011-7471(72)90002-2

Gould, J., Sloyan, B. M., and Visbeck, M. (2013). *In-situ Ocean Observations: A brief history present status and future directions. In Gerold Siedler, Stephen Griffies, John Gould and John Church (eds) Ocean Circulation and Climate: A 21st Century Perspective, 2nd Ed*. 59–79.

Grilli, F., & Pinardi, N. (1998). The computation of Rossby radii of deformation for the Mediterranean Sea. *MTP News*, *6*(4), 4–5.

Guihou, K., Marmain, J., Ourmières, Y., Molcard, A., Zakardjian, B., & Forget, P. (2013). A case study of the mesoscale dynamics in the North-Western Mediterranean Sea: a combined data–model approach. *Ocean Dynamics*. https://doi.org/10.1007/s10236-013-0619-z

Haidvogel B., D., Curchitser N., E., Danilov, S., & Fox-Kemper, B. (2017). Numerical modelling in a multiscale ocean. In *Journal of Marine Research* (Vol. 75). https://doi.org/10.1357/002224017823523964

Hamlington, P. E., Van Roekel, L. P., Fox-Kemper, B., Julien, K., & Chini, G. P. (2014). Langmuir–Submesoscale Interactions: Descriptive Analysis of Multiscale Frontal Spindown Simulations. *Journal of Physical Oceanography*, *44*(9), 2249–2272. https://doi.org/10.1175/JPO-D-13-0139.1

Hayes, M. H. (1996). *Statistical Digital Signal Processing and Modeling* (1st ed.). John Wiley & Sons, Inc.

Hebert, D., & Moum, J. N. (1994). Decay of a near-inertial wave. In *Journal of Physical Oceanography* (Vol. 24, Issue 11, pp. 2334–2351). https://doi.org/10.1175/1520-0485(1994)024<2334:DOANIW>2.0.CO;2

Herbaut, C., Crépon, M., & Mortier, L. (n.d.). A Sensitivity Study of the General Circulation of the Western Mediterranean Sea. Part I: The Response to Density Forcing

through the Straits. *Journal of Physical Oceanography*, *26*(1), 65–84. https://doi.org/10.1175/1520-0485(1996)026<0065:ASSOTG>2.0.CO;2

Hongbo Qi, De Szoeke, R. A., Paulson, C. A., & Eriksen, C. C. (1995). The structure of near-inertial waves during Ocean Storms. *Journal of Physical Oceanography*, *25*(11 Part II), 2853–2871. https://doi.org/10.1175/1520-0485(1995)025<2853:tsoniw>2.0.co;2

Jochum, M., Briegleb, B. P., Danabasoglu, G., Large, W. G., Norton, N. J., Jayne, S. R., Alford, M. H., & Bryan, F. O. (2013). The impact of oceanic near-inertial waves on climate. *Journal of Climate*, *26*(9), 2833–2844. https://doi.org/10.1175/JCLI-D-12-00181.1

Joyce, T. M., Toole, J. M., Klein, P., & Thomas, L. N. (2013). A near-inertial mode observed within a Gulf Stream warm-core ring. *Journal of Geophysical Research: Oceans*, *118*(4), 1797–1806. https://doi.org/10.1002/jgrc.20141

Kara, A. B., Rochford, P. A., & Hurlburt, H. E. (2000). An optimal definition for ocean mixed layer depth. *Journal of Geophysical Research: Oceans*. https://doi.org/10.1029/2000JC900072

Kawaguchi, Y., Wagawa, T., & Igeta, Y. (2020). Near-inertial internal waves and multiple-inertial oscillations trapped by negative vorticity anomaly in the central Sea of Japan. *Progress in Oceanography*, *181*, 102240. https://doi.org/https://doi.org/10.1016/j.pocean.2019.102240

Kim, S. Y., & Kosro, P. M. (2013). Observations of near-inertial surface currents off Oregon: Decorrelation time and length scales. *Journal of Geophysical Research: Oceans*. https://doi.org/10.1002/jgrc.20235

Klein, P., Lapeyre, G., & Large, W. G. (2004). Wind ringing of the ocean in presence of mesoscale eddies. *Geophysical Research Letters*, *31*(15), 4–7. https://doi.org/10.1029/2004GL020274

Klein, P., Smith, S. L., & Lapeyre, G. (2004). Organization of near-inertial energy by an eddy field. *Quarterly Journal of the Royal Meteorological Society*, *130*(598), 1153–1166. https://doi.org/https://doi.org/10.1256/qj.02.231

Kobashi, F., & Kawamura, H. (2002). Seasonal variation and instability nature of the North Pacific Subtropical Countercurrent and the Hawaiian Lee Countercurrent. *Journal of Geophysical Research: Oceans*, *107*(C11), 3185. https://doi.org/https://doi.org/10.1029/2001JC001225

Kundu, P. K. (1976). An Analysis of Inertial Oscillations Observed Near Oregon Coast. *Journal of Physical Oceanography*, *6*, 879–893.

Kunze, E. (1985). Near-Inertial Wave Propagation In Geostrophic Shear. *Journal of Physical Oceanography*, *15*(5), 544–565. https://doi.org/10.1175/1520-0485(1985)015<0544:NIWPIG>2.0.CO;2

Kunze, E. (1986). The Mean and Near-Inertial Velocity Fields in a Warm-Core Ring. *Journal of Physical Oceanography*, *16*(8), 1444–1461. https://doi.org/10.1175/1520-0485(1986)016<1444:TMANIV>2.0.CO;2

Kunze, E., Schmitt, R. W., & Toole, J. M. (1995). The Energy Balance in a Warm-Core Ring's Near-Inertial Critical Layer. *Journal of Physical Oceanography*, *25*(5), 942–957. https://doi.org/10.1175/1520-0485(1995)025<0942:TEBIAW>2.0.CO;2

Lahoz, W. A., & Schneider, P. (2014). Data assimilation: making sense of Earth Observation. *Frontiers in Environmental Science*, *2*. https://doi.org/10.3389/fenvs.2014.00016

Lapeyre, G. (2017). Surface Quasi-Geostrophy. *Fluids*, *2*(1). https://doi.org/10.3390/fluids2010007

Lascaratos, A., Williams, R., & Tragou, E. (1993). A mixed-layer study of the formation of Levantine Intermediate Water. *Journal of Geophysical Research*, *98*, 14, 714–739, 749. https://doi.org/10.1029/93JC00912

Le Boyer, A., Alford, M. H., Pinkel, R., Hennon, T. D., Yang, Y. J., Ko, D., & Nash, J. (2020). Frequency shift of near-inertial waves in the South China sea. *Journal of Physical Oceanography*, *50*(5), 1121–1135. https://doi.org/10.1175/JPO-D-19-0103.1

Le Traon, P. Y. (2013). From satellite altimetry to Argo and operational oceanography: three revolutions in oceanography. *Ocean Science*, *9*(5), 901–915. https://doi.org/10.5194/os-9-901-2013

Le Traon, P. Y., Reppucci, A., Alvarez Fanjul, E., Aouf, L., Behrens, A., Belmonte, M., Bentamy, A., Bertino, L., Brando, V. E., Kreiner, M. B., Benkiran, M., Carval, T., Ciliberti, S. A., Claustre, H., Clementi, E., Coppini, G., Cossarini, G., De Alfonso Alonso-Muñoyerro, M., Delamarche, A., … Zacharioudaki, A. (2019). From Observation to Information and Users: The Copernicus Marine Service Perspective . In *Frontiers in Marine Science* (Vol. 6). https://www.frontiersin.org/articles/10.3389/fmars.2019.00234

Leaman, K. D., & Sanford, T. B. (1975). Vertical Energy Propagation of Inertial Waves: A Vector Spectral Analysis of Velocity Profiles. *JOURNAL OF GEOPHYSICAL RESEARCH MAY*, *80*(20). https://doi.org/10.1029/JC080i015p01975

Lee, D.-K., & Niiler, P. P. (1998). The inertial chimney: The near-inertial energy drainage from the ocean surface to the deep layer. *Journal of Geophysical Research: Oceans*, *103*(C4), 7579–7591. https://doi.org/https://doi.org/10.1029/97JC03200

Lelong, M. P., Cuypers, Y., & Bouruet-Aubertot, P. (2020). Near-inertial energy propagation inside a mediterranean anticyclonic eddy. *Journal of Physical Oceanography*, *50*(8), 2271–2288. https://doi.org/10.1175/JPO-D-19-0211.1

Lengaigne, M., Menkes, C. E., Aumont, O., Gorgues, T., Bopp, L., André, J.-M., & Madec, G. (2007). Influence of the oceanic biology on the tropical Pacific climate in a coupled general circulation model. *Climate Dynamics*, *28*, 503–516.

Levier, B., Tréguier, A.-M., Madec, G., & Garnier, V. (2007). *Free surface and variable volume in the NEMO code*. *i*, 46. papers3://publication/uuid/7C6C84F3-985D-4BF7-B299-19393359A544

Lilly, J. M., & Olhede, S. C. (2012). Generalized morse wavelets as a superfamily of analytic wavelets. *IEEE Transactions on Signal Processing*, *60*(11), 6036–6041. https://doi.org/10.1109/TSP.2012.2210890

Liu, P. C., & Miller, G. S. (1996). Wavelet Transforms and Ocean Current Data Analysis. *Journal of Atmospheric and Oceanic Technology*, *13*(5), 1090–1099. https://doi.org/10.1175/1520-0426(1996)013<1090:WTAOCD>2.0.CO;2

Lorbacher, K., Dommenget, D., Niiler, P. P., & Köhl, A. (2006). Ocean mixed layer depth: A subsurface proxy of ocean-atmosphere variability. *Journal of Geophysical Research: Oceans*. https://doi.org/10.1029/2003JC002157

Lukas, R., & Lindstrom, E. (1991). The mixed layer of the western Equatorial Pacific Ocean. *Journal of Geophysical Research*, *96*, 3343–3358. https://doi.org/10.1029/90JC01951

Macdonald, A. M., & Wunsch, C. (1996). An estimate of global ocean circulation and heat fluxes. *Nature*, *382*(6590), 436–439. https://doi.org/10.1038/382436a0

MacKinnon, J. A., & Winters, K. B. (2005). Subtropical catastrophe: Significant loss of low-mode tidal energy at 28.9. *Geophysical Research Letters*, *32*(15), 1–5. https://doi.org/10.1029/2005GL023376

Madec, G., Chartier, M., Delécluse, P., & Crépon, M. (1991). A Three-Dimensional Numerical Study of Deep-Water Formation in the Northwestern Mediterranean Sea. *Journal of Physical Oceanography*, *21*(9), 1349–1371. https://doi.org/10.1175/1520-0485(1991)021<1349:ATDNSO>2.0.CO;2

Madec, G., & the NEMO Team. (2019). NEMO ocean engine. *Note Du Pôle de Modélisation*, *27*, 1–386. https://doi.org/10.5281/zenodo.1464816

Mahadevan, A. (2006). Modeling vertical motion at ocean fronts: Are nonhydrostatic effects relevant at submesoscales? In *Ocean Modelling* (Vol. 14). https://doi.org/10.1016/j.ocemod.2006.05.005

Maksimova, E. V. (2018). A conceptual view on inertial internal waves in relation to the subinertial flow on the central west Florida shelf. *Scientific Reports*, *8*(1). https://doi.org/10.1038/s41598-018-34346-2

Manzella, G., Franco, R., Coppini, G., Borghini, M., Crusado, A., Galli, C., Gertman, I., Gervais, T., Hayes, D., Millot, C., Özsoy, E., Tziavos, C., Velasquez, Z., & Zodiatis, G. (2006). The improvements of the Ships Of Opportunity Program in MFSTEP. *Ocean Science Discussions*, *3*. https://doi.org/10.5194/osd-3-1717-2006

Margirier, F., Testor, P., Heslop, E., Mallil, K., Bosse, A., Houpert, L., Mortier, L., Bouin, M. N., Coppola, L., D'Ortenzio, F., Durrieu de Madron, X., Mourre, B., Prieur, L., Raimbault, P., & Taillandier, V. (2020). Abrupt warming and salinification of intermediate waters interplays with decline of deep convection in the Northwestern Mediterranean Sea. *Scientific Reports*, *10*(1). https://doi.org/10.1038/s41598-020-77859-5

Martínez-Marrero, A., Barceló-Llull, B., Pallàs-Sanz, E., Aguiar-González, B., Estrada-Allis, S. N., Gordo, C., Grisolía, D., Rodríguez-Santana, A., & Arístegui, J. (2019). Near-Inertial Wave Trapping Near the Base of an Anticyclonic Mesoscale Eddy Under Normal Atmospheric Conditions. *Journal of Geophysical Research: Oceans*, *124*(11), 8455–8467. https://doi.org/10.1029/2019JC015168

Marullo, S., Salusti, E., & Viola, A. (1985). Observations of a small-scale baroclinic eddy in the Ligurian Sea. *Deep Sea Research Part A, Oceanographic Research Papers*, *32*(2), 215–222. https://doi.org/10.1016/0198-0149(85)90029-9

Melet, A. V, Hallberg, R., & Marshall, D. P. (2022). Chapter 2 - The role of ocean mixing in the climate system. In M. Meredith & A. Naveira Garabato (Eds.), *Ocean Mixing* (pp. 5–34). Elsevier. https://doi.org/https://doi.org/10.1016/B978-0-12-821512-8.00009-8

Millot and Crepon. (1981). Inertial Oscillations on the Continental Shelf of the Gulf of Lions - Observations and Theory. *Journal of Physical Oceanography*, *11*(5), 639–657. https://doi.org/https://doi.org/10.1175/1520-0485(1981)011%3C0639:IOOTCS%3E2.0.CO;2

Millot, C. (1991). Mesoscale and seasonal variabilities of the circulation in the western Mediterranean. *Dynamics of Atmospheres and Oceans*, *15*(3–5), 179–214. https://doi.org/10.1016/0377-0265(91)90020-G

Millot, C. (1999). Circulation in the Western Mediterranean Sea. *Journal of Marine Systems*, *20*(1–4), 423–442. https://doi.org/10.1016/S0924-7963(98)00078-5

Millot, C., & Taupier-Letage, I. (2005). Circulation in the Mediterranean Sea. In A. Saliot (Ed.), *The Mediterranean Sea* (pp. 29–66). Springer Berlin Heidelberg. https://doi.org/10.1007/b107143

Millot, C. (2013). Levantine Intermediate Water characteristics: an astounding general misunderstanding! ; Las características de LIW: un malentendido asombroso. *Scientia Marina Barcelona (Spain) SCI. MAR*, *77*(772), 217–232. https://doi.org/10.3989/scimar.03518.13A

Mooers, C. N. K. (1973). A technique for the cross spectrum analysis of pairs of complex-valued time series, with emphasis on properties of polarized components and rotational invariants. *Deep Sea Research and Oceanographic Abstracts*, *20*(12), 1129–1141. https://doi.org/10.1016/0011-7471(73)90027-2

Moum, J. N., Farmer, D. M., Smyth, W. D., Armi, L., & Vagle, S. (2003). Structure and Generation of Turbulence at Interfaces Strained by Internal Solitary Waves Propagating Shoreward over the Continental Shelf. *Journal of Physical Oceanography*, *33*(10), 2093. https://doi.org/10.1175/1520-0485(2003)033<2093:SAGOTA>2.0.CO;2

Nagai, T., & Hibiya, T. (2015). Internal tides and associated vertical mixing in the Indonesian Archipelago. *Journal of Geophysical Research: Oceans*, *120*, 3373–3390. https://doi.org/https://doi.org/10.1002/2014JC010592

Nash, J. D., & Moum, J. N. (2005). River plumes as a source of large-amplitude internal waves in the coastal ocean. *Nature*, *437*(7057), 400–403. https://doi.org/10.1038/nature03936

Nezlin, N. P. (2004). Remotely sensed seasonal dynamics of phytoplankton in the Ligurian Sea in 1997–1999. *Journal of Geophysical Research*. https://doi.org/10.1029/2000JC000628

Nikurashin, M., & Ferrari, R. (2010). Radiation and dissipation of internal waves generated by geostrophic motions impinging on small-scale topography: Theory. *Journal of Physical Oceanography*, *40*(5), 1055–1074. https://doi.org/10.1175/2009JPO4199.1

Oddo, P., Bonaduce, A., Pinardi, N., & Guarnieri, A. (2014). Sensitivity of the Mediterranean Sea level to atmospheric pressure and free surface elevation numerical formulation in NEMO. *Geoscientific Model Development*. https://doi.org/10.5194/gmd-7-3001-2014

Oddo, P., Falchetti, S., Viola, S., Pennucci, G., Storto, A., & Borrione, I. (2022). Evaluation of different Maritime rapid environmental assessment procedures with a focus on acoustic performance. *Journal of the Acoustical Society of America*, *152*(5), 2962–2981. https://doi.org/10.1121/10.0014805

Oddo, P., & Pinardi, N. (2008). Lateral open boundary conditions for nested limited area models: A scale selective approach. *Ocean Modelling*, *20*(2), 134–156. https://doi.org/10.1016/j.ocemod.2007.08.001

Oey, L.-Y., Inoue, M., Lai, R., Lin, X.-H., Welsh, S. E., & Rouse Jr., L. J. (2008). Stalling of near-inertial waves in a cyclone. *Geophysical Research Letters*, *35*(12). https://doi.org/https://doi.org/10.1029/2008GL034273

Olhede, S. C., & Walden, A. T. (2002). Generalized Morse wavelets. *IEEE Transactions on Signal Processing*, *50*(11), 2661–2670. https://doi.org/10.1109/TSP.2002.804066

Ostrovsky, L. ~A., & Stepanyants, Y. A. (1989). Do internal solitions exist in the ocean? *Reviews of Geophysics*, *27*(3), 293–310. https://doi.org/10.1029/RG027i003p00293

Padman, L., & Erofeeva, S. (2004). A barotropic inverse tidal model for the Arctic Ocean. *Geophysical Research Letters*, *31*(2). https://doi.org/https://doi.org/10.1029/2003GL019003

Pedlosky, J. (1987). *Geophysical fluid dynamics* (Vol. 710). Springer.

Perkins, H. (1972). *Inertial oscillations in the Mediterranean** (Vol. 19). Pergamon Press.

Perkins, H. (1976). Observed effect of an eddy on inertial oscillations. *Deep Sea Research and Oceanographic Abstracts*, *23*(11), 1037–1042. https://doi.org/10.1016/0011-7471(76)90879-2

Picco, P., Cappelletti, A., Sparnocchia, S., Schiano, M. E., Pensieri, S., & Bozzano, R. (2010). Upper layer current variability in the Central Ligurian Sea. *Ocean Science*. https://doi.org/10.5194/os-6-825-2010

Pinardi, N., & Navarra, A. (1993). Baroclinic wind adjustment processes in the Mediterranean Sea. *Deep-Sea Research Part II*, *40*(6), 1299–1326. https://doi.org/10.1016/0967-0645(93)90071-T

Pinardi, N., Zavatarelli, M., Adani, M., Coppini, G., Fratianni, C., Oddo, P., Simoncelli, S., Tonani, M., Lyubartsev, V., Dobricic, S., & Bonaduce, A. (2015). Mediterranean Sea large-scale low-frequency ocean variability and water mass formation rates from 1987 to 2007: A retrospective analysis. *Progress in Oceanography*, *132*, 318–332. https://doi.org/10.1016/j.pocean.2013.11.003

Pinardi, N., Zavatarelli, M., Arneri, E., Crise, A., & Ravaioli, M. (2006). *The physical, sedimentary and ecological structure and variability of shelf areas in the Mediterranean Sea.*

Poulain, P. M., Gerin, R., Rixen, M., Zanasca, P., Teixeira, J., Griffa, A., Molcard, A., de Marte, M., & Pinardi, N. (2012). Aspects of the surface circulation in the Liguro-Provençal basin and Gulf of Lion as observed by satellite-tracked drifters (2007-2009). *Bollettino Di Geofisica Teorica Ed Applicata*, *53*(2), 261–279. https://doi.org/10.4430/bgta0052

Poulain, P.-M., Luther, D. S., & Patzert, W. C. (1992). Deriving Inertial Wave Characteristics From Surface Drifter Velocities' Frequency Variability in the Tropical Pacific. In *JOURNAL OF GEOPHYSICAL RESEARCH* (Vol. 97). https://doi.org/10.1029/92JC01381

Poulain, P.-M., Menna, M., & Mauri, E. (2012). Surface Geostrophic Circulation of the Mediterranean Sea Derived from Drifter and Satellite Altimeter Data. *Journal of Physical Oceanography*, *42*(6), 973–990. https://doi.org/10.1175/JPO-D-11-0159.1

Poulain, P.-M., R, B., J, F., Cruzado, A., C, M., Gertman, I., Griffa, A., Molcard, A., V, R., Bras, S., & Villeon, L. (2006). MEDARGO: A drifting profiler program in the Mediterranean Sea. *Ocean Science Discussions (OSD)*, *3*. https://doi.org/10.5194/osd-3-1901-2006

Pujol, I., Yannice, F., Taburet, G., Dupuy, S., Pelloquin, C., Michaël, A., & Picot, N. (2016). DUACS DT2014 : the new multi-mission altimeter dataset reprocessed over 20 years. *Ocean Science Discussions*, 1–48. https://doi.org/10.5194/os-2015-110

Qu, T., Du, Y., Gan, J., & Wang, D. (2007). Mean seasonal cycle of isothermal depth in the South China Sea. *Journal of Geophysical Research*, *112*. https://doi.org/10.1029/2006JC003583

Rainville, L., & Pinkel, R. (2004). Observations of energetic high-wavenumber internal waves in the Kuroshio. *Journal of Physical Oceanography*, *34*(7), 1495–1505. https://doi.org/10.1175/1520-0485(2004)034<1495:OOEHIW>2.0.CO;2

Raja, K. J., Buijsman, M. C., Shriver, J. F., Arbic, B. K., & Siyanbola, O. (2022). Near-Inertial Wave Energetics Modulated by Background Flows in a Global Model Simulation. *Journal of Physical Oceanography*, *52*(5), 823–840. https://doi.org/10.1175/JPO-D-21-0130.1

Ray, R. D., & Mitchum, G. T. (1996). Surface manifestation of internal tides generated near Hawaii. *Geophysical Research Letters*, *23*, 2101–2104.

Rhines, P. B. (1979). Geostrophic Turbulence. *Annual Review of Fluid Mechanics*, *11*(1), 401–441. https://doi.org/10.1146/annurev.fl.11.010179.002153

Robinson, A. R., Hecht, A., Pinardi, N., Bishop, J., Leslie, W. G., Rosentroub, Z., Brenner, S. (1987). Small synoptic/mesoscale eddies and energetic variability of the eastern Levantine basin. *Nature*, *327*(6118), 131–134. https://doi.org/https://doi.org/10.1038/327131A0

Robinson, A. R., Malanotte-Rizzoli, P., Hecht, A., Michelato, A., Roether, W., Theocharis, A., Ünlüata, Ü., Pinardi, N., Artegiani, A., Bergamasco, A., Bishop, J., Brenner, S., Christianidis, S., Gacic, M., Georgopoulos, D., Golnaraghi, M., Hausmann, M., Junghaus, H.-G., Lascaratos, A., … Osman, M. (1992). General circulation of the Eastern Mediterranean. *Earth-Science Reviews*, *32*(4), 285–309. https://doi.org/https://doi.org/10.1016/0012-8252(92)90002-B

Robinson, A. R., & Golnaraghi, M. (1993). Circulation and dynamics of the Eastern Mediterranean Sea; quasi-synoptic data-driven simulations. *Deep Sea Research Part II: Topical Studies in Oceanography*, *40*(6), 1207–1246. https://doi.org/https://doi.org/10.1016/0967-0645(93)90068-X

Robinson, A. R., Leslie, W. G., Theocharis, A., & Lascaratos, A. (2001). *Mediterranean Sea Circulation*.

Ruiz, S., Renault, L., Garau, B., & Tintoré, J. (2012). Underwater glider observations and modeling of an abrupt mixing event in the upper ocean. *Geophysical Research Letters*. https://doi.org/10.1029/2011GL050078

Salmon. (1998). *Lectures on Geophysical Fluid Dynamics*. New York: Oxford Univ. Press., 278 pp.

Sammari, C., Millot, C., & Prieur, L. (1995). Aspects of the seasonal and mesoscale variabilities of the Northern Current in the western Mediterranean Sea inferred from the PROLIG-2 and PROS-6 experiments. *Deep-Sea Research Part I*, *42*(6), 893–917. https://doi.org/10.1016/0967-0637(95)00031-Z

Sanford, T. B. (1975). *Observations of the Vertical Structure of Internal Waves*. *80*(27), 3861–3871. https://doi.org/https://doi.org/10.1029/JC080I027P03861

Schröder, K., Gasparini, G. P., Tangherlini, M., & Astraldi, M. (2006). Deep and intermediate water in the western Mediterranean under the influence of the Eastern Mediterranean Transient. *Geophysical Research Letters*, *33*(21). https://doi.org/https://doi.org/10.1029/2006GL027121

Schroeder, K., Haza, A. C., Griffa, A., Özgökmen, T. M., Poulain, P. M., Gerin, R., Peggion, G., & Rixen, M. (2011). Relative dispersion in the Liguro-Provençal basin: From sub-mesoscale to mesoscale. *Deep-Sea Research Part I: Oceanographic Research Papers*. https://doi.org/10.1016/j.dsr.2010.11.004

Schroeder, K., Gasparini, G., Tangherlini, M., & Astraldi, M. (2006). Deep and intermediate water in the western Mediterranean under the influence of the Eastern Mediterranean Transient. *GEOPHYSICAL RESEARCH LETTERS*, *33*. https://doi.org/10.1029/2006GL027121

Scott, R. B., & Wang, F. (2005). Direct evidence of an oceanic inverse kinetic energy cascade from satellite altimetry. *Journal of Physical Oceanography*, *35*, 1650–1666. https://doi.org/10.1175/JPO2771.1

Shchepetkin, A. F., & McWilliams, J. C. (2005). The regional oceanic modeling system (ROMS): a split-explicit, free-surface, topography-following-coordinate oceanic model. *Ocean Modelling*, *9*(4), 347–404. https://doi.org/https://doi.org/10.1016/j.ocemod.2004.08.002

Silverthorne, K. E., & Toole, J. M. (2009). Seasonal kinetic energy variability of near-inertial motions. *Journal of Physical Oceanography*, *39*(4), 1035–1049. https://doi.org/10.1175/2008JPO3920.1

Simmons, H. L., & Alford, M. H. (2012). Simulating the long-range swell of internal waves generated by ocean storms. *Oceanography*, *25*(2), 30–41. https://doi.org/10.5670/oceanog.2012.39

Small, R. J., Carniel, S., Campbell, T., Teixeira, J., & Allard, R. (2012). The response of the Ligurian and Tyrrhenian Seas to a summer Mistral event: A coupled atmosphere-ocean approach. *Ocean Modelling*, *48*, 30–44. https://doi.org/10.1016/j.ocemod.2012.02.003

Stoica, P. (2005). Spectral analysis of signals / Petre Stoica and Randolph Moses. In *Spectral analysis of signals*. Pearson/Prentice Hall.

Storto, A., Oddo, P., Cozzani, E., & Coelho, E. F. (2019). Introducing along-track error correlations for altimetry data in a regional ocean prediction system. *Journal of Atmospheric and Oceanic Technology*, *36*(8), 1657–1674. https://doi.org/10.1175/JTECH-D-18-0213.1

Taupier-Letage, I., & Millot, C. (1986). General hydrodynamical features in the Ligurian Sea inferred from the DYOME experiment. *Oceanologia Acta*, *9*(2), 119–131.

Thomas, L. N. (2017). On the modifications of near-inertial waves at fronts: implications for energy transfer across scales. *Ocean Dynamics*, *67*(10), 1335–1350. https://doi.org/10.1007/s10236-017-1088-6

Thomson, R. E., & Emery, W. J. (n.d.). *DATA ANALYSIS METHODS IN PHYSICAL OCEANOGRAPHY THIRD EDITION*.

Tintoré, J., Gomis, D., Alonso, S., & Wang, D.-P. (1988). A theoretical study of large sea level oscillations in the western Mediterranean. *Journal of Geophysical Research*, *93*(C9), 10797. https://doi.org/10.1029/jc093ic09p10797

Tobias, S., Friedrich, T., Hartman, S., Oschlies, A., Wallace, D. W. R., & Arne, K. (2010). Estimating mixed layer nitrate in the North Atlantic Ocean. *Biogeosciences*, *6*. https://doi.org/10.5194/bgd-6-8851-2009

Treguier, A., Sommer, J. L. E., Beckmann, A., Biastoch, A., Remy, E., Theetten, S., Bernard, B., Madec, G., & Penduff, T. (2006). Impact of partial steps and momentum advection schemes in a global ocean circulation model at eddy-permitting resolution. *Ocean Dynamics*, *56*(December), 543–567. http://www.springerlink.com/index/W8327463321564N3.pdf

Tsimplis, M. N., Proctor, R., & Flather, R. A. (1995). A two-dimensional tidal model for the Mediterranean Sea. *Journal of Geophysical Research: Oceans*, *100*(C8), 16223–16239. https://doi.org/10.1029/95JC01671

Tsimplis, M. N., Zervakis, V., Josey, S. A., Peneva, E. L., Struglia, M. V., Stanev, E. V, Theocharis, A., Lionello, P., Malanotte-Rizzoli, P., Artale, V., Tragou, E., & Oguz, T. (2006). Changes in the Oceanography of the Mediterranean Sea and their Link to Climate Variability. *Developments in Earth and Environmental Sciences*, *4*, 227–282. https://doi.org/10.1016/S1571-9197(06)80007-8

Umlauf, L., & Burchard, H. (2003). A generic length-scale equation for geophysical turbulence models. *Journal of Marine Research*, *61*, 235–265.

Umlauf, L., & Burchard, H. (2005). Second-order turbulence closure models for geophysical boundary layers. A review of recent work. *Continental Shelf Research*, *25*(7), 795–827. https://doi.org/https://doi.org/10.1016/j.csr.2004.08.004

Van Aken, H. M., van Haren, H., & Maas, L. R. M. (2007). The high-resolution vertical structure of internal tides and near-inertial waves measured with an ADCP over the continental slope in the Bay of Biscay. *Deep-Sea Research Part I: Oceanographic Research Papers*. https://doi.org/10.1016/j.dsr.2007.01.003

Van Haren, H., & Millot, C. (2003). Seasonality of internal gravity waves kinetic energy spectra in the Ligurian Basin. *Oceanologica Acta*, *26*(5), 635–644. https://doi.org/https://doi.org/10.1016/S0399-1784(03)00062-8

Wagner, G. L., & Young, W. R. (2016). A three-component model for the coupled evolution of near-inertial waves, quasi-geostrophic flow and the near-inertial second harmonic. *Journal of Fluid Mechanics*, *802*, 806–837. https://doi.org/DOI: 10.1017/jfm.2016.487

Weatherall, P., Marks, K. M., Jakobsson, M., Schmitt, T., Tani, S., Arndt, J. E., Rovere, M., Chayes, D., Ferrini, V., & Wigley, R. (2015). A new digital bathymetric model of the world's oceans. *Earth and Space Science*, *2*(8), 331–345. https://doi.org/https://doi.org/10.1002/2015EA000107

Welch, P. D. (1967). The use of fast Fourier transform for the estimation of power spectra: A method based on time averaging over short, modified periodograms. *IEEE Transactions on Audio and Electroacoustics*, *15*, 70–73.

Weller, R. A. (1985). Near-Surface Velocity Variability at Inertial and Subinertial Frequencies in the Vicinity of the California Current. *Journal of Physical Oceanography*, *15*(4), 372–385. https://doi.org/10.1175/1520-0485(1985)015<0372:NSVVAI>2.0.CO;2

Whitt, D. B., & Thomas, L. N. (2013). Near-inertial waves in strongly baroclinic currents. *Journal of Physical Oceanography*, *43*(4), 706–725. https://doi.org/10.1175/JPO-D-12-0132.1

Wortham, C., & Wunsch, C. (2014). A Multidimensional Spectral Description of Ocean Variability. *Journal of Physical Oceanography*, *44*(3), 944–966. https://doi.org/10.1175/JPO-D-13-0113.1

Young, W. R., & Jelloul, M. Ben. (1997). Propagation of near-inertial oscillations through a geostrophic flow. *Journal of Marine Research*. https://doi.org/10.1357/0022240973224283

Zalesak, S. T. (1979). Fully multidimensional flux-corrected transport algorithms for fluids. *Journal of Computational Physics*, *31*(3), 335–362. https://doi.org/https://doi.org/10.1016/0021-9991(79)90051-2

Zhai, X., Greatbatch, R. J., & Zhao, J. (2005). Enhanced vertical propagation of storm-induced near-inertial energy in an eddying ocean channel model. *Geophysical Research Letters*, *32*(18). https://doi.org/https://doi.org/10.1029/2005GL023643

Zhao, Z., & Alford, M. H. (2009). New altimetric estimates of mode-1 M2 internal tides in the Central North Pacific Ocean. *Journal of Physical Oceanography*, *39*(7), 1669–1684. https://doi.org/10.1175/2009JPO3922.1